NTNU – Trondheim
Norwegian University of
Science and Technology

Non-linear Wave Loads on Offshore Wind Support Structure

Jinchao Chen

Wind Energy
Submission date: June 2014
Supervisor: Carl Martin Larsen, IMT
Co-supervisor: Andrei Metrikine, TU Delft

Norwegian University of Science and Technology
Department of Marine Technology

Master Thesis of Science

Nonlinear Wave Loads on Offshore Wind Support Structure

Jinchao Chen

June 27, 2014

European Wind Energy Master - EWEM- Offshore Track

Nonlinear Wave Loads on Offshore Wind Support Structure

MASTER OF SCIENCE THESIS

For obtaining the degree of Master of Science in Offshore Engineering at Delft University of Technology and in Technology-Wind Energy at Norwegian University of Science and Technology.

Jinchao Chen

June 27, 2014

European Wind Energy Master - EWEM
Delft University of Technology
Norwegian University of Science and Technology

NTNU

TU Delft
Delft
University of
Technology

Copyright © Jinchao Chen
All rights reserved.
Cover photo: http://www.statoil.com

European Wind Energy Master - EWEM
Of
Offshore Track

The undersigned hereby certify that they have read and recommend to the European Wind Energy Master - EWEM for acceptance a thesis entitled **“Nonlinear Wave Loads on Offshore Wind Support Structure”** by **Jinchao Chen** in partial fulfillment of the requirements for the degree of **Master of Science**.

Dated: June 27, 2014

Supervisor: ______________________
Prof. C.M. Larsen of Norwegian University of Science and Technology

Supervisor: ______________________
Prof. Dr. A.V. Metrikine of Delft University of Technology

Abstract

Offshore wind development is constrained by its high cost. One potential way to meet this challenge is to reduce the uncertainty in wave modeling and hydrodynamic loads calculation for offshore wind support structures design. The thesis covers two aspects for calculating loads acting on a offshore wind support structure: an improved hydrodynamic load model and a modified higher order wave model.

In studying hydrodynamic load model, FNV and Rainey's methods, both intended to explain third order phenomena observed on offshore slender structure, are compared and analyzed to solve the surface piercing problem, critical for a slender structure at an extreme sea state. Rainey's new equation is preferred over FNV.

Second order irregular wave model, a simple higher order stochastic wave model, enables it to include non-linear contributions from waves. Analysis focuses on how the modified wave model affects wave surface elevation, wave power spectrum and wave kinematics.

With improved hydrodynamic load model and wave model introduced, there are in total six methods available to calculate the loads acting on a slender offshore wind support structure. The proposed six methods are invstigated by comparing load statistics and corresponding power spectrum of shear force and bending moment at foundation base. The implementation of non-linear models increases foundation shear and bending moment by 3% to 34%

For a floating type support structure, the analysis concentrates on dynamic response of structure, including spar hull and mooring lines. With the assistance of numerical tool RIFLEX, the non-linear dynamic problem is solved in time domain by displaying displacements and forces at targeted section, mooring lines and cylinder hull. It is observed that the low frequency components exerts a reduction effect on maximum axial force on mooring lines, while higher order frequency effects are absent. Based a simple long term extrapolation, environmental contour line method, the reduction effect is predicted to be 10% at the mooring line for a 50-year sea state. When it comes to fatigue analysis, second order irregular wave model only slightly differs damage level at cylinder hull around surface piercing point, but greatly reduce cycle nubmers on mooring lines.

Acknowledgements

I would like to express my sincere gratefulness to my supervisors, Professor Larsen and Professor Metrikine for providing me with encouragements, inspirations and supports during my thesis work.

I also want to thank EWEM offshore track fellows for all the moments we shared and EWEM coordinating team for all the efforts they contributed to organzing the master program.

Last but not least, I would like to thank my parents for being so supportive.

Jinchao Chen
Trondheim, Norway

Contents

Acknowledgements **vii**

List of Figures **xiv**

List of Tables **xvi**

Nomenclature **xvii**

1 Introduction **1**
- 1.1 Background 1
- 1.2 Hywind Demo Project 2
- 1.3 Wave Forces 4
- 1.4 Nonlinear Phenomena 6
- 1.5 Objectives 7

2 Hydrodynamic Model **9**
- 2.1 State of the art 9
  - 2.1.1 Morison equation 9
  - 2.1.2 Stretching 10
- 2.2 Wave Model 11
  - 2.2.1 Higher order Stokes 11
  - 2.2.2 Stream function 13
  - 2.2.3 Second order irregular wave 13
  - 2.2.4 Fully nonlinear model 14
  - 2.2.5 Kinematics 14
- 2.3 Sea loads models 15
  - 2.3.1 The FNV-theory 15
  - 2.3.2 Rainey's new equation 17

2.3.3 Alternatives . . . 19
2.3.4 Comparison . . . 19
2.4 Preliminary calculations . . . 20
2.4.1 FNV-theory . . . 20
2.4.2 Rainey's new equation . . . 23

3 Second Order Irregular Waves 27
3.1 Stochasticity . . . 27
3.2 Wave model . . . 29
3.3 Wave generation . . . 30
3.3.1 Regular wave . . . 32
3.3.2 Bichromatic wave . . . 35
3.3.3 Irregular wave . . . 35
3.4 Wave kinematics . . . 39
3.5 Force . . . 43
3.5.1 Implementation in Rainey's model . . . 43
3.5.2 Comparison . . . 45
3.6 Conclusion . . . 53

4 Dynamics of Floating Wind Turbine 55
4.1 RIFLEX model . . . 55
4.2 Environmental Input . . . 57
4.2.1 Wave . . . 57
4.2.2 Current . . . 57
4.2.3 Wind . . . 58
4.2.4 Second order irregular wave . . . 58
4.3 Time domain simulation . . . 60
4.3.1 Convergence study . . . 60
4.3.2 Dynamic analysis . . . 62
4.4 Extreme load . . . 67
4.4.1 Full long term all sea state approach . . . 68
4.4.2 Contour line method . . . 71
4.5 Fatigue damage . . . 74
4.6 Conclusion . . . 78

5 Conclusions and further work 81
5.1 Conclusions . . . 81
5.2 Further work . . . 82

A Hywind Model 87

B Matlab Scripts 91
B.1 Non-linear Load calculation . . . 91
B.2 Rossenblatt Transformation . . . 102

C Modal Analysis **105**
- C.1 Modal analysis . . . 105
  - C.1.1 Beam model . . . 105
  - C.1.2 Modal superposition . . . 107
- C.2 Hywind Model . . . 109

D Mooring line dynamics **113**

E Wave Force **121**

List of Figures

1.1 Classification of wave forces 5
1.2 Springing phenomenon 6

2.1 Wheeler stretching 11
2.2 Guidance for stream function order 12
2.3 Total point loads 21
2.4 Elastic response along the center line, $KA = 0.1$ 22
2.5 Elastic response of cylinder hull 22
2.6 RAO at different wave amplitude 23
2.7 Point force,Rainey's Method, $KA = 0.1$ 24
2.8 Third order contributions, comparison between Rainey and FNV's method, $KA = 0.1$ 24

3.1 Realization of Jonswasp spectrum 28
3.2 Second order wave frequency matrix, left sum-freq, right dif-freq 32
3.3 Second order regular wave 33
3.4 Second Order Regular Wave, 4 sea states comparison 34
3.5 Time series of bichromatic wave, red: second order, blue: first order . . . 36
3.6 Second order irregular wave time series 37
3.7 Wave elevation spectrum, $H_s = 5\ m,\ T_p = 12\ s,\ ,\gamma = 3.3,\ h = 20\ m$ . . . 38
3.8 Wave Kinematics, regular wave, t=0s, h=30 m 41
3.9 Wave Kinematics, bichromatic, t=0s, h=30 m 42
3.10 Horizontal particle velocity, bichromatic waves, $h = 30\ m,\ T_1 = 8\ s,\ T_2 = 12\ s, A_1 = 2\ m, A_2 = 2\ m$ 42
3.11 Comparison of Rainey's model with linear wave model with stretching . . 46
3.12 Drag component 47
3.13 Comparison of foundation base shear, bending moment calculated with various loads model, ratio to first order value 49

3.14 Load comparison 1, blue: Linear Morison, red: Linear Rainey 50
3.15 Load comparison 2, blue: Linear Morison, red: Non-linear Morison 50
3.16 Load comparison 3, blue: Linear Rainey, red: Non-linear Rainey 51
3.17 Frequency guided support structure design method 52
3.18 Extreme value distribution for local and global maxima 52
3.19 Probability plot for local peaks 53

4.1 Mooring system layout 56
4.2 Mooring line configuration [1] 57
4.3 Current profile 58
4.4 Spectrum for wave surface elevation 59
4.5 Wave surface elevation spectrum, $T_1 = 8\ s,\ T_2 = 12\ s, A_1 = 2\ m, A_2 = 2\ m,\ h = 200\ m$ 59
4.6 Horizontal particle velocity, bichromatic waves, $h = 200\ m,\ T_1 = 8\ s,\ T_2 = 12\ s, A_1 = 2\ m, A_2 = 2\ m$ 60
4.7 Convergence study, response over various time step 61
4.8 Dynamic response of cylinder hull in wave zone, $H_s = 6\ m, T_p = 6\ s$ . . . 63
4.9 Dynamics of cylinder hull at mooring point, $H_s = 6\ m, T_p = 6\ s$ 64
4.10 Heave and pitch motion of cylinder hull, $H_s = 6\ m, T_p = 6\ s$ 66
4.11 Dynamics of delta line, line 3,$H_s = 6\ m, T_p = 6\ s$ 66
4.12 Dynamic response of main mooring line, line 9, $H_s = 6\ m, T_p = 6\ s$ 68
4.13 Envrionmental contour lines 72
4.14 Design ponits on the contour line, left first order wave, right, second order 73
4.15 Gumbel Fit 74
4.16 Dynamic response on main mooring line 9, $H_s = 6\ m, T_p = 12\ s$ 76
4.17 Rainflow counting matrix, $H_s = 6\ m,\ T_p = 12\ s,\ t = 6000\ s$ 77
4.18 Rainflow counting cycle number comparison, amplitude range versus cycle number, $H_s = 6\ m$, $T_p = 12\ s$, $t = 6000\ s$ 79

A.1 Structural drawing of Hywind Demo [1] 88

C.1 Modes shape for the lowest six modes 107

D.1 Maixmum value of dynamic response on main mooring line 9, $H_s = 6\ m, T_p = 12\ s$ 114
D.2 Maixmum value of dynamic response on main mooring line 9, $H_s = 6\ m, T_p = 12\ s$ 115
D.3 Maixmum value of dynamic response on main mooring line 9, $H_s = 6\ m, T_p = 12\ s$ 116
D.4 Maixmum value of dynamic response on main mooring line 9, $H_s = 6\ m, T_p = 12\ s$ 117
D.5 Maixmum value of dynamic response on main mooring line 9, $H_s = 6\ m, T_p = 12\ s$ 118
D.6 Maixmum value of dynamic response on main mooring line 9, $H_s = 6\ m, T_p = 12\ s$ 119

List of Tables

1.1 Technical data of Hywind Demo[2] 2
1.2 Structural parameters for each segment of Hywind 3
1.3 Hywind support structure mass distribution 3
1.4 Siemens 2.3 MW turbine mass distribution 4
1.5 Natural frequencies of Hywind Demo [2] 4

3.1 Summary of data sets used in simulation 33
3.2 Summary of regular wave statistics, water depth 30m 35
3.3 Biachromatic wave parameters 35
3.4 Code Validation, $H_s = 12\ m, T_p = 14\ s, h = 30\ m$ 38
3.5 Statistics for sea surface elevation 39
3.6 Load calculation models 45
3.7 Comparison of load statistics of monopile base shear, quasi-static assumed, regular wave, T=8 s, H=3 m 45
3.8 Sea states 48
3.9 Comparison of load statistics of monopile base shear, quasi-static assumed, averages maximum over 50 simulations, ratio to first order value 48
3.10 Comparison of load statistics of monopile base bending moment, quasi-static assumed, average maximum over 50 simulations, ratio to first order value 49

4.1 Hywind wind model brief 57
4.2 Current profile 57
4.3 CPU time for non-linear time integration 62
4.4 Statistics comparison, different time steps 62
4.5 Dynamic response statistics, $H_s = 6\ m, T_p = 6\ s$ 69
4.6 Design points, linear wave model 72
4.7 Design points, non-linear wave model 72

4.8 Dynamic response statistics, long term exptrapolation 74
4.9 Dynamic response statistics, force variance, $H_s = 6\ m$, $T_p = 12\ s$ 75

A.1 Mooring line structural properties 87
A.2 Structural properties of cylinder hull and turbine tower 89

C.1 Roots of the characteristic equation for a free-free beam 107
C.2 Eigenfrequencies for the lowest six modes 111

E.1 Comparison of load statistics of monopile base shear, quasi-static assumed, averages over 50 simulations, absolute value 121
E.2 Comparison of load statistics of monopile base bending moment, quasi-static assumed, average over 50 simulations, absolute value 121

Nomenclature

Latin Symbols

$A_m,\ A_n$	wave amplitude for wave component m, n	m
S	wave parameter steepness	$-$
$u^{(1)}$	horizontal particle velocity, first order	m/s
$u^{(2+)}$	horizontal particle velocity, second order sum frequency component	m/s
$u^{(2-)}$	horizontal particle velocity, second order difference frequency component	m/s
$u^{(2)}$	horizontal particle velocity, second order	m/s
$X(n)$	stream function coefficient	$-$
Δf	sampling frequency	rad/s
Φ	velocity potential	-
A^{2D}	High-frequency limit of the added mass	
$B^{\pm}_{mn}$	quadratic surface elevation transfer functions	$-$
c	wave celerity	m/s
C_A	mass coefficient	-
C_D	drag coefficient	-
cf	cut off frequency	Hz
D	cylinder diameter	m
H	wave height	m
H_s	significant wave height	m
K,k	wave number	rad
KA	wave steepness	-
L	characteristic length	m

T_p	peak period	s
u	particle velocity in x-direction	m/s
w	particle velocity in z-direction	m/s
L	cylinder length	m
c	wave celerity	m/s

Greek Symbols

α	intersection angle	rad
μ	shallow water parameter	–
A^{2D}	high-frequency limit of the added mass, 2D	–
$\ddot{\eta}_i$	Rigid body acceleration in i direction	m^2/s
$\dot{\eta}_i$	Rigid body velocity in i direction	m/s
ϵ	perturbation parameter	-
η_i	Rigid body displacement in i direction	m
λ	wave length	m
μ	shallow water parameter	-
ω	wave frequency	rad/s
ϕ	phase angle	rad
Φ_i	potential to the $i^{th} order$	-
ζ	free surface elevation	m
h	water depth	m

Subscripts

n,m	wave component n,m

Superscripts

2+	2nd order sum frequency correction term
2−	2nd order difference frequency correction term

Abbreviations

DOF	degree of freedom
FLS	fatigue limit state

IFFT	inverse fast Fourier transform
MSL	Mean sea level
MSL	mean sea level
ULS	ultimate limit state
WTG	Wind turbine generator

Chapter 1

Introduction

1.1 Background

The wind industry is nowadays experiencing a technology transfer from onshore to offshore, which makes offshore wind one of the fastest growing maritime sectors. Statistics reveals that installed offshore wind capacity has reached 5 GW by the end of 2012, and the figure is expected to reach 40 GW, meeting 4% of European electricity demand in the near future [3].

Offshore wind turbines, mainly installed in North Sea, are mounted on bottom fixed substructures. Among them, monopiles and gravity based substructures are the most commonly employed offshore wind foundations for regions with a water depth of smaller than 30 m, while frame structures, i.e. jackets and tripods, are chosen for a deeper site up to 50 m, e.g. OWEC tower at Beatrice Windfarm [4]. But for an even deeper site larger than 100 m, the diameter of support structure needs to increase significantly to ensure the integrity of the utility, which causes problems for both design and installation. To harness offshore wind resources in countries with a steep continental shelf, such as China, USA, Japan and Norway, floating type support structures are generally preferred over fixed ones. Several alternatives are available for floating wind turbine design, including spar, semi-submersible, TLP etc.

Though booming, offshore wind development is greatly constrained by its high cost. Compared with land-based wind turbines, which are already less economically competitive than fossil fuels, offshore wind development easily exerts extra demand on investment. Different from land based structures, offshore wind turbines are subjected to hydrodynamic forces in addition to aerodynamic loads. A potential way to reduce the cost is to gain a more in depth insight into incident wave modeling and the mechanism that explains how wave interacts with structure.

To predict hydrodynamic loads on such a slender structure, Morison equation combined with first order wave theory, is widely used in industry to divide wave loads into two components, inertia and drag forces[5], leaving out higher order terms. The calculation based on Morison equation generates satisfying results and is computationally efficient for a benign sea state. But when set at a harsh sea state, where wave height is comparable to the structure diameter, nonlinear effects might be excited and affect the steady state oscillations by displaying higher order steady state or transient response. Besides, first order wave theory, which uses linearized boundary condition, fails to describe wave kinematics in the wave zone and subsequently leaves out loads in the wave zone.

Solving the above mentioned problem requires a modified load model and a more sophisticated wave model. For a bottom fixed substructure, which is frequency driven in design, the higher order terms introduced with either method can better determine the frequency range that the support structure should be sited. For a floating wind turbine, which is in most cases moored, the low frequency items included by using a non-linear wave model might affect mooring line design for both ULS and FLS. Most importantly, with an improved environmental description implemented, the safety margin included in engineering design can be accordingly reduced and consequently cut down offshore wind cost.

The primary objective of this thesis is to introduce a more sophisticated hydrodynamic load model and a modified wave model, analyze how the modified method affects foundation design.

1.2 Hywind Demo Project

Hywind, a concept from Statoil, is world's first spar type floating wind turbine. It was installed 12 *km* south east of Karmøy in Norway, at a water depth of about 220 *m* [6]. The hull and the tower of Hywind Demo is made of steel and blasted with gravel and water, with its major design parameters shown in table 1.1.

Table 1.1: *Technical data of Hywind Demo[2]*

Design Parameter	Value	Unit
Power	2.3	MW
Turbine Weight	138	tonnes
Rotor Diameter	82.4	m
Nacelle Height above MSL	65	m
Hull Draft	100	m
Diameter at Water Line	6	m
Diameter of Submerged Part	8.3	m
Water Depth	220	m
Displacement	$5,300$	tonnes

The Hydro Demo is composed of three parts, a spar type substructure, a tower and a wind turbine generator mounted at its top, refer to figure A.1. The substructure, hereon referred as the hull, is designed to support the wind turbine and maintains a desirable sea performance to ensure the operation of wind turbine. The hull is a 100 *m* steel cylinder with a diameter of 8.3 *m* at the immersed part, and a reduced diameter of 5 *m* at water surface to reduced hydrodynamic loading in wave zone. The hull is blasted with gravel and water to lower the center of gravity. Also, three mooring lines, anchored at sea, are attached to the hull at 52.3 m below MSL for positioning purposes. The turbine tower, with a total length of $46.54m$, acts as the link between the hull and WTG. WTG consists of three parts, a nacelle, a rotor and a generator. The wind turbine supplied by Siemens is a $SWT - 2.3 - 82$ with a rated power of 2.3 MW [6].

The following three tables illustrated the design parameters. Table 1.3 includes the mass distribution over height. Table 1.4 shows the concentrated weight of different parts of the structure, and the total weight. Table 1.5 gives the critical dynamic characteristics of the structures, including 6 DOF's rigid body modes and the lowest bending modes of the turbine tower.

Table 1.2: *Structural parameters for each segment of Hywind*

Section	**Range**	**Diameter** $[m]$	**Wall thickness**$[m]$
upper tower	27.5 $\sim$ 65.7	3.3	0.022
lower tower	17.0 $\sim$ 27.5	4.6	0.045
MS 1	11.0 $\sim$ 17.0	6.0	0.052
MS 2	–4.5 $\sim$ 11.0	6.0	0.052
MS 3	–18.4 $\sim$ –4.5	6.0	0.052
MS 4	–36.2 $\sim$ –18.4	7.8	0.052
MS 5	–51.0 $\sim$ –36.2	8.3	0.037
MS 6	–57.0 $\sim$ –51.0	8.3	0.038
MS 7	–68.8 $\sim$ –57.0	8.3	0.038
MS 8	–86.6 $\sim$ –68.8	8.3	0.038
MS 9	–99.3 $\sim$ –86.8	8.3	0.038

Table 1.3: *Hywind support structure mass distribution*

Section	**Range**	**Mass** $[tonnes]$	**Mass per unit length**$[tonnes/m]$
upper tower	27.5 $\sim$ 65.7	88.0	2.3
lower tower	17.0 $\sim$ 27.5	85.3	8.1
MS 1	11.0 $\sim$ 17.0	104.9	17.5
MS 2	–4.5 $\sim$ 11.0	153.4	9.9
MS 3	–18.4 $\sim$ –4.5	172.0	12.4
MS 4	–36.2 $\sim$ –18.4	173.7	9.8
MS 5	–51.0 $\sim$ –36.2	143.3	9.7
MS 6	–57.0 $\sim$ –51.0	96.4	16.1
MS 7	–68.8 $\sim$ –57.0	117.2	9.9
MS 8	–86.6 $\sim$ –68.8	1772.4	99.6
MS 9	–99.3 $\sim$ –86.8	2086.9	164.3

Table 1.4: *Siemens 2.3 MW turbine mass distribution*

Part	**Mass** $[tonnes]$
Hub	26.4
Nacelle	82.1
Blades	27.6
Sum	136.1

Table 1.5: *Natural frequencies of Hywind Demo [2]*

Mode of motion	**Measured value** $[Hz]$	**Simulated value** $[Hz]$
Surge/ sway	0.008	0.009
Roll /pitch	0.040	0.043
Heave	0.036	0.037
1st tower bending moment	0.699	0.690
2nd tower bending moment	1.667	1.639

1.3 Wave Forces

The wave forces acting on a marine unit can be classified into four areas as shown in figure 1.1 [7]. The ratio between cylinder diameter and incident wave length, $\frac{\lambda}{D}$, and ratio between wave height and cylinder diameter $\frac{H}{D}$ determine the governing wave loads type. Within the wave breaking limit, diffraction loads are dominating when $\frac{\lambda}{D}$ is smaller than 5, while for longer waves the mass forces become more important if $\frac{\lambda}{D} > 5$. Besides, viscous effects, such as flow separation and wake, need to be included if $\frac{H}{D}$ is sufficiently large.

In the context of the project, though a relatively large wave height is applied, breaking wave is not considered to simplify wave modeling. Also, as a slender structure with a large $\frac{\lambda}{D}$ ratio, it is assumed that mass forces is the dominating wave force type. It is thus justified to combine strip theory and long wave approximation for loads calculation, ignoring 2D effects and wave profile deformation.

In offshore wind industry, Morison Equation is widely applied to calculate the hydrodynamic loads. This semi-empirical load formula considers two parts, one inertia term and one drag term. The inertia term serves to count for the diffraction problem, assuming the relevant characteristic length L is smaller than the wave length, i.e. $KL \ll O(1)$. This long wave assumption leads to the simple conclusion that the horizontal wave force acting locally on a fixed body is proportional to the acceleration of the incident-wave velocity field at the same position. Morison's equation also assumes that viscous drag dominates in drag loading, and that wave radiation damping can be ignored. Concluded by Rainey [8], Morison equation is applicable for limiting cases of small lattice-member diameter, and deals entirely in member-center line fluid properties, so that it can be applied computationally by a simple 'stick model' computer program. Morison equation will be treated with in more detail in 2.1.1

In the offshore wind industry, integrated wind turbine design codes employ the Morison Equation for calculating hydrodynamic loads for its simplicity and high efficiency. When

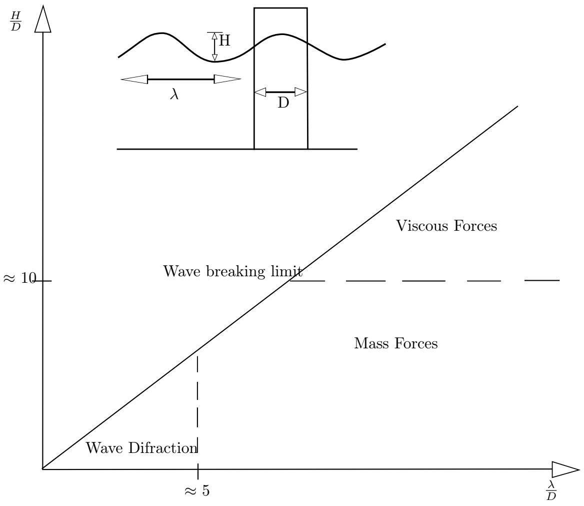

Figure 1.1: *Classification of wave forces*
[7]

it comes to analyzing floating support structure, its disadvantages is well pointed out by Matha et al. [9]. However, when the structural characteristic length is comparable to wave length, which is always the case for floating wind, and causes noticeable disturbance to incident wave, wave potential should not be assumed to be constant over piecing surface and leads to the failure of diffraction simplification in Morision Equation. Also, they indicate that for floating hull with accountable displacement, the radiation damping should be also included in analysis and the simplification that viscous drag dominates the drag loading is no longer valid. Another issue they noted is that the equation does not take account of any added mass induced coupling between hydrodynamic force and support structure in all DOF's, as the wind structure is no longer as axisymmetric as assumed in Morison equation.

Apart from the limitations of Morison's Equation, some nonlinear phenomenon, such as the ringing effects, see figure 1.2 [10], and springing, can not be explained when higher order terms are excluded. These higher order phenomenon have arouse recognition on nonlinear wave loads since late 1980's, in order to explain transient structural deflection beyond dominant wave frequencies. Since the hull of Hywind Demo has a relatively large draft-diameter ratio and can thus be treated as a slender cylinder with a low natural frequency, the higher order response might be excited by nonlinear wave components. A recent study performed by Lucas [11] on the comparison of first- and second-order hydrodynamics confirms the importance of second-order effects for an FOWT [9]. But few efforts have been paid to analyze higher order effects, to third or fourth order, when the floater is slender and subject to steep waves.

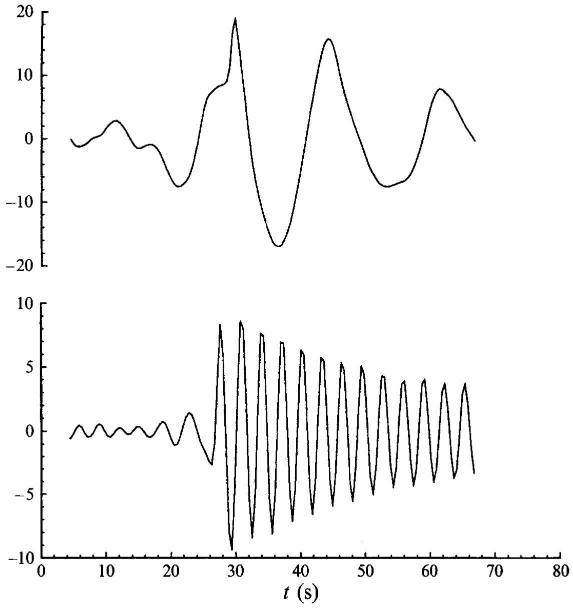

Figure 1.2: *Springing phenomenon*

1.4 Nonlinear Phenomena

Slamming

Slamming is a non-linear fluid-structure interaction that affects not only local structure integrity, but also its global elastic behavior. When it comes to the substructure of Hywind, the slamming loads acting at the wave intersection might have great concern with regard to its fatigue life and local strength. Two parameters, relative impact angle or dead-rise angle, and the relative attacking velocity, the relative structure-liquid velocity at the impact, determine the level of slamming loads.

Ringing

Ringing is a high-frequency transient response caused by large and steep waves. These transient oscillations at frequencies substantially higher than wave frequencies were first observed in some tension leg platforms and gravity based structure in North Sea during 1980's. Similar problems can also occur to fixed platforms in deep waters, which has a relatively high natural frequency.

Ringing is believed to be a third order effect, as the natural frequency of those structures were approximately three times the wave frequency. It tends to be excited in a steep wave with the wave amplitude comparable to structure radius. This phenomenon can not be explained by traditional wave diffraction theory. Since this issue first came into sights, great efforts have been paid to explain the rationale behind this in the last two decades. One such example is FNV-theory introduced by Faltinsen et al. [10] that enables to include a third order term in the formula. By introducing a inner domain and outer domain, FNV-theory is valid for wave height comparable to cylinder radius. This method will be explained in detail in chapter 2. Another approach is presented by Malenica and Molin [12] by applying the conventional perturbation technique and derived the complete third order potential for a fixed cylinder in finite water depth. In contrast to FNV-theory, as a standard procedure, the wave height is assumed to be small compared with other length scales. Also, Rainey [8] invented a new method to calculate wave loads on a slender structure. Instead of directly integrating pressure over the submerged surface, Rainey's new formula is based on energy conservation, which will also be elaborated in chapter 2.

Springing

Springing is a steady state resonance phenomena that affects the fatigue level of the structure. Springing is normally excited by second order loads, which lies outside the range of linear forces. It has been observed that springing effects can cause resonant axial deflection of the tendons.

1.5 Objectives

To study the above described non-linear phenomena that might occur at a severe sea state, both improved hydrodynamic load model and a more sophisticated wave model shall be proposed. Besides, how the improved hydrodynamic model affects static loads of a bottom founded slender offshore support structure, and dynamic response of a floating wind turbine shall also be investigated. The study thus concentrates on following areas,

1. Hydrodynamic load model, focusing on proposing improved loads model to solve wave-structure interaction at a steep wave;
2. Higher order wave models that includes a certain level of non-linearity at low computation cost;
3. Static load calculation to investigate into statistic properties of loads estimated with various loads models;
4. Higher order wave model on the dynamic of Hywind and its influence on extreme loads estimation, and fatigue design.

Chapter 2

Hydrodynamic Model

To capture the non-linearity resulting from steep waves, it would be straight forward to investigate into both non-linear wave model and sea loads calculation model. In this chapter, the prior focus will be on the state of the art in offshore wind design codes, and a comparative study of more sophisticated load models.

2.1 State of the art

2.1.1 Morison equation

In offshore wind design codes, Morison equation is widely employed for its convenience in implementation and high calculation efficiency. Morision equation is a semi-empirical method that calculates the sea loads as the sum of quasi-static inertia and drag force, which has the form,

$$dF = C_A \rho \pi \frac{D^2}{4} \dot{u} dz + C_D \rho \frac{D}{2} |u| u dz \tag{2.1}$$

in which C_D and C_A are drag coefficient and mass coefficient, $\dot{u}$ and u are the water particle acceleration and velocity at the cylinder center in x direction. The two coefficients C_A and C_D are determined empirically, depending on Keuligan-Carpenter number, Reynolds number, roughness and some other parameters.

For a floating wind turbine, which is free to move in 6 DOFs, the Morison equation needs to be expanded to account for the relative motion between the structure and wave. Equation 2.1 needs to be modified as,

$$dF = C_A \frac{D^2}{4} \rho \pi \dot{u} dz - C_A \frac{D^2}{4} \rho \pi \ddot{\eta} dz + C_D \rho \frac{D}{2} |u - \dot{\eta}| (u - \dot{\eta}) dz \tag{2.2}$$

in which $\dot{\eta}$ and $\ddot{\eta}$ are velocity and acceleration of the floating substructure. Combined with strip theory, the wave loads can be conveniently obtained by integrating dF over its length ‘L’ i.e.

$$F_{total} = \int_0^L dF \tag{2.3}$$

Morision equation is based on the assumption that the structure is slender in comparison to wave length λ. The structure will not deform the wave profile. Pressure and velocity fields around the structure remain as they are in the far field. Wave particle velocity and acceleration at the center line are used in calculation, i.e. long wave assumption is assumed.

By writing the drag term in Fourier series, higher order components, but odd frequency terms only, i.e. $\omega,\ 3\omega,\ 5\omega$, are found in the second part of the formula, which can be one source for non-linearity.

For Hywind Demo, the long wave assumption can be easily justified, so long as the wave length is larger than $5D$. The limitation of using Morison equation mainly lies on the integration method, since it ignores the free surface piecing effect at the wave-structure intersection. Besides, when applied in combination with linear wave theory, the integration is carried out to mean free surface, $z = 0$. In that way, it fails to capture the nonlinearities above the mean water surface. Though stretching method to some extent adds wave zone loads to the expression as a engineering remedy, its physical rationale remains to be proved. Also, it is reported that stretching methods, such as Wheeler stretching, significantly underestimate velocities with the error ranging from $0.5KA$ to $0.75KA$ [13] for steep waves. A more sophisticated model is thus in need.

2.1.2 Stretching

Though not recommended in the context of extreme wave, streching method will still be briefly introduced for comparison purposes. The most often utilized technique is the Wheeler stretching that ‘stretches’ the vertical coordinates from the original level z_s to a modified level z:

$$z = \frac{z_s - \zeta}{1 + \frac{\zeta}{h}} \tag{2.4}$$

where ζ is free surface elevation and h is the water depth. Figure 2.1[14] clearly illustrates the procedure. Intuitively, this stretching method works to transform the linear wave velocities up and down to the wave crest or trough. First order solution is correct to MSL, the stretching method will significantly reduce velocity under a wave crest of an extreme wave.

Besides, pointed out by Wheeler, the coordinates are shifted to proximate the particle velocity in stretching, which makes the solution fail to satisfy Laplace equation. Significant errors occur especially when applied in combination with steep waves and linear wave theory. Further, Larsen et al. [15] concluded that due to asymmetry in loading, stretching method underestimate fatigue damage, and shall not be preferred for fatigue analysis. A more sophisticated wave kinematic model is in need to capture non-linearity included in the wave zone.

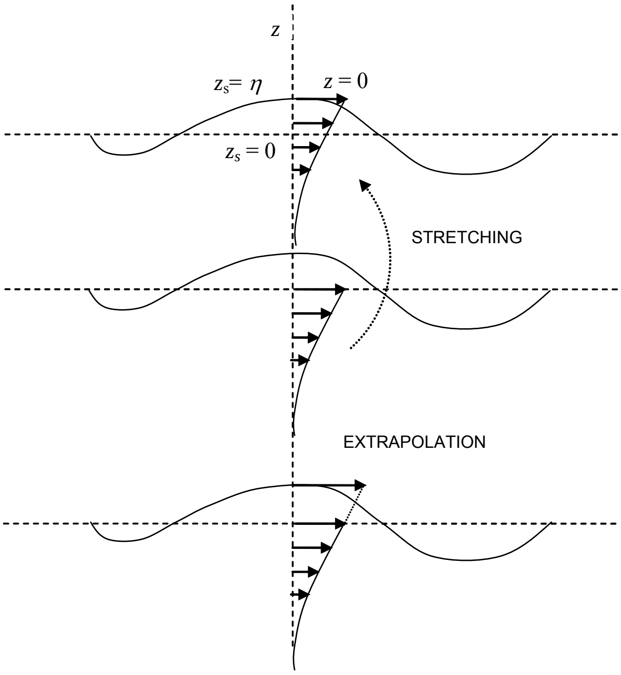

Figure 2.1: Wheeler stretching
[14]

2.2 Wave Model

In Stokes waves derivations, perturbation method is a commonly used technique to solve the potential problem. When a Taylor expansion is applied at $z = 0$, the boundary condition problem for wave potential can be linearized as,

$$\Phi(x, y, \zeta, t) = \Phi(x, y, 0, t) + \zeta \left(\frac{\partial \Phi}{\partial z} \right) \tag{2.5}$$

When a linearized boundary condition is applied, the solved linear potential will be valid up to the mean free surface and is assumed to be constant from $z = 0$ to $z = \zeta$. To use the linear potential theory consistently, wave forces is integrated up to mean free surface as well. It can be justified for a benign wave condition, where the wave surface elevation is relatively small. But for an extreme sea state, wave kinematics in the wave zone is expected to be included in calculation, in order to describe wave zone loads, which include a non-negligible part of the total wave load.

One widely applied remedy is Wheeler stretching, explained in section 2.1.2. Alternatives are, higher order wave models, 2nd order irregular sea model and stream theory.

2.2.1 Higher order Stokes

When applying perturbation techniques, the velocity potential can be expressed as,

$$\Phi = \Phi_1 \epsilon + \Phi_2 \epsilon^2 + \Phi_3 \epsilon^3 + \cdots \tag{2.6}$$

The accuracy of the potential problem increases when more higher order terms are added, see equation 2.7. The derived higher order solution has its advantage in better predicting extreme loads for design purposes.

$$\Phi(x, y, z = \zeta, t) = \Phi(x, y, 0, t) + \zeta \left(\frac{\partial \phi}{\partial z} \right) + \frac{1}{2} \zeta^2 \left(\frac{\partial^2 \phi}{\partial^2 z} \right) \tag{2.7}$$

But the accuracy is achieved at the cost of loosing its superposition property. For a linearized potential problem, superposition technique is applicable to represent the real sea state as the sum of a group of linear waves characterized by varying wave frequencies. But when higher order terms included, superposition is not valid any more.

Besides, the perturbation method requires wave amplitude to be smaller than all the other length scales to be valid. When the wave steepness is large, for example wave amplitude of the same order of cylinder diameter, the results from Stokes waves may diverge. Rainey [16] discussed this in detail in its appendix.

Despite of the two above mentioned shortcomings, higher order Stokes still have its advantage in studying nonlinear wave kinematics for its more sophisticated description of wave kinematics in the wave zone. But its applicability is constrained by two parameters, water depth and wave height. As a general guidance, the more higher order terms included, the better approximation to the 'real' wave.

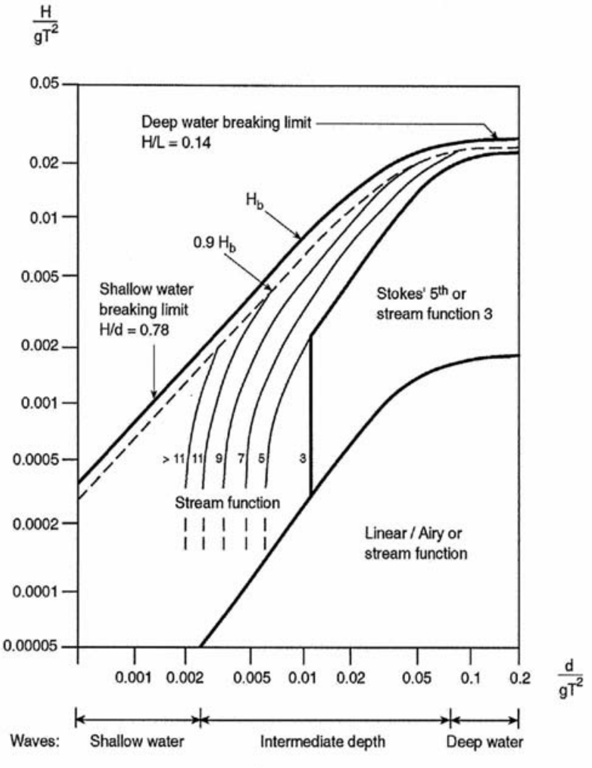

Figure 2.2: *Guidance for stream function order*
[5]

2.2.2 Stream function

Stream function is a purely numerical procedure for approximating a given wave profile, which has a broader range of validity than Stokes waves[5]. A stream function wave solution has a general form,

$$\Psi(x,z) = cz + \sum_{n=1}^{N} X(n)\sinh(nk(z+h))\cos(nkx)[5] \tag{2.8}$$

where c is the wave celerity. N is the order aimed at when applying stream function. The targeted order N is determined by the wave parameter steepness, S, and shallow water parameter, μ. When N is chosen to be 1, the stream function theory leads to the same result as linearized first order problem. The closer to the breaking wave limit, the more terms should be included in order to give an accurate representation of the wave profile. $X(n)$ is the coefficient for each order that is required to satisfy the dynamic free surface condition at its order. Figure 2.2 provides some guidance on selecting stream function order over Stokes waves.

Stream function has its advantage in describing steep waves that are close to breaking limit, for its high accuracy achieved by increasing N. However, when using stream function theory, the incident wave height, water depth and wave period are required to be determinant. Due to the stochastic nature of a real sea state, stream function is not ideal for design purposes. But it can help to predict the loading in extreme states.

2.2.3 Second order irregular wave

A irregular wave model that enables the realization of stochastic of a sea state will be a better targeted solution, in comparison with the above mentioned methods. The simplest non-linear random wave model is the long-crested second-order model, where the second-order wave process has N^2 corrections spreading over all sum-frequencies and another N^2 corrections terms covering all difference frequencies.

Longuett-Higgins invented a simple nonlinear random wave model for long crested second order waves, which is expressed as,

$$\begin{aligned}\zeta^{(2)} &= \sum_{n=1}^{N}\sum_{m=1}^{N} A_m A_n B_{mn}^{+} \cos[(\omega_m + \omega_n)t + (\varepsilon_m + \varepsilon_n)] \\ &+ \sum_{n=1}^{N}\sum_{m=1}^{N} A_m A_n B_{mn}^{-} \cos[(\omega_m - \omega_n)t + (\varepsilon_m - \varepsilon_n)]\end{aligned} \tag{2.9}$$

where $B_{mn}^{\pm} = B^{\pm}(\omega_m, \omega_n)$ are quadratic surface elevation transfer functions. The wave is modeled by including additional N^2 terms to include sum frequencies and difference frequencies terms all over the complete frequency spectrum. As the only method that better describes the stochastic nature of a real sea state in a convenient manner, this model will be selected and treated in detail in the subsequent analysis in chapter 3.

2.2.4 Fully nonlinear model

In Marino et al. [17], a fully nonlinear wave model is developed to model breaking waves, which is called a mixed-Eulerian-Lagrangian approach. There are two steps involved in this procedure. First, the potential problem is solved using a boundary element method at time t. Then the free surface is stepped forward in time by a distance of δt by using a Taylor expansion in time. Afterwards the boundary value problem is again solved using the same boundary element method as in the first step, before continuing with the next time step. Non-linear wave can also be modeled with Boussinesq, see Madsen et al. [18], but at a rather high computation cost.

2.2.5 Kinematics

Recommended in DNV guidelines [14], wave kinematics in irregular waves can be predicted by one of the following methods,

1. Grue's method
2. Wheeler's method
3. Second order kinematics model

Grue's method introduces a nonlinear dispersion relationship and a non-dimensional free surface elevation, i.e.

$$\begin{aligned} \frac{\omega^2}{gk} &= 1+\varepsilon^2 && (2.10) \\ k\eta_m &= \varepsilon + \frac{1}{2}\varepsilon^2 + \frac{1}{2}\varepsilon^3 && (2.11) \end{aligned}$$

The horizontal velocity under the crest is given by the exponential profile

$$u(z) = \varepsilon\sqrt{\frac{g}{k}}e^{kz} \qquad (2.12)$$

where $z = 0$ is the mean water level and g is the acceleration of gravity. But the validity is limited to crest kinematics and deep water.

Wheeler's streching has been elaborated in section 2.1.2.

Horizontal velocities can also be consistently modeled up to the free surface elevation with a second-order kinematics model, which is a Taylor expansion of the linear velocity profile, including contributions from sum and difference frequency wave components. The horizontal velocity under a crest is given as,

$$\begin{aligned} u^{(2)}(z) &= u^{(1)}(z) + u^{(2+)}(z) + u^{(2-)}(z), \quad for z \leq 0 && (2.13) \\ u^{(2)}(z) &= u^{(1)}(0) + \frac{\partial u^{(1)}}{\partial z}\mid_{z=0} z + u^{(2+)}(0) + u^{(2-)}(0), \quad for z > 0 && (2.14) \end{aligned}$$

where $u^{(1)}(z)$, $u^{(2+)}(z)$ and $u^{(2-)}(z)$ are the linear, second order sum and difference frequency velocity profiles.

Stansberg [14] compared the above mentioned of three methods for predicting wave kinematics under an extreme wave and came the conclusions that:

1. Grues method well predicts the wave kinematics for $z > 0$, but it arrived at a too large velocity for the part below mean free surface.
2. The second-order kinematics model performs the best for all z-levels of a steep waves in deep water.
3. Wheelers method under predicts the values at positions around $z = 0$ as well as at lower levels.

2.3 Sea loads models

Wave loads also utilizes perturbation method, which allows it to obtain first order loads proportional to wave height and second order loads squared to wave height. But in case that the waves are sufficiently steep, Stokes expansion will diverge even without any cylinder interaction, as explained by Rainey [16]. To capture higher order terms, one possibility is to apply FNV-theory that introduces a innovative perturbation scheme on the horizontal plane moving up and down with the first order incident wave. An alternative is 'slender body theory' introduced by Rainey [16], in which the Stokes expansion parameter is replaced by the slenderness parameter. The key in his derivation is energy conservation.

2.3.1 The FNV-theory

To explain the third order effects on TLP, O.M. Faltinsen, J.N.Newman, and T.Vinje presented an innovative theory that allows to include the third order harmonic terms in the expression for loads on a fixed flexible cylinder. Similar as the general method that solves the diffraction problem, assumptions are made that both wave amplitude A and cylinder radius a are small compared to the wave length. But instead of further assuming small wave elevation, A and a can actually be of the same order in their derivation, which makes the theory applicable to a extreme wave condition of the same order of structure diameter.

The diffraction problem is subsequently divided into two domains, an outer domain and an inner domain. In the outer domain, the conventional linear analysis can be justified, when the wave slope is small. However significant nonlinear effects are present in the inner domain, associated with the free-surface boundary condition. Thus the perturbation is applied at the free surface, instead of $z = 0$ for a conventional analysis. The rationale behind this is that *the leading-order nonlinear contribution to the velocity potential includes terms proportional to both* A^2a *and* A^3*.The wave load which acts on the cylinder near the free surface includes second- and third-harmonic components which are proportional* *respectively to A^2a^2 and A^3a. In a conventional perturbation analysis, where $A \ll a$, these components would be ordered in magnitude corresponding to the different powers of A, but here they are of the same order*[10] for a condition A and a are of the same order.

Wave loads

With boundary-value problem solved, it is possible to evaluate the wave loads acting on the cylinder. Following [10], the expression for the force is given as,

$$F_x = \rho a \int_0^{2\pi} \cos\theta d\theta \int_{-\infty}^{0} (\Phi_t + \frac{1}{2}V^2)_{r=a} dz + \rho a \int_0^{2\pi} \cos\theta d\theta \int_0^{\zeta} (\Phi_t + \frac{1}{2}V^2 + gz)_{r=a} dz \tag{2.15}$$

In the integration of the first part up to $z = 0$, the first order contribution can be obtained from the total linear diffraction potential,

$$F_1' = \rho a \int_0^{2\pi} \Phi_{Dt} \cos\theta d\theta = 2\pi\rho g K A a^2 e^{Kz} \cos\omega t \tag{2.16}$$

This is the first order component acting on unit length along the cylinder. The expression is exactly the same as inertia force term in Morison's equation.

The second order component is given by integrating the squared term in Bernoulli equation,

$$F_2' = \frac{1}{2}\rho a \int_0^{2\pi} (\bigtriangledown\Phi_D)^2 \cos\theta d\theta = \frac{1}{2}\pi\rho g K^2 A^2 a^2 e^{2Kz} \sin 2\omega t \tag{2.17}$$

For the second integral in equation 2.15, integration is carried out between the planes $z = 0$ and $z = \zeta_1 = A\sin\omega t$ by evaluating 2.16 and 2.17 respectively. For the remaining portion between $z = \zeta_1$ and the exact free surface $z = \zeta$, the pressure is approximated as hydro-static.

The wave loads contributions from linear potential Φ_D is thus formulated as,

$$F_x^D = 2\pi\rho g a^2 A \cos\omega t + \frac{5}{4}\pi\rho g K a^2 A^2 \sin 2\omega t - \pi\rho g K^2 a^2 A^3 \cos 3\omega t + O(\epsilon^6) \tag{2.18}$$

The nonlinear potential also gives a contribution to nonlinear loads,

$$F_x^{\psi} = \pi\rho g K^2 a^2 A^3 (\cos\omega t - \cos 3\omega t) + O(\epsilon^6) \tag{2.19}$$

Adding linear and nonlinear components, i.e. 2.18 and 2.19, gives the total point force F_x acting on the intersection,

$$F_x = \pi\rho g K a^2 A^2 \sin 2\omega t + \pi\rho g K^2 a^2 A^3 (\cos\omega t - 2\cos 3\omega t) + O(\epsilon^6) \tag{2.20}$$

As is noticed above, linear potential ϕ_D and the higher order potential ψ equally contribute to the third harmonic component in the expression of the total point force. Faltinsen *et al.* argues that *Third-order load is attenuated more rapidly with negligible contributions below a depth comparable to the cylinder diameter.*[10] Besides, *The third-order load is represented in terms of the normalized vertical coordinate,which moves up and down with the undisturbed incident wave. Thus it is appropriate to think of this load as acting locally at the free surface point forces which are concentrated in the vicinity of the free surface.*[10]

In addition, there is a fourth order harmonic contribution, if the moment due to the higher order loads is calculated about a fixed point,

$$M = -\pi \rho g K^2 a^2 A^4 \sin 4\omega t \tag{2.21}$$

2.3.2 Rainey's new equation

Contrary to FNV-theory that applies direct surface pressure integration, Rainey's method is derived from fluid kinetic energy, which requires a lower level understanding of flow details. The proposed method *is inherently more efficient, in that a simple 2D flow idealization can be used, which would not be sufficient for pressure integration purposes for* the FNV theory. The new equation is formulated as an improvement for the inertia term of Morision equation, although the accuracy gained is somehow offset by the level of uncertainty over the prediction of vorticity-induced loads.

In Rainey's derivation [8], the water surface is assumed to be contained by a 'wavy lid' in the shape of the incident wave, so that the wave is assumed not to be distorted by the cylinder. One of the greatest advantage of the 'wavy lid' assumption is that it does not put any restrictions on the incident waves. In other words, the incident wave can be fully nonlinear or even breaking. By assuming this, *it removes the free-surface degrees of freedom from the problem, so that it can be tackled by classical energy arguments.* This is the simplest limiting case by assuming non distorted wave surface. A more sophisticated 'distorted wavy lid' is also derived at a later time by Rainey [16] to add its contributions to the loads at the intersection.

Another assumption made in the derivation is that the structure members can be treated as slender, i.e. that the diameter is small compared with all the other relative length. As a basic rule, the wavelength is required to be at least ten times the cylinder diameter. Or else, serious error occurs due to the significant contribution from 'microseism effect'.

Based on two assumption made above, the slender body theory can be developed applying energy conservation. But both the derivation and reasoning are quite lengthy and not straightforward in Rainey [8]. The method is generalized to a moving structure at a later phase by Rainey. The results deduced from the new theory is surprisingly simple and can be easily applied for engineering purposes.

The results show that there are mainly four contributions to wave loads based on Rainey's theory,

Force per unit immersed length

For a circular cylinder with the cross-sectional area of $\frac{\pi D^2}{4}$, the distributed loads for unit immersed length has the form,

$$dF_1 = \rho \frac{\pi D^2}{4}(a-g)_t + \mathbf{M}\left[a + (l \cdot \mathbf{V}l)w\right] - \mathbf{M}\dot{u} - 2\mathbf{M}\boldsymbol{\Omega}w_a \tag{2.22}$$

in expression 2.22, the bold sns-serif capitals denote matrices, while bold letters are vectors. a is the particle acceleration including convective terms, with the expression $a = \partial v/\partial t + \mathbf{V}v$. $\mathbf{V}$ and v are velocity gradient matrices and velocity of the incident wave, respectively. u is the velocity of the structure at a specified point along the body, i.e. $u = u_0 + \Omega \times r$. $\mathbf{M}$ is the added mass matrix. l is a unit vector along the structure, and $\boldsymbol{\Omega}$ is defined as $\boldsymbol{\Omega}x = \omega \times x$.The suffixes a and t denotes axial and transverse components. w is the relative velocity defined as $w = v - u$. $g = -ge_z$, i.e. it points downwards.

Point loads at joints

In addition to unit forces at each segment, each element produces a point loads at its end. For the Hywind hull, there will be a point force at its immersed end, which can be calculated as,

$$F_2 = \left(\frac{1}{2}w \cdot \mathbf{M}w - \frac{\pi D^2}{4}p\right) l - (l \cdot w)\,\mathbf{M}w \tag{2.23}$$

where p is the pressure term, including both hydrodynamic and static components. All the other terms in equation 2.23 are defined in the same way as in equation 2.22. The pressure term can be interpreted as the axial buoyancy and provides static restoring force. The terms associated with velocity squared can be seen as a second order component of the wave force.

Point loads at surface intersection

The point load at the intersection is actually of greater interest within the scope o this project. Is is written as,

$$F_3 = \frac{1}{2}\tan(\alpha)\left[(t \cdot w)\,\mathbf{M}w - (t \cdot (l \times \mathbf{M}w))\right] \tag{2.24}$$

where α is the acute angle between the cylinder centerline and the surface normal to the incident wave; and t is a unit vector at the joint plane, normal to the centerline and pointing out of the fluid. For a large wave, the wave slope will be large as well for a vertical structure and results in a slamming loads. See from the expression, the intersection load grows with the increase of the angle. Thus it has the potential to approximate slamming loads when the intersection angle α is large. For a smaller angle, it can be used to predict the ‘ringing’ of offshore structures, since it is shown by Rainey that this force are at least third order of the wave height.

Rainey also carried out an error analysis of the simple ‘wavy lid’ assumption. When the order of the wave defined in the same way as Stokes expansion, i.e. based on the order to the wave height, the error introduced by the wavy lid is of third order. And that it is accurate to the first and second order.

The drag force per unit length can be calculated in the same way as in Morison equation to include the viscous effects,

$$dF_{drag} = \rho D C_D w_n |w_n| \tag{2.25}$$

2.3.3 Alternatives

Nestegård et al. [19] also proposed a method to calculate loads in the wave zone, defined as slamming loads in the analysis. The sectional slamming loads is dependent on the changing rate of added mass, which has the expression,

$$F_x(z,t) = \frac{d}{dt}\left[A^{2D}(t,z)u\right] = \frac{d}{ds}\left[A^{2D}(s,z)u^2\right] \tag{2.26}$$

where A^{2D} is the high-frequency limit of the added mass for a 2D cylindrical section as a function of submergence length s, and u is relative velocity between particle velocity of wave and cylinder. For a steep wave, the slamming loads can be approximated as following,

$$F_x(z,t) = \frac{1}{2}\rho C_s D u^2 \tag{2.27}$$

$$C_s(s) = 5.15\left[\frac{D}{D+19s} + \frac{0.107s}{D}\right] \tag{2.28}$$

the empirical coefficients are proposed by Campbell and Weynberg [20] based on experiment results.

Malenica and Molin [12] also applied a conventional perturbation to the third order and deduced a third order wave loads that explains the ringing effects. But the method is mathematically laborious and tends to diverge at high wave height.

2.3.4 Comparison

FNV-theory provides a method to estimate higher order loads acting on a fixed flexible cylinder when the wave amplitude is comparable to cylinder diameter. In the analysis, wave slope is assumed to be small and wave length is long compare to the characteristic length of the structure. To analyze the elastic response of Hywind, the explicit expression equation 2.17 is not applicable any more, since the floating structure has 6 DOFs. However, a numerical method can be applied to analyze the problem in the time domain, with the higher order loads evaluated at each time step, taking into consideration the relative motion between wave and the structure. Also, by applying Newman’s method, it is possible to extend FNV-theory to a more practical case of unidirectional irregular waves. However, FNV model is applicable to deep water condition, where the pressure field is not significantly affected by sea bed. Also, first order regular wave model, developed by Stokes expansion, is assumed in derivation with higher order terms implemented as a correction to account the true free surface in the inner domain. Highly nonlinear effects in the incident waves are ignored in FNV.

When Rainey's 'slender body theory' is applied on a vertical cylinder, the point load at the water surface intersection is only one eighth of that in FNV-theory. The difference, as explained by Jefferey, is due to the rate of change the energy stored in the surface distortion. If corrected, two models actually produces exactly the same results. However, while FNV-theory is derived for a fixed cylinder, Rainey's equation is applicable to more general cases of an arbitrarily moving structure with arbitrary cross-sectional shapes. Also, Rainey's methods has a broader application as is can be used even when the wave is breaking. Rainey's method seems to be the best available solution, since it allows for the implement of fully nonlinear wave model and include nonlinear components in the incident wave.

However, Chaplin et al. [21] argues that Rainey's method will be an attractive solution, without considering the surface distortion, when either of the following conditions is satisfied,

1. $D > L/10$
2. $D > relative\ fluid\ motion/5$
3. $D > structure\ motion\ raduis/20$
4. $D > \lambda/30$

The first condition is not satisfied for Hywind, as the length of the structure is about 16 times the cylinder diameter. Rainey's method still seems to be promising since the other three conditions are not too demanding.

Nestegård et al. [19] method is empirical. It will be preferred only when the wave steepness is rather large and slamming tends to occur. Malenica and Molin is not considered here is this case due to its complexity in application.

2.4 Preliminary calculations

The preliminary calculations are based on free-free beam model for hywind, refer to Appendix C.

2.4.1 FNV-theory

The point loads acting at the intersection has the expression that,

$$F_x = \pi\rho g K a^2 A^2 \sin 2\omega t + \pi\rho g K^2 a^2 A^3 (\cos\omega t - 2\cos 3\omega t) + O(\epsilon^6) \tag{2.29}$$

Since the derivation is done for a fixed cylinder at deep water, the analysis is first carried out assuming the rigid body motion of Hywind to be restrained. Consequently, a larger relative motion between wave and the structure is included in the analysis. But the trend observed in analysis will still of value in predicting the elastic response of the structure due to non-linear components included in wave zone.

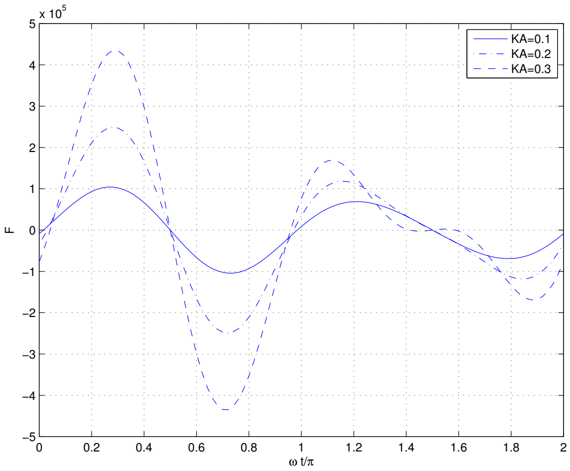

Figure 2.3: *Total point loads*

Figure 2.3 shows the wave loads act at the intersection in one wave period. Different KA value, defined as wave steepness, is applied in analysis. See from the figure, for small value of wave steepness, there is only slight difference from the first order solution. The relative importance of the third order forces increases with KA. For $\omega t < \pi$, the higher order components tend to increase the magnitude of the total loads, while in the second half of the cycle cancellation effects are dominant.

For simplicity concerns, a linear incident wave, defined as $\zeta = A\sin(\omega t)$, is introduced. The dynamic response analysis are based on modal analysis in Appendix C, with the following assumptions made,

1. Floating wind turbine is constrained from moving;
2. Wave amplitude is set to be the same size as cylinder diameter at the intersection, i.e. $A = a = 3.0\ m$;
3. Load in the wave zone is taken as a point load, as argued by Faltisen;

See from figure 2.4, the elastic deformation is dominated by the lowest eigenmode, with the largest deformation appearing at two ends of the cylinder. Based on assumptions made above, dynamic response will be dependent on wave number K only, since wave height is set to be a constant. It will be of interest to see its trend with the variation of KA. Illustrated in figure 2.5, resonance of the lowest eigen mode is excited by the third order wave loads at around $KA = 0.6$, where incident wave frequency is one third

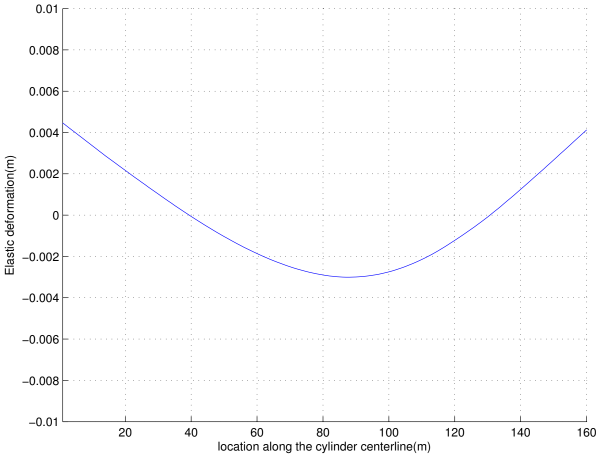

Figure 2.4: *Elastic response along the center line,* $KA = 0.1$

of the lowest eigenfrequency of the cylindrical hull. At resonance, the amplitude of elastic deformation is around 0.5 m, which is about 8% of the structure diameter.

The ratio between magnitude of resultant dynamic response to A^3 can be seen as RAO, when looking into third orde resonance. See from figure 2.6, it is obvious that third order contributions are dominant, exhibiting a high peak at $kA = 0.6$. The divergence of the lines is because of second order terms in equation 2.29. The second lowest eigenmode of Hywind is expected to be excited at $KA > 1$. But the importance of second order contributions reduce with the increase of wave amplitude.

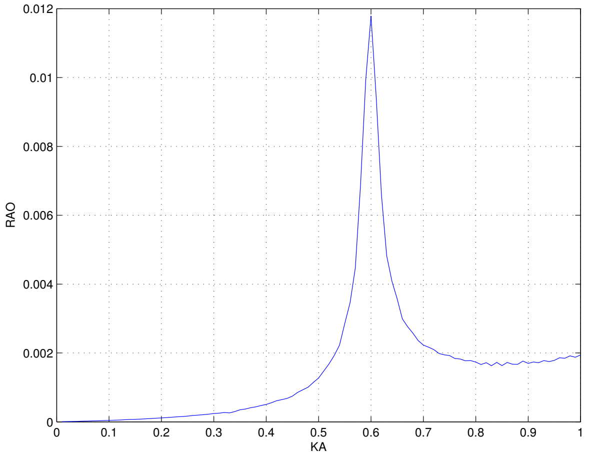

Figure 2.5: *Elastic response of cylinder hull*

Since FNV-theory is applicable to non-breaking waves only, the above mentioned resonance excitation condition remains to see whether the critical wave condition is within breaking limit. For a deep water site, breaking occurs when the wave steepness, $2A/\lambda$ is

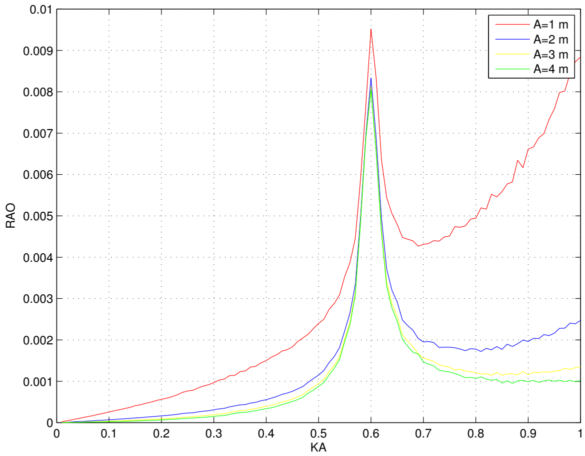

Figure 2.6: *RAO at different wave amplitude*

approximately 0.14, i.e. $KA < 0.439$. When wave amplitude is set to be $A = 3.0\ m$, the higher order resonance, ringing, might not be excited due to wave-breaking. Based on this, FNV-theory is not the most desirable tool for calculating non-linear loads in wave zone.

2.4.2 Rainey's new equation

To compare with FNV method, Rainey's slender body theory is applied on Hywind substructure with rigid body DOFs constrained as well. Though there are five components derived in Rainey equation, only the point load at the intersection is of interest in analyzing the elastic response of the cylindrical hull when rigid body mode is restrained,

$$F_3 = \frac{1}{2}\tan(\alpha)\left[(t\cdot w)\,\mathbf{M}w - (t\cdot(l\times\mathbf{M}w))\right][22] \tag{2.30}$$

can be simplified as,

$$F_3 = \frac{1}{8}\pi\rho a^2 C_A K A^3\omega^2\left(\cos(\omega t) - \cos(3\omega t)\right) \tag{2.31}$$

in derivation, first order potential is introduced, ignoring higher order contributions with all the terms expressed considering first order potential with a regular incident wave written as,

$$\zeta = A\sin(\omega t - Kx) \tag{2.32}$$

and the corresponding first order velocity potential,

$$\Phi_1 = \frac{gA}{\omega}\frac{\cosh K(z+h)}{\cosh Kh}\cos\left(\omega t - Kx\right) \tag{2.33}$$

Figure 2.7 shows how the point loads at the intersection varies with the elapse of time. In the analysis, the wave steepness KA is taken as 0.1, with the wave amplitude set to be

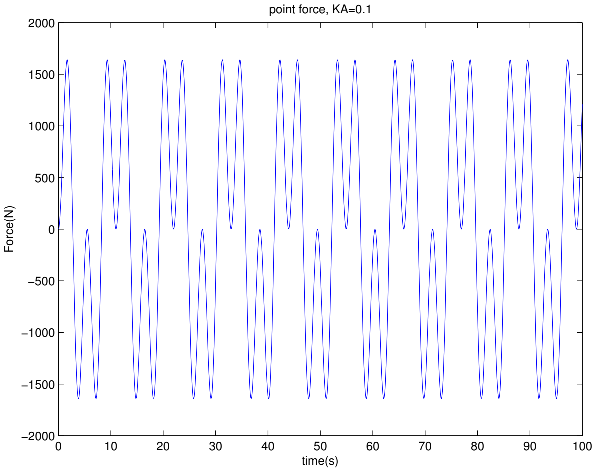

Figure 2.7: *Point force,Rainey's Method,* $KA = 0.1$

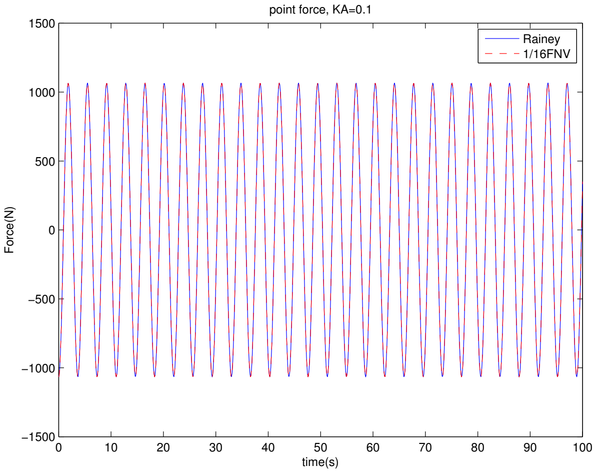

Figure 2.8: *Third order contributions, comparison between Rainey and FNV's method,* $KA = 0.1$

the same as cylinder radius. Contributions from third order effects are clearly indicated in the figure. The third order components tends to increase the load magnitude during the first half of the wave period and poses a canceling effect during the second half of the cycle.

Rainey's results are obviously a lot smaller than FNV solution. The reason are mainly three folds. One is that, in FNV there are second order contributions included as a point loads, while in Rainey, there are first and third order components only. Besides, corrections are included to describe the real free surface in FNV, which doubles the nonlinear loads at the intersection. Further, free surface distortion, which adds to the nonlinear loads at the intersection, is also ignored in Rainey's derivation. Figure 2.8 compares the third order contributions in two theories. Two lines in the figure overlap, indicating Rainey's result to be 1/16 of FNV. But if FNV considers first order potential only, the difference will be reduced to 1/8. The difference is explained in detail in Rainey [16].

Rainey's method will be preferred over FNV, due to following considerations,

1. Rainey asks for less information about incident waves, which makes it applicable even for a breaking wave case and shallow water site while FNV assume deep water unbreaking wave condition;
2. Rainey's method is derived for a floating slender structure, while FNV are targeted at fixed structure sited at deep water;
3. Rainey's equation also accounts forces at member joint, which is another source of non-linearity.

It should also be noticed that the resonance of the lowest eignmode will hardly be excited. The cylinder hull of Hywind is still relatively stiff, though it maintains a small D/L ratio. Resonance occurs at $KA = 0.6$, which is normally far beyond wave breaking limit. However, the improved hydrodynamic, with the surface piercing correction introduced, can potentially provides a better approximation for wave loads at a steep wave.

Chapter 3

Second Order Irregular Waves

This chapter focuses on second order irregular wave model that encloses both non-linearity and stochasticity in incident waves.

Wave non-linearity exerts a greater effect on structures sited at shallow waters, since the limited water depth deformed the wave profile to be sharp crested and trough flattened [23]. To better capture non-linearity in waves, a finite water depth second order irregular wave model will be first explained in this chapter. Deep water water non-linear wave model, which is the actual intention, will be referred and modeled at a later phase when dealing with floating wind support structure.

3.1 Stochasticity

Irregularity is a fundamental property of ocean waves. As a first approximation, random sea waves may be considered as a liner superposition of an infinite number of sinusoidal waves, characterized by different wave numbers, k_n, amplitudes, A_n, and phase angles, ϕ_n. A random sea state can conveniently be expressed in a mathematical way as a sum of a group of sinusoidal waves,

$$\begin{aligned}\zeta\left(t\right) &= \sum_{n=1}^{N}\left(a_n\cos\left(\omega_n t\right)+b_n\sin\left(\omega_n t\right)\right) && (3.1)\\ &= \sum_{n=1}^{N}A_n\cos\left(\omega_n t+\phi_n\right) && (3.2)\end{aligned}$$

in which $A_n=\sqrt{a_n^2+b_n^2}$, $\phi_n=\arctan\left(\frac{b_n}{a_n}\right)$, $\omega_n=2\pi n\Delta f$, Δf represents the bandwidth, i.e. frequency resolution applied in each sea state realization.

Widely accepted in offshore engineering practice, the energy characteristics of a random sea state is represented by the wave spectral density function $E\left(f\right)$, which indicates the

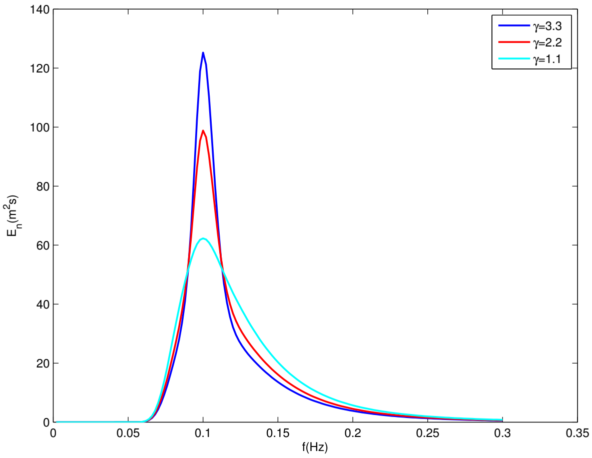

Figure 3.1: *Realization of Jonswasp spectrum*

magnitude of the time average of wave energy as a function of wave frequency. Among the proposed forms, Pierson-Moskowits frequency spectrum, JONSWAP frequency spectrum and TMA frequency spectrum are the most popular ones.

Considering that the Hywind Demo was installed in North sea, a JONSWAP frequency spectrum, which is based on a Joint North Sea Wave Project, can be implemented for wave realization at the site. Proposed by Hasselmann et al. [24], the spectrum has the formulation,

$$E(f) = \left(\frac{m_0}{\Xi}\right) af^{-5}\exp\left(-bf^{-4}\right)\gamma^{\Omega(f)} \tag{3.3}$$

$$\Xi = \sum_{n=1}^{N} af^{-5}\exp\left(-bf^{-4}\right)\gamma^{\Omega(f)}\Delta f \tag{3.4}$$

$$\Omega(f) = \exp\left(-\frac{1}{2}\left(\frac{f-f_p}{\sigma f_p}\right)^2\right) \tag{3.5}$$

in which

$$f = n\Delta f, \quad a = 5f_p^4, \quad b = \frac{5}{4}f_p^4$$

$$\sigma = \sigma_b, \quad for \quad f > f_p$$
$$\sigma = \sigma_a, \quad for \quad f \leq f_p$$

Typical values are $\gamma = 3.3$, $\sigma_a = 0.07$, $\sigma_b = 0.09$, but they are site dependent.

Figure 3.1 shows several realizations of equations above, with $f_p = 0.10Hz$, $\sigma_a = 0.07$, $\sigma_b = 0.09$, but different *gamma*. The wave spectrum tends to have a higher peak at a larger γ and the energy is more concentrated around peak frequency, while at a smaller γ the wave energy is spread over a larger range of frequency around wave peak frequency.

One of the shortcomings of JONSWAP, also for the other two spectrum introduced above, is that the randomness of a real sea state introduced by the wave propagation direction is lost. To account for wave direction, one remedy is to multiply the unidirectional wave spectrum by an empirically determined directional distribution function.

However, the primary objective of the project lies on comparing linear wave model and second order wave model in a random sea state. It can be justified to leave out the wave propagation direction parameter for this moment and focus on static and dynamic characteristics resulting from uni-directional waves. From now on, incident wave will be assumed to be unidirectional, and characterized by $\sigma_a = 0.07$, $\sigma_b = 0.09$, $\gamma = 3.3$,

3.2 Wave model

Based on second order wave model derived by Sharma and Dean [25], the non-linear wave elevation $\zeta^{(2)}$ can be expressed as a sum of first order solution and second order correction terms,

$$\zeta^{(2)}(t) = \zeta^{(1)}(t) + \zeta^{(2+)}(t) + \zeta^{(2-)}(t) \tag{3.6}$$

The first order contribution, $\zeta^{(1)}$ is a sum of various linear waves that cover a complete wave spectrum. Each component, achieved by solving linearized boundary conditions, can be expressed in a sinusoidal form. The first order part is,

$$\zeta^{(1)} = \sum_{n=1}^{N} A_n \cos(\omega_n t - \phi_n) \tag{3.7}$$

where A_n, ω_n and ϕ_n are the wave amplitude, wave frequency and wave phase, with $A_n = \sqrt{2E(n\Delta f)}$, $\omega_n = 2\pi n \Delta f$, Δf is the sampling frequency, n identifies it to be the n^{th} order wave component of the wave series. ϕ_n randomly distributes among $[0, 2\pi)$, and can be realized in *Matlab* by utilizing the command *random.*

Second order correction terms, which include sub-harmonics and super-harmonics, are obtained from second order potential corrections,

$$\zeta^{(2+)} = \sum_{m=1}^{N}\sum_{n=1}^{N} A_m A_n B_{mn}^{+} \cos(\psi_m + \psi_n) \tag{3.8}$$

$$\zeta^{(2-)} = \sum_{m=1}^{N}\sum_{n=1}^{N} A_m A_n B_{mn}^{-} \cos(\psi_m - \psi_n) \tag{3.9}$$

where

$$\begin{aligned} \psi_m + \psi_n &= (\omega_m + \omega_n)t + \phi_m + \phi_n && (3.10)\\ \psi_m - \psi_n &= (\omega_m - \omega_n)t + \phi_m - \phi_n && (3.11) \end{aligned}$$

B^+_{mn} and B^-_{mn} can be seen as transfer function for the solutions of Laplace equations, with non-linear boundary conditions implemented. The transfers functions are given as,

$$B^+_{mn} = \frac{1}{4}\left[\frac{D^+_{mn} - (k_m k_n - R_m Rn)}{\sqrt{R_m R_n}} + (R_m + R_n)\right] \tag{3.12}$$

$$B^-_{mn} = \frac{1}{4}\left[\frac{D^-_{mn} - (k_m k_n + R_m R_n)}{\sqrt{R_m R_n}} (R_m + R_n)\right] \tag{3.13}$$

in which

$$\begin{aligned} D^+_{mn} &= \frac{\left(\sqrt{R_m} + \sqrt{R_n}\right)\left[\sqrt{R_n}\left(k_m^2 - R_m^2\right) + \sqrt{R_m}\left(k_n^2 - R_n^2\right)\right]}{\left(\sqrt{R_m} + \sqrt{R_n}\right)^2 - k^+_{mn}\tanh\left(k^+_{mn}h\right)} \\ &\quad + \frac{2\left(\sqrt{R_m} + \sqrt{R_n}\right)^2\left(k_m k_n - R_m R_n\right)}{\left(\sqrt{R_m} + \sqrt{R_n}\right)^2 - k^+_{mn}\tanh\left(k^+_{mn}h\right)} \end{aligned} \tag{3.14}$$

$$\begin{aligned} D^-_{mn} &= \frac{\left(\sqrt{R_m} - \sqrt{R_n}\right)\left[\sqrt{R_n}\left(k_m^2 - R_m^2\right) - \sqrt{R_m}\left(k_n^2 - R_n^2\right)\right]}{\left(\sqrt{R_m} - \sqrt{R_n}\right)^2 - k^-_{mn}\tanh\left(k^-_{mn}h\right)} \\ &\quad + \frac{2\left(\sqrt{R_m} - \sqrt{R_n}\right)^2\left(k_m k_n + R_m R_n\right)}{\left(\sqrt{R_m} - \sqrt{R_n}\right)^2 - k^+_{mn}\tanh\left(k^-_{mn}h\right)} \end{aligned} \tag{3.15}$$

where k_m is the wave number corresponds to the m^{th} wave component in the wave group, and linked to wave frequency and site water depth via the shallow water dispersion relation, i.e.

$$\omega_m^2 = g k_m \tanh(kh)$$

the other parameters in $B^{\pm}$are defined as ,

$$R_m = \frac{\omega_m^2}{g} \tag{3.16}$$

$$k^-_{mn} = \mid k_m - k_n \mid \tag{3.17}$$

$$k^+_{mn} = \mid k_m + k_n \mid \tag{3.18}$$

3.3 Wave generation

Various techniques have been devised to create the random time histories. Based on methods introduced by H.T. Cuong Cuong et al. [26], inverse fast Fourier transform (IFFT) method gives the desired time history, without further elaboration here, refer to Morooka et al. [27]. In comparison, IFFT method significantly reduces the computation time. To generate a $1000s$ wave records with a time increment of $0.3s$, IFFT methods consumes $8.1 \times 10^{-4}s$ only, while the superposition method needs as much as $1.3s$. This advantage will be more evident when wave frequency spectrum is subdivided into more subtle components.

However, the problem of using IFFT is also quite obvious: the time increment in the generated wave is constrained by cut-off frequency of the wave spectrum. In Stansberg et al. [28], it is stated that a spectrum input with a long tail will include a higher level of non-linearity than a narrow spectrum with the same energy. To avoid introducing nonphysically reasonable high frequency terms, the wave spectrum used in second order irregular wave modeling generally does not include components higher than cut-off frequency. Since the cut-off frequency is recommend to be four times peak frequency, see Forristall [29], time increment implemented used in simulation is thus $1/cf = 2.5s$ for a wave condition characterized by $T_p = 10s$. Though linear interpolation can be applied to get the wave information between two consecutive points in wave record, the large time step still causes problem for time domain integration when it comes to dynamic response analysis.

As a remedy, a modified JONSWAP spectrum, which follows the JONSWAP below the cut off frequency and artificially extend to a higher value with zero energy concentration will be introduced in analysis.

Although wave generation efficiency is improved by IFFT, second order irregular wave formulation is still time consuming. When the wave spectrum is divided into N components, the integration should be repeated N^2 times, if direct integration method is applied. Fortunately, by collecting terms with the same frequency first, it is possible to reduce the calculation times to $2N-1$ for sum frequency contribution, and $N-1$ for low frequency terms. Though the saved time will be offset to some extent by the operation of locating and collecting the same-frequency terms in the $N \times N$ matrix, the reduced computation time with regards to total computation time is still very promising.

The formulation of sum and difference frequency terms follow equation 3.18. Figure 3.2 further illustrates the method. In the figure $\omega_1 = \Delta f,\ \omega_2 = 2\Delta f, \cdots, \omega_n = n\Delta f$. If the same frequency terms, (i.e. the diagonal going from the lower left corner to the upper right corner in sum-freq matrix, and the diagonal going from upper left corner to the lower right corner in dif-freq matrix), are collected first, the double summation of $N \times N$ terms can be replaced with a single summation of $2N-1$ terms for sum frequency components, and $N-1$ for difference frequency components.

In this way, equation Equations 3.18, which composes of double summations, will be simplified as,

$$\zeta^{2+} = \sum_{p=1}^{2N-1} A_p^+ B_p^+ \cos\left(\omega_p^+ t + \phi_p^+\right) \tag{3.19}$$

$$\zeta^{2-} = 2 \cdot \sum_{p=1}^{N-1} A_p^- B_p^- \cos\left(\omega_p^- t + \phi_p^-\right) \tag{3.20}$$

where,

	ω_1	ω_2	ω_3	ω_4	...	ω_n
ω_1	$2\Delta f$	$3\Delta f$	$4\Delta f$	$5\Delta f$		
ω_2	$3\Delta f$	$4\Delta f$	$5\Delta f$			
ω_3	$4\Delta f$	$5\Delta f$				
ω_4	$5\Delta f$					
⋮						
ω_n						$2n\,\Delta f$

	ω_1	ω_2	ω_3	ω_4	...	ω_n
ω_1		$1\Delta f$	$2\Delta f$	$3\Delta f$		
ω_2	$-1\Delta f$		$1\Delta f$	$2\Delta f$		
ω_3	$-2\Delta f$	$-1\Delta f$		$1\Delta f$		
ω_4	$-3\Delta f$	$-2\Delta f$	$-1\Delta f$			
⋮						
ω_n						

Figure 3.2: *Second order wave frequency matrix, left sum-freq, right dif-freq*

$$
\begin{aligned}
A_p^{\pm} &= \sum_{m \pm n = p} A_{mn} \\
B_p^{\pm} &= \sum_{m \pm n = p} B_{mn} \\
\omega_p^{\pm} &= \sum_{m \pm n = p} \omega_{mn} \\
\phi_p^{\pm} &= \sum_{m \pm n = p} \phi_{mn}
\end{aligned}
$$

the method shows in figure 3.2 is also applicable to generate second order transfer function and second order wave height. With an integration order reduction method introduced, it is expected to generate numerical second order irregular wave in a more efficient manner.

3.3.1 Regular wave

To get a knowledge of how wave elevation is affected by including sub and super-harmonic terms, a Dirac-delta function is used to express the wave spectrum and formulate a wave series composed of only a single frequency sinusoidal wave. See from figure 3.3, the difference frequency component is absent from the numerical wave, since there is only one frequency component in the wave series. The sum-frequency component, which is also sinusoidal, is characterized by showing a frequency twice of first order input. Also, since sum frequency component are in phase at peaks and out of phase at troughs, the total sum of second order solution, exhibits an elevation effect, characterized by a higher peak and a flattened trough.

The non-linearity of a sea state can measured by both wave amplitude and wave period. Wave steepness kA, which is linked to both wave amplitude and wave period, is normally

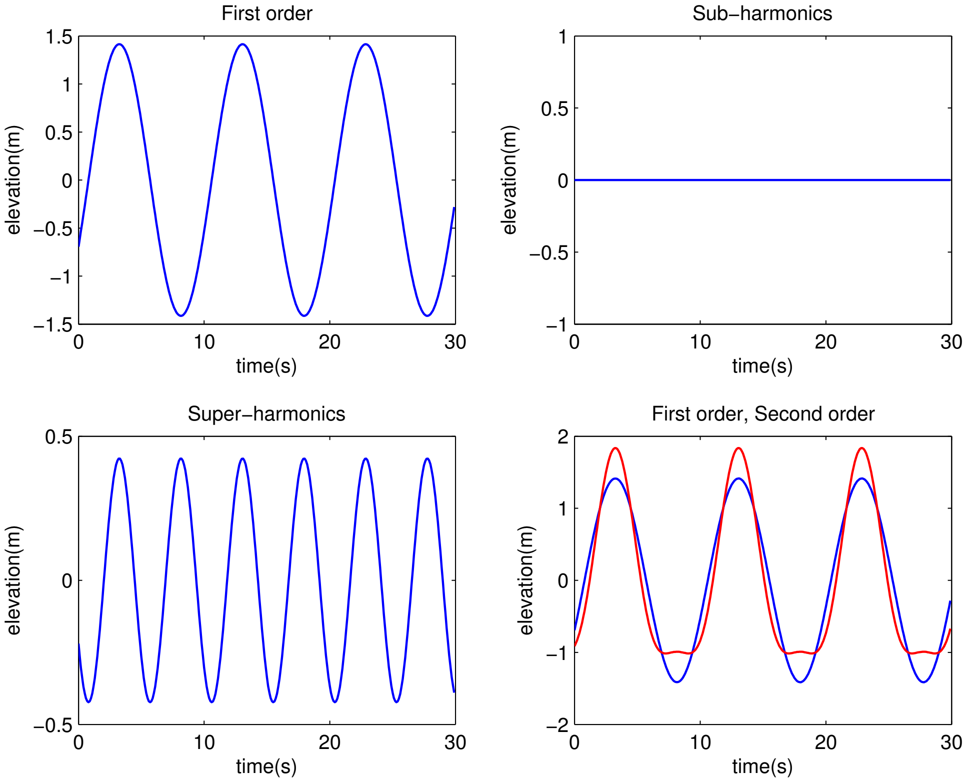

Figure 3.3: *Second order regular wave*

Table 3.1: *Summary of data sets used in simulation*

	$T[s]$	$H[m]$	kA	comment
1	8.33	4.24	0.13	mild
2	8.33	5.65	0.17	medium
3	6.66	4.24	0.19	medium
4	6.66	5.65	0.26	extreme

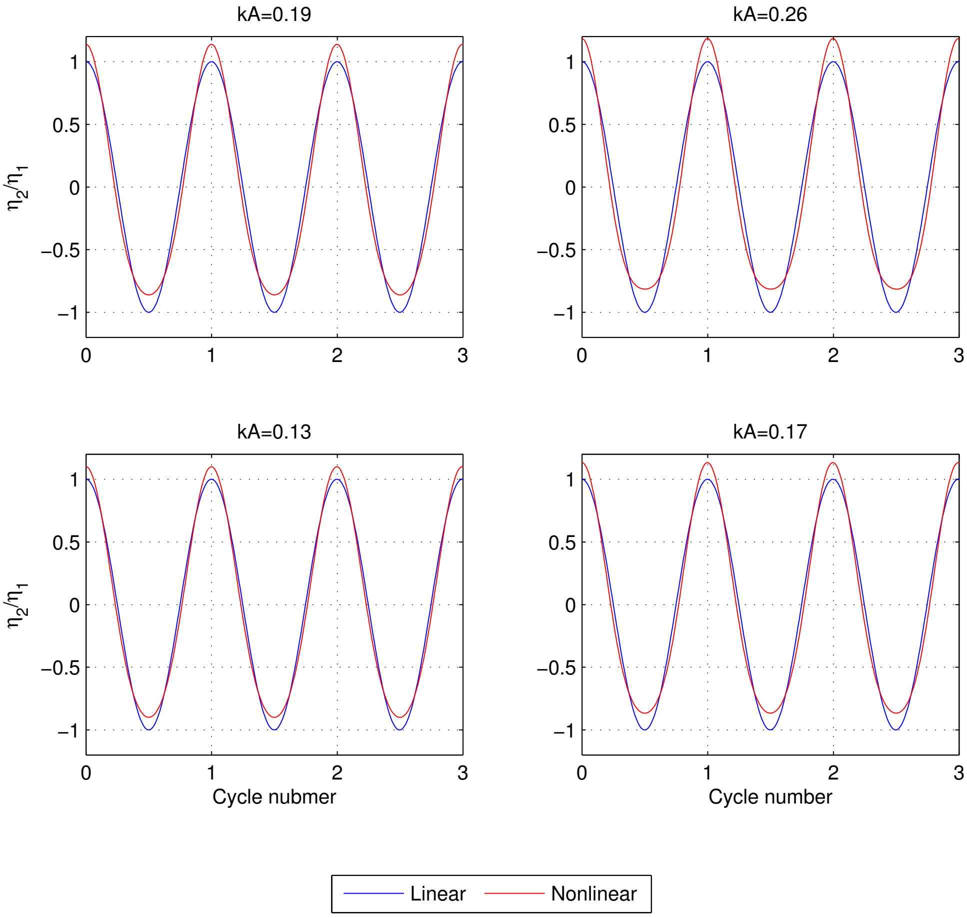

Figure 3.4: *Second Order Regular Wave, 4 sea states comparison*

employed to describe the non-linearity of a wave input. To study the influence of these two parameters on non-linearity of numerical wave, four groups of kA, listed in table 3.1, are generated for simulation purposes. Characterized by wave steepness kA, these four data sets are intended to simulate a mild, two medium, and a extreme wave states respectively. Figure 3.4 shows how the modified wave model affects the wave surface elevation at different wave steepness. The figure contains only the first three cycles, and wave elevation is normalized to first order amplitude. As expected, the difference between first order and second order solution is smallest at a benign sea sate (lower left) among the four input sets, while it deforms wave profile to severely at the worst case (upper right).

Table 3.2 summarizes the wave statistics, including maximum elevation, variance and skewness. The trend shown in the table is consistent with what is observed in figure 3.4. The larger the wave steepness, the more noticeable the change in wave height. Skewness, which is an indicator of non-linearity, turns non-zero for non-linear incident wave trains. The largest skewness is achieved at highest wave steepness, and lowest value corresponds to the wave input with lowest wave steepness.

Table 3.2: *Summary of regular wave statistics, water depth 30m*

	Maximum$[m]$		Variance$[m^2]$		Skewness	
Wave Steepness	Linear	Non-linear	Linear	Non-linear	Linear	Non-linear
0.13	2.12	2.33	2.26	2.27	0.00	0.21
0.17	2.83	3.21	4.01	4.07	0.00	0.28
0.19	2.12	2.42	2.25	2.29	0.00	0.29
0.26	2.83	3.35	4.01	4.14	0.00	0.38

Table 3.3: *Biachromatic wave parameters*

		Wave Group 1		Wave Group 2	
		Comp. 1	Comp. 2	Comp. 1	Comp. 2
Wave period	[s]	4.00	10.00	8.00	10.00
Wave height	[m]	4.24	4.26	4.24	4.24

3.3.2 Bichromatic wave

Difference frequency components will be present in waves that compose of at least two frequency components, i.e. a bichromatic wave. Figure 3.5 shows time series of two bichromatic wave groups, see table 3.3 for wave parameters. Each wave group contains two frequency components, and zeros phase angle is assumed for sinusoidal wave input in both groups. In figure 3.5, the upper two figures illustrates the time series of wave elevation, while the lower two are the results of FFT, showing the power spectrum of the two generated waves. At a first glance, it is noticed that the time series differs mainly in wave peak and wave trough.

Group 1 shows a higher level of non-linearity, characterized by an obvious deviation from first order solution at both wave peak and wave trough, while in group 2 the difference is relatively less obvious. Besides, while there is only an elevation effect observed in the wave profile of group two, the wave troughs in group one are severely deformed due to second order effects. Also, since the two wave inputs are quite close in wave period in group 2, it results only in three noticeable wave frequency components in power density spectrum, together with other three components with negligible energy accumulation. There are in total six easily distinguished peaks in the lower left figure, with additional three sum-frequency components and one difference frequency component.

3.3.3 Irregular wave

Second order irregular wave theory allows it to include the stochastic nature of a real sea state, though it is still time consuming. One aspect of interests is to see how it affects wave surface elevation, with regards to max wave elevation, variance, skewness and kurtois.

A three hour time series of waves is generated using a JONSWAP spectrum, parametrized by $H_s = 5.0\ m$ and $T_p = 12\ s$. Two shallow water sites, with a water depth of $h = 20\ m$ and 30 m, respectively will be the target site for wave realization. Since the sea state is considered extreme for that water depth, non-linearity should be expected to be evident

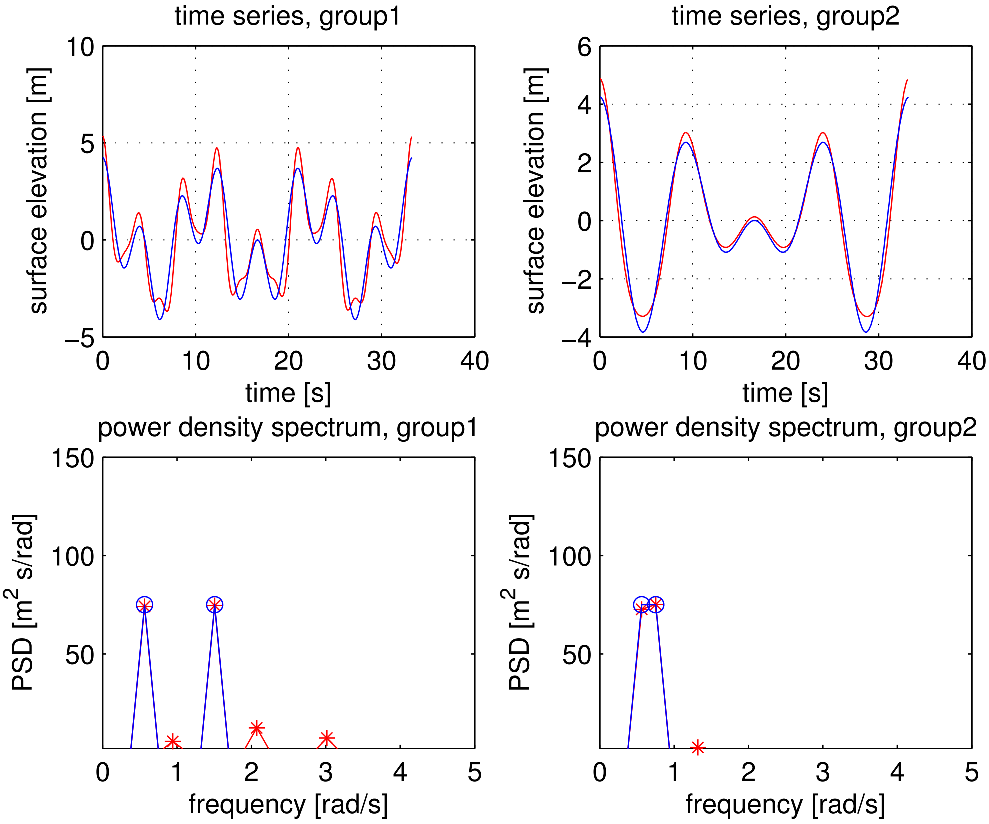

Figure 3.5: *Time series of bichromatic wave, red: second order, blue: first order*

in the simulation results. A total of one hundred seeds are used to minimize short term variance introduced by the randomly generated phase angle ϕ.

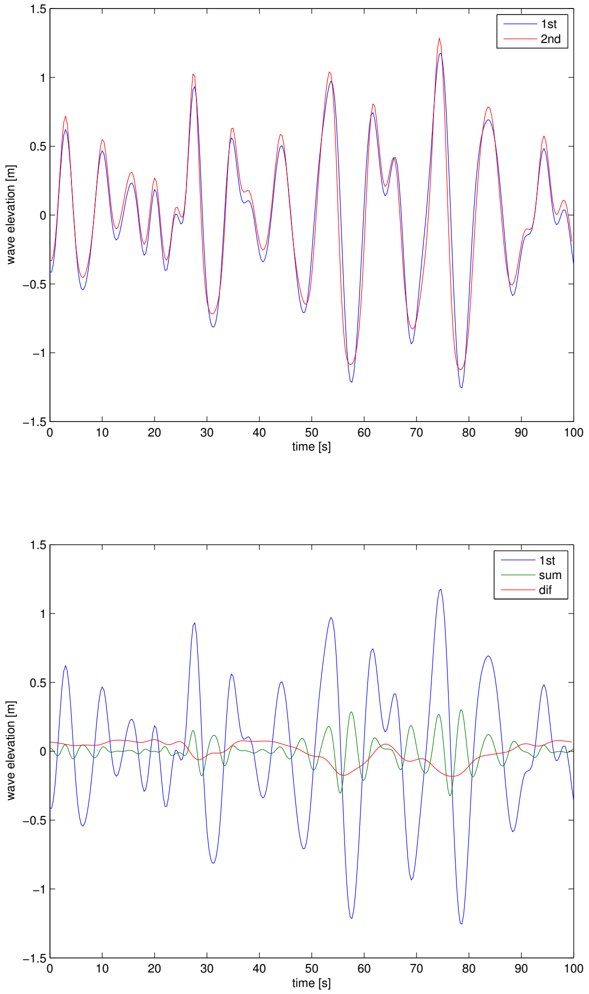

Figure 3.6: *Second order irregular wave time series*

Figure 3.6 is a realization of a stochastic sea state implemented with both linear and non-linear wave model. Clearly, when the non-linear components are included, the wave train tends to have a higher peak at crest and flatter trough at wave bottom. Due to the change of wave shape, especially the higher peaks, it can be expected to induce a higher load at the wave-structure intersection. The second figure in 3.6, which decomposes the second order profile into first order components and second order corrections, can work to explain the mechanism. Similar to the first order simulation, the sum component sharpens to the peak and flatten the trough, due to the difference in phase angle. Concluded by Carl Stansberg et al. [30], second-order elevation produces reasonably well the sharpening of the crest and flattening effects at troughs, compared with measurement data.

Figure 3.7 transforms the time domain wave elevation records into frequency domain. Both the spectrum for linear and non-linear wave surface elevation reach the peak at

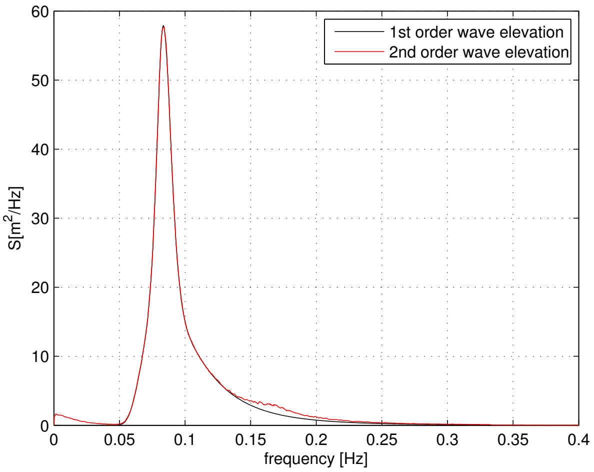

Figure 3.7: *Wave elevation spectrum,* $H_s = 5\ m,\ T_p = 12\ s,\ ,\gamma = 3.3,\ h = 20\ m$

Table 3.4: *Code Validation,* $H_s = 12\ m, T_p = 14\ s, h = 30\ m$

	Variance $[m^2]$	Skewness	Kurtiosis
Target	9.22	0.17	3.10
Simulation	9.17	0.17	3.04

incident wave peak frequency, corresponds to $T_p = 12\ s$. While the first order solution poses the shape of JONSWAP spectrum, second order solution deviates from first order curve around $f = 0\ Hz$ and $f = 0.17\ Hz$, by displaying two additional peaks. The first sub-peak can be owed to difference interactions of first order components, and the second sub-peak is attributed to the super harmonics enclosed in the second order corrections. Tough second order irregular wave model brings in a higher level of energy and results in an odd shape that contradicts with wave power spectrum input, it actually does not need to be corrected and is said to be a better approximation of measured elevation, see Veldkamp and Van Der Tempel [31].

To validate Matlab code, a study is carried out to compare the statistical properties of the wave generated with values in literature. A JONSWAP spectrum with a significant wave height of 12 m and peak period of 14 s is used to simulate a 3 hour wave series and compare it with value reported by Sweetman and Winterstein [32]. Table 3.4 shows the mean value over 500 realizations. The simulation results are fairly close to the target value, which proves the Matlab code to be valid.

To investigate the non-linearity introduced by second order correction, a statistics comparison is carried out focusing on skewness and kurtois of the generated wave train. Skewness is an indicator for symmetry of the probability density function. For a linear wave, which is a true Gaussian process, the calculated value should be zero. However, when non-linearity is introduced, the skewness will be different from zero. Kurtosis represents the tails for the probability density function. For a Gaussian process, such as the linear wave trains, the value is 3, while for a non-linear is larger than 3.

See from table 3.5, linear model generates a wave series that corresponds to a Gaussian

Table 3.5: *Statistics for sea surface elevation*

	Max $[m]$	Min$[m]$	Variance$\left[m^2\right]$	Skewness	Kurtiosis
$h = 20m$					
Linear	4.81	-4.78	1.56	0.00	2.99
Non-linear	5.45	-4.78	1.66	0.10	3.07
Ratio	1.13	1.00	1.06		1.02
$h = 30m$					
Linear	4.88	-4.87	1.56	0.00	3.00
Non-linear	5.38	-4.87	1.60	0.11	3.03
Ratio	1.10	1.00	1.02		1.01

process. Skewness remains zeros, since it is symmetrical. The no-linear wave model increases peak crest by around 10%, which is consistent with the elevation effect observed in regular waves. The non-linearity of the wave is also indicated by the change in skewness, which is no longer a non-zero value. Also, the kurtois becomes larger than 3 and makes it a non-Gaussian process. When a distribution kurtosis is greater than 3, it is said to be leptokurtic, associated with distribution contains a fat tail.

The level of non-linearity is also dependent on site conditions. The change in wave elevation, and skewness tend to be affected to a greater extent at a shallower water site and at a sea sate characterized with higher significant wave heights and shorter peak period, e.g. when the wave period decrease to $7s$, the wave crest increase reaches 20%, and skewness to 0.27.

3.4 Wave kinematics

The accuracy of loads estimation, especially wave zone load in an extreme sea state, largely relies on the proximity of wave kinematics model used. In linear wave models, velocities are valid up to mean sea level due to boundary condition linearization. The linearization simplification can be justified for estimating wave loads at a benign sea state, but for a severe sea state with high wave steepness, it fails to capture the kinematics in wave zone and consequently underestimate loads in the wave zone. By implementing second order wave corrections, wave kinematics in the crest can be added as a correction term to the first order solution.

The wave kinematics estimation is based on a 2nd order perturbation. Obtained velocity potential will be valid up to the free surface, i.e,

$$\Phi^2(z) = \Phi^1(z) + \Phi^{2+}(z) + \Phi^{2-}(z) \quad for \quad z \leq 0 \tag{3.21}$$

$$\Phi^2(z) = \Phi^1(0) + \Phi^{2+}(0) + \Phi^{2-}(0) + z \cdot \frac{\partial \Phi^1}{\partial z}\,|_{z=0} \quad for \quad z > 0 \tag{3.22}$$

in which Φ^1, Φ^2,Φ^{2+}, and Φ^{2-} are first order potential, second order potential, second order sum frequency correction potential and second order difference frequency correction potential, respectively. The third term in equation 3.22 can be treated as as a Taylor expansion of first order potential at $z = 0$, and thus the solved potential problem will be valid up to linear surface elevation, ζ^1. While the first order potential can be found from classical linear wave theory, the second order correction terms can be formulated with a quadratic transformation function as presented by Sweetman and Winterstein [32].

Partial velocity and local acceleration are the first order derivative of the potential to space and time. The correction method includes super-harmonics and sub-harmonics terms for particles below water level and at the same time linearly extrapolate the linear velocity at $z = 0$ to the crest. The horizontal velocity at a level z is formulated as,

$$u^{(2)}(z) = u^{(1)}(z) + u^{(2+)}(z) + u^{(2-)}(z) \quad for \quad z \leq 0 \tag{3.23}$$

$$u^{(2)}(z) = u^{(1)}(0) + \frac{\partial u^{(1)}}{\partial z}|_{z=0} \cdot z + u^{(2+)}(0) + u^{(2-)}(0) \quad for \quad z > 0 \tag{3.24}$$

in which u^2, u^1, u^{2+}, u^{2-} are x component of the corrected second order particle velocity, first order particle velocity and contributions from sum, difference frequency potentials respectively. The solution, based on second order perturbation of the velocity potential, is valid up to first order free surface.

To compare wave kinematics profile, three models, first order solution to mean free surface, first order solution with Wheeler stretching implemented and second order solution, are chosen to establish particle velocity profile in wave zone for a site $h = 30\ m$.

Figure 3.8 shows the wave kinematics calculated with the above mentioned three wave kinematic calculation methods for waves listed in table 3.1. In the figure, horizontal axis shows the normalized velocity, ratio between local velocity to first order solution at wave crest. Vertical coordinates are the vertical location. See from the figure, Wheeler's method under predict velocities in steep waves for $z < 0$, though it managers to express wave kinematics in the wave zone $z > 0$. Second order solution linearly extends the profile to the wave free surface, and the predicted velocity is about $1.2u_1 - 1.4u_1$. The increment ratio is dependent on wave steepness. At a higher wave steepness, i.e in the upper right figure, the ratio reaches 1.4, while at $kA = 0.13$, the ratio is about 1.2. When $z < 0$, the second order solution overlaps with first order solution, though minor difference can still be observed.

However, the difference between second order and first order wave kinematics is present in a bichromatic wave group for $z < 0$. When difference frequency components are added to the wave train, it works to elevate the velocity profile and slightly decreases wave kinematics under the wave crest. In general, non-linear model slightly under predict the wave kinematics under mean water level, but significantly increases that at wave crest, to 1.5 u_1 for some cases. Wheeler's methods stretches the profile to the wave surface, but consequently reduce the wave loads under the mean free surface. Due to presence of second order difference frequency contributions, the second order potential contribution puts a negative effect on wave kinematics, which is interpreted as a 'return current' by Longuet-Higgins and Stewart [33]. The trend shows in figure 3.10 is consistent with the

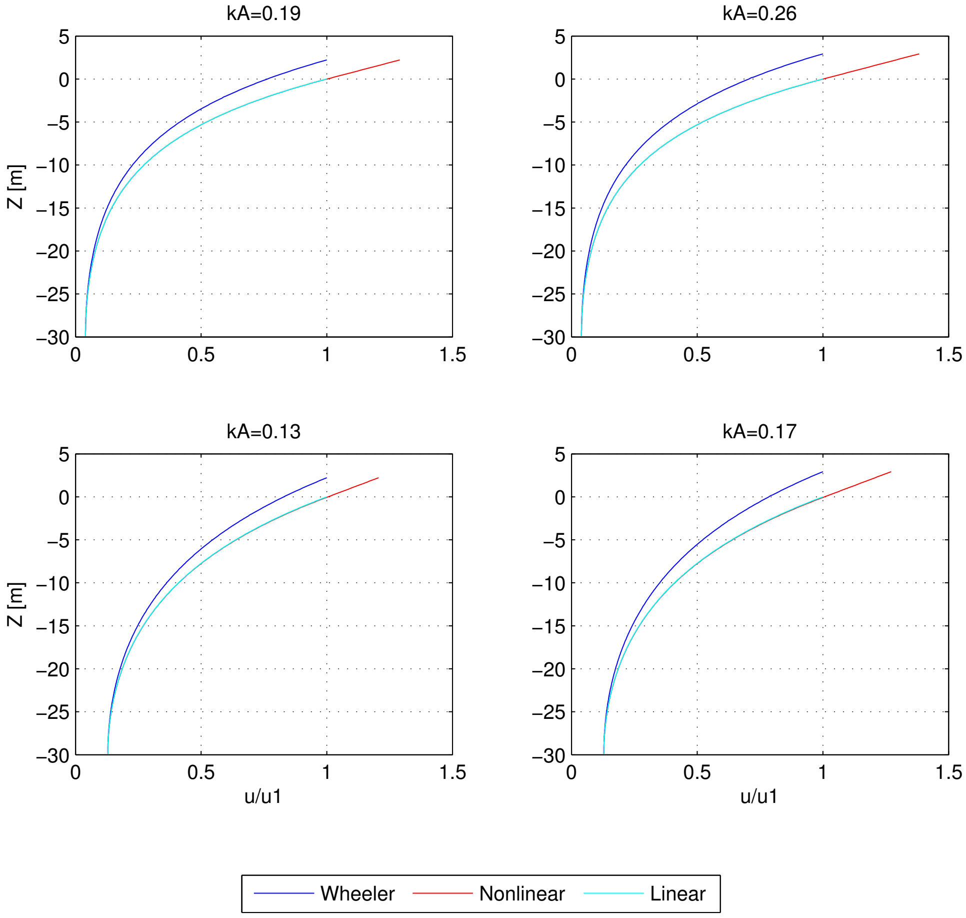

Figure 3.8: *Wave Kinematics, regular wave, t=0s, h=30 m*

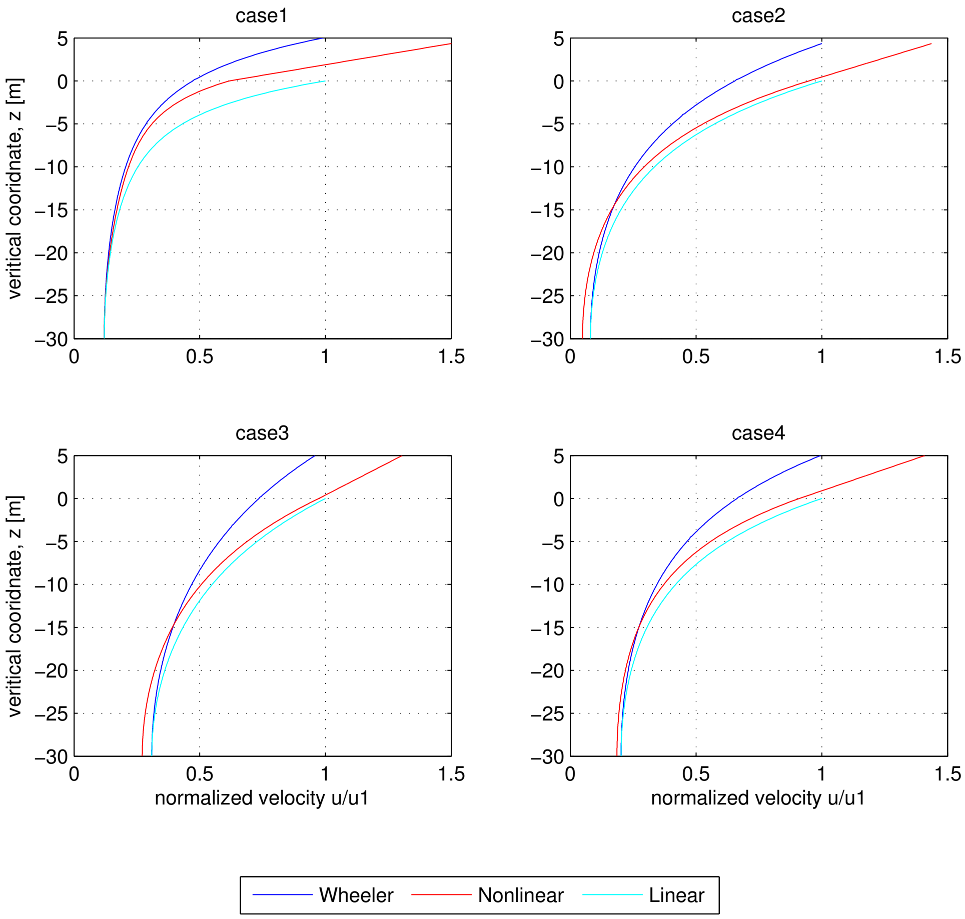

Figure 3.9: *Wave Kinematics, bichromatic, t=0s, h=30 m*

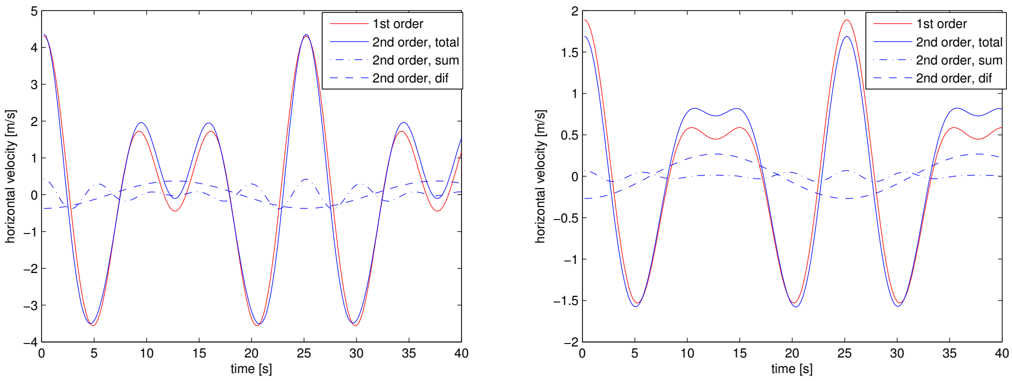

(a) $z = 0\ m$

(b) $z = -20\ m$

Figure 3.10: *Horizontal particle velocity, bichromatic waves,* $h = 30\ m,\ T_1 = 8\ s,\ T_2 = 12\ s, A_1 = 2\ m, A_2 = 2\ m$

'return current' phenomenon. While the super-harmonics add to wave kinematics, second order difference component tends to reduce local maximum of horizontal particle velocity, and the effect is more evident at $z < 0$ due to the slower vanishing tendency than higher frequency terms.

3.5 Force

With wave kinematics expressed in the same way as the previous section, the proposed wave model can be conveniently implemented into the modified non-linear loads model, with first order wave theory kinematics replaced by second order expressions. To get an impression of how the loads acting on a cylinder will be influenced by including higher order terms, a fixed cylinder at a shallow water site, e.g. a monopile, is chosen as the loading structure to analyze load statistics.

3.5.1 Implementation in Rainey's model

Rainey's equation, which originally derived for a slender structure, can be expressed in an analytically way, with the following taken into considerations,

1. Cylinder assumed to be rigidly fixed with negligible deformation, and relative velocity equals water particle velocity,
2. Strip theory assumed valid, which indicates that it is a 2D problem without any terms in y direction.

$$dF_x = \left(\rho\frac{\pi D^2}{4} + m_x\right)\left(\frac{\partial u^{(2)}}{\partial t} + u^{(2)}\frac{\partial u^{(2)}}{\partial x} + w^{(2)}\frac{\partial u^{(2)}}{\partial z}\right) + m_x\frac{\partial w^{(2)}}{z}u^{(2)}[22] \tag{3.25}$$

where $u^{(2)}$ follows the expression in 3.24 and 3.23 and $w^{(2)}$ has a similar form, but u replaced by w. The other terms are derived as below,

for a second order irregular wave, which is expressed as

$$\zeta^{(2)} = \sum_{n=1}^{N} A_n \cos(\psi_n) + \sum_{m=1}^{N}\sum_{n=1}^{N} A_m A_n B_{mn}^{+} \cos(\psi_m + \psi_n) + \sum_{m=1}^{N}\sum_{n=1}^{N} A_m A_n B_{mn}^{-} \cos(\psi_m - \psi_n) \tag{3.26}$$

the first order kinematics has the following forms, for x components,

$$u_n^{(1)} = \omega_n A_n \frac{\cosh(k_n(z+h))}{\sinh(kh)} \cos(\psi_n) \tag{3.27}$$

while in z direction,

$$w_n^{(1)} = \omega_n A_n \frac{\sinh\left(k_n\left(z+h\right)\right)}{\sinh\left(kh\right)} \sin\left(\psi_n\right) \tag{3.28}$$

the derivatives to t, x, and z are,

$$\begin{aligned}
\frac{\partial u^{(1)}}{\partial t} &= -\sum_{n=1}^{N} \omega_n^2 A_n \frac{\cosh\left(k_n\left(z+h\right)\right)}{\sinh\left(kh\right)} \sin\left(\psi_n\right) && (3.29)\\
\frac{\partial u^{(1)}}{\partial x} &= \sum_{n=1}^{N} k_n \omega_n A_n \frac{\cosh\left(k_n\left(z+h\right)\right)}{\sinh\left(kh\right)} \sin\left(\psi_n\right) && (3.30)\\
\frac{\partial u^{(1)}}{\partial z} &= \sum_{n=1}^{N} k_n \omega_n A_n \frac{\sinh\left(k_n\left(z+h\right)\right)}{\sinh\left(kh\right)} \cos\left(\psi_n\right) && (3.31)
\end{aligned}$$

introducing second order terms to the expression,

$$\begin{aligned}
\frac{\partial u^{(2)}}{\partial t} &= \sum_{n=1}^{N} \frac{\partial u_n^{(1)}}{\partial t} + \sum_{n=1}^{N}\sum_{m=1}^{N} \frac{\partial\left(u_{mn}^{(2+)} + u_{mn}^{(2-)}\right)}{\partial t} \quad for \quad z \leq 0 && (3.32)\\
\frac{\partial u^{(2)}}{\partial t} &= \frac{\partial u^{(2)}}{\partial t} |_{z=0} + \sum_{n=1}^{N} z \cdot \frac{\partial^2 u_n^{(1)}}{\partial t \partial z} |_{z=0} \quad for \quad z > 0 && (3.33)
\end{aligned}$$

$$\begin{aligned}
\frac{\partial u^{(2)}}{\partial z} &= \sum_{n=1}^{N} \frac{\partial u_n^{(1)}}{\partial z} + \sum_{n=1}^{N}\sum_{m=1}^{N} \frac{\partial\left(u_{mn}^{(2+)} + u_{mn}^{(2-)}\right)}{\partial z} \quad for \quad z \leq 0 && (3.34)\\
\frac{\partial u^{(2)}}{\partial z} &= \frac{\partial u^{(2)}}{\partial z} |_{z=0} + \sum_{n=1}^{N} \frac{\partial u_n^{(1)}}{\partial z} |_{z=0} \quad for \quad z > 0 && (3.35)
\end{aligned}$$

$$\begin{aligned}
\frac{\partial w^{(2)}}{\partial z} &= \sum_{n=1}^{N} \frac{\partial w_n^{(1)}}{\partial z} + \sum_{n=1}^{N}\sum_{m=1}^{N} \frac{\partial\left(w_{mn}^{(2+)} + w_{mn}^{(2-)}\right)}{\partial z} \quad for \quad z \leq 0 && (3.36)\\
\frac{\partial w^{(2)}}{\partial z} &= \frac{\partial w^{(2)}}{\partial z} |_{z=0} + \sum_{n=1}^{N} \frac{\partial w_n^{(1)}}{\partial z} |_{z=0} \quad for \quad z > 0 && (3.37)
\end{aligned}$$

$$\begin{aligned}
\frac{\partial u^{(2)}}{\partial x} &= \sum_{n=1}^{N} \frac{\partial u_n^{(1)}}{\partial x} + \sum_{n=1}^{N}\sum_{m=1}^{N} \frac{\partial\left(u_{mn}^{(2+)} + u_{mn}^{(2-)}\right)}{\partial x} \quad for \quad z \leq 0 && (3.38)\\
\frac{\partial u^{(2)}}{\partial x} &= \frac{\partial u^{(2)}}{\partial x} |_{z=0} + \sum_{n=1}^{N} z \cdot \frac{\partial^2 u_n^{(1)}}{\partial x \partial z} |_{z=0} \quad for \quad z > 0 && (3.39)
\end{aligned}$$

Double summation above shall utilize the same reduction method used for wave generation.

3.5.2 Comparison

With both non-linear hydrodynamic model and higher order irregular wave model introduced, a total of 6 methods, summarized in table 3.6, can be utilized to calculate wave forces acting on a slender cylinder structure. The second and third column define the wave model and hydrodynamic model applied in loads calculation, and the fourth column works to assign a name for each model. For reducing calculation time purposes, quasi-static state is assumed, and aerodynamic forces are not included. Considering a bottom fixed wind support structure, the quasi-static loading condition can be justified, since the structure is normally quite stiff and the dynamic behavior is of secondary concern.

Table 3.6: *Load calculation models*

No	Wave Model	Load Model	Comment
1	1st Order	Morison	Linear Morison
2	1st Order	Rainey	Linear Rainey
3	1st+Wheeler	Morison	Wheeler Morison
4	1st+Wheeler	Rainey	Wheeler Rainey
5	2nd Order	Morison	Non-linear Morison
6	2nd Order	Rainey	Non-linear Rainey

Compared with first order wave model, second order irregular wave theory enables a better description of wave peaks, which can potentially better describe loads in wave zone and increase the total hydrodynamic forces exerting on an offshore wind sub-structure. Besides, the non-linear hydrodynamic model includes higher order force components at the wave-structure intersection when solving this surface piercing problem. The additional higher order term at the wave intersection can be critical at a severe sea state where wave height approaches cylinder diameter. If take a bottom fixed monopile, which is laterally supported, as a the offshore wind support structure, shear force and bending moment at the foundation bottom needs to be investigated for design purposes.

Regular Wave

Table 3.7: *Comparison of load statistics of monopile base shear, quasi-static assumed, regular wave, T=8 s, H=3 m*

	Model	1	2	3	4	5	6
Sea State							
1	Max [MN]	1.58	1.67	1.61	1.62	1.73	1.67
	Sta.Dev	1.13	1.15	1.13	1.12	1.23	1.19
	Skewness	0.00	-0.08	0.01	-0.07	0.01	-0.13

To figure out how the various loads calculation model affects the magnitude of loads, a regular wave with a wave period of 8 s and wave amplitude of 1.5 m is used as the incident wave. See from table 3.7, the non-linear models alter the skewness of loads, which is no longer zero. Rainey's model tends to introduce a negative skewness and makes the distribution has a long left tail, while Wheeler's and second order correction achieves a positive skewness and a long left tail. Also, non-linear model includes a higher variation of loads, indicated by an increased standard deviation. One thing worth noticing is that while Wheeler stretching gives higher load than first order solution when Morison equation is used, it actually reduces the total force when combined with Rainey's model, see 2 and 4 in table 3.10.

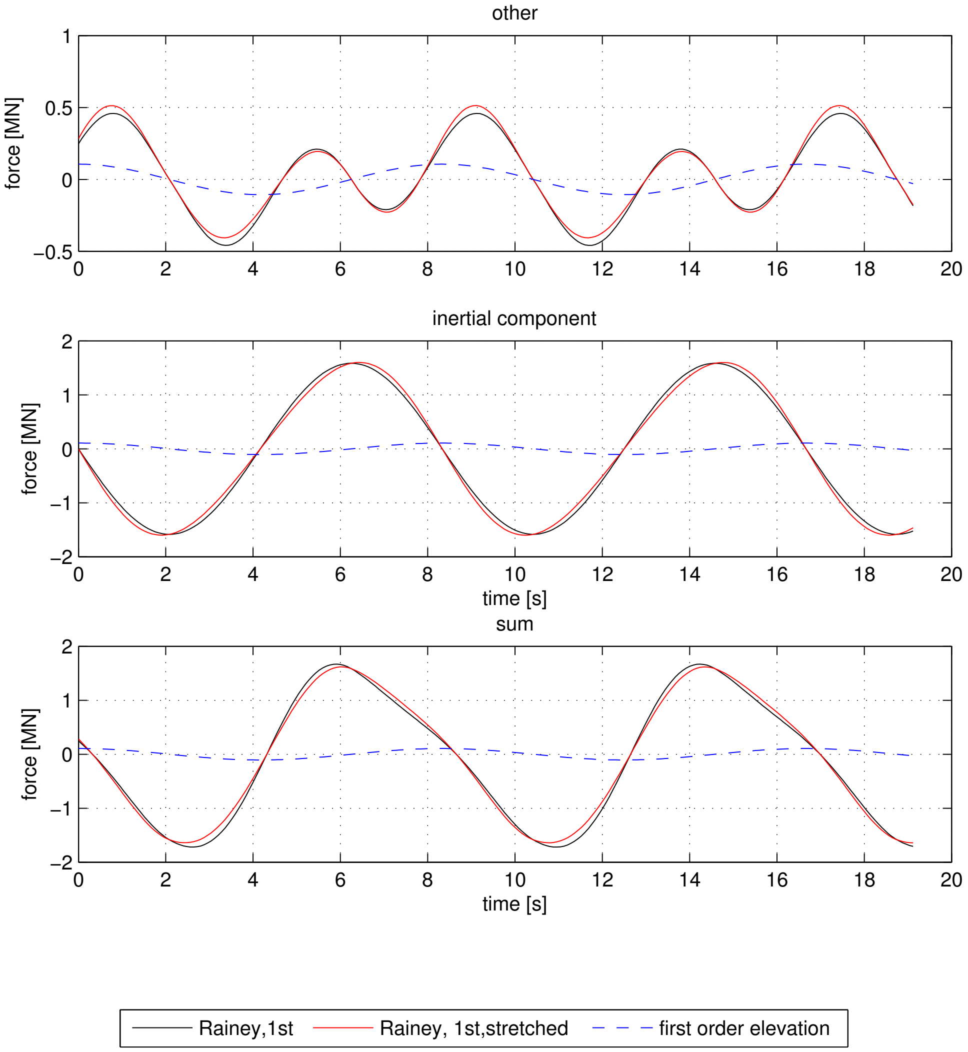

Figure 3.11: Comparison of Rainey's model with linear wave model with stretching

Figure 3.11 and 3.12 explain why Wheeler's stretching reduces the maximum value of wave load. Rainey's model mainly modifies the inertia term in the Morison equation. See from the two figures, inertia components are dominating in the total wave force. Due to the phase difference between inertia term and the rest, the maximum value occur at $z < 0$, below mean water level. The compressed wave profile results in a smaller derivation of velocity terms with respect to z, and consequently reduces the value of the maximum

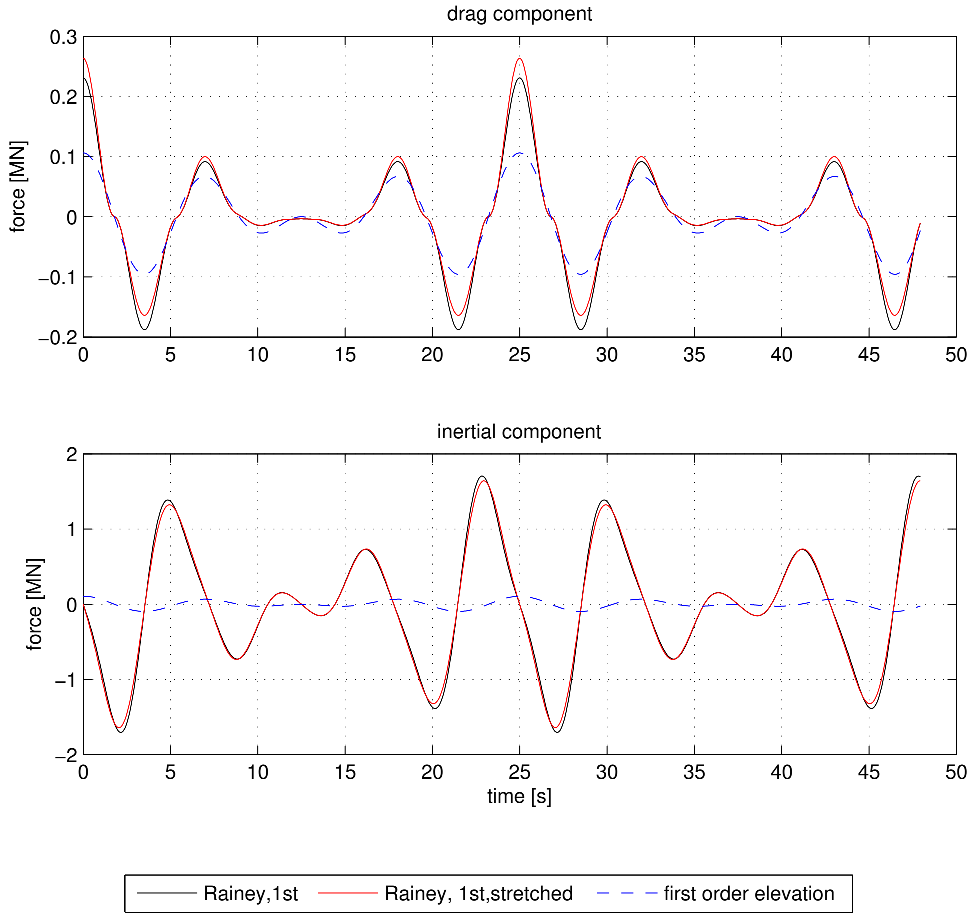

Figure 3.12: *Drag component*

load. Figure 3.12 shows how Wheeler's streching affects the drag term in Rainey's load calculation model. Different from inertia terms, the non-linear model still results in a similar loading curve, but higher peaks and lower troughs.

Irregular Wave

The objective of this part is to compare the maximum shear force and bending moment at foundation base when subject to first order irregular wave and second order irregular wave. Four sea states are chosen in the simulation, based on North Sea conditions described by Faltinsen [34], see table 3.8.

Table 3.8: *Sea states*

Sea state	$T_p[s]$	H_s [m]	Comment
1	8	3.25	Mild
2	9	5.10	Medium
3	10	6.00	Medium
4	10	7.50	Extreme

Each sea state represents a mild, medium or a extreme wave condition for the selected site with a water depth of 20 m. A total of 48 seeds are used in simulation for the realization of each sea state that lasts 30 min. The reason that a 30 min, instead of 3 h simulation is that when using *IFFT* method, the extension in sea state realization time will greatly increase the matrix size and consequently reduces computation efficiency significantly. A simulation of 3 h sea state cost significantly longer time than 6 realization of 30 min the same sea state. To ensure the results are both representative and computationally efficient, a total of 48 seeds are taken, fully utilizing multi-task ability of parallelly running 12 tasks in Matlab. Table 3.9 and 3.10 show the averages of 48 simulations, represented as the ratios to first order value. The absolute are included in Appendix E.

Table 3.9: *Comparison of load statistics of monopile base shear, quasi-static assumed, averages maximum over 50 simulations, ratio to first order value*

	Model	1	2	3	4	5	6
1	Max	1.00	1.08	1.01	1.03	1.02	1.15
	Sta.Dev	1.00	1.01	1.00	1.00	1.01	1.02
2	Max	1.00	1.13	1.02	1.05	1.06	1.27
	Sta.Dev	1.00	1.01	1.00	1.00	1.01	1.04
3	Max	1.00	1.15	1.03	1.05	1.07	1.32
	Sta.Dev	1.00	1.02	1.00	1.00	1.02	1.05
4	Max	1.00	1.13	1.05	1.03	1.12	1.34
	Sta.Dev	1.00	1.02	1.00	1.00	1.03	1.05

Take table 3.9 as an example, non-linear models introduce a higher load at the foundation bases, ranging from 3% to 34%, depending on sea sates and load calculation model. Figure 3.13 summarizes the general trend shows in the table. Linear Rainey and Non-linear

Table 3.10: *Comparison of load statistics of monopile base bending moment, quasi-static assumed, average maximum over 50 simulations, ratio to first order value*

	Model	1	2	3	4	5	6
1	Max	1.00	1.11	1.01	1.03	1.03	1.21
	Sta.Dev	1.00	1.01	1.00	0.99	1.01	1.03
2	Max	1.00	1.16	1.02	1.03	1.08	1.37
	Sta.Dev	1.00	1.02	1.00	0.98	1.02	1.04
3	Max	1.00	1.18	1.03	1.03	1.10	1.41
	Sta.Dev	1.00	1.02	1.00	0.98	1.03	1.05
4	Max	1.00	1.17	1.05	1.02	1.17	1.45
	Sta.Dev	1.00	1.02	1.00	0.98	1.04	1.04

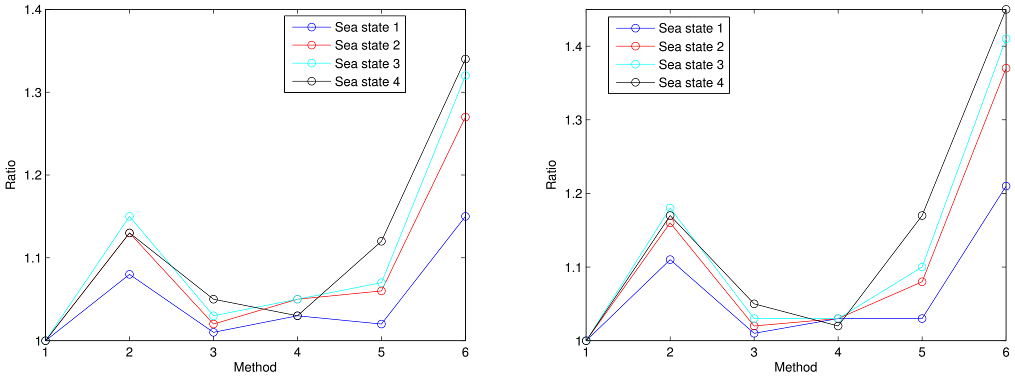

(a) shear force compare

(b) bending moment compare

Figure 3.13: *Comparison of foundation base shear, bending moment calculated with various loads model, ratio to first order value*

Rainey get the largest base shear, compared to first order solution integrated to mean water surface. Wheeler's method mildly adds another 1% to 5% of first order solution to account for the wave zone loads. In comparison, the loads included by second order irregular wave model are a lot higher, varying from 2% to 12%. The tendency observed here is also present in the bending moment at foundation base, see table 3.10. Non-linear models even increase the bending moment at the foundation base to a larger extent.

Standard deviation shows the variability of the data from the mean value, and can be used as an indicator for fatigue damage. Table 3.9 and 3.10 also contain information about the how the results spread out over a large range of shear forces or bending moments. Wheeler's model, though it modifies wave loads in the wave zone and slightly increase the maximum value, it seldom affects the variation of the loading. In comparision, non-linear wave model and non-linear loads model increase the standard deviation by $2-4$ %. Similar as the maximum value, the difference is more obvious at harsher sea states. Also, it affects bending moment to a larger extent than foundation shear.

Apart from maximum foundation shear and bending moment, another critical aspect that governs monopile design is the distribution of loads in frequency domain. Fast

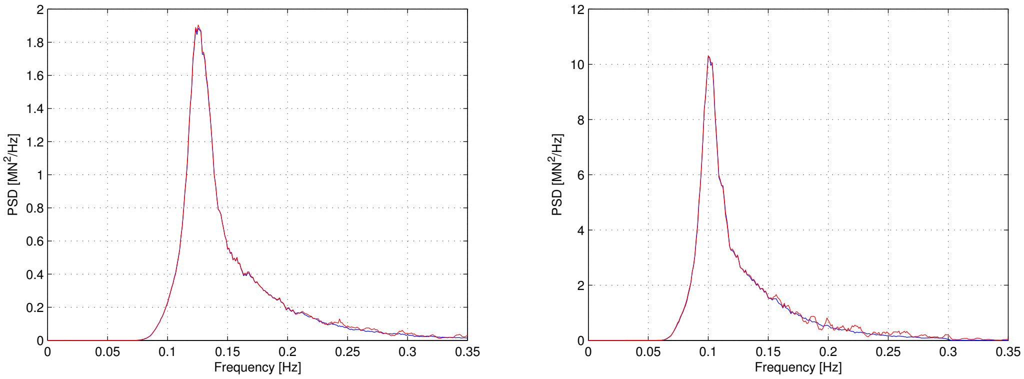

(a) Sea State 1 (b) Sea State 4

Figure 3.14: *Load comparison 1, blue: Linear Morison, red: Linear Rainey*

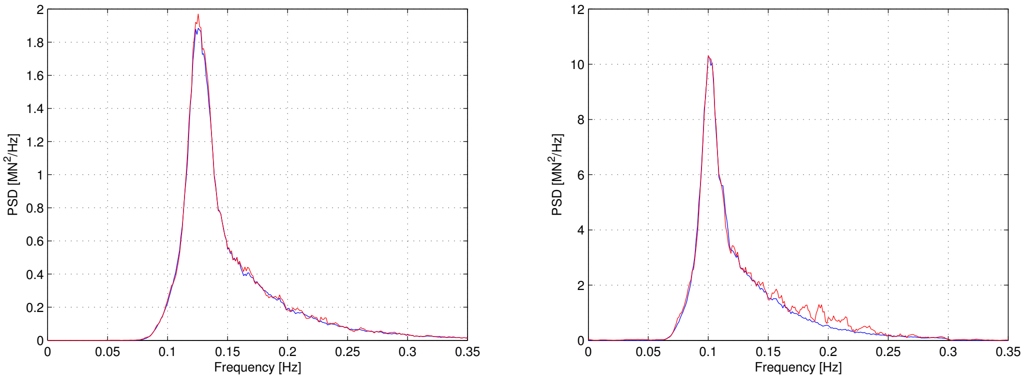

(a) Sea State 1 (b) Sea State 4

Figure 3.15: *Load comparison 2, blue: Linear Morison, red: Non-linear Morison*

fourier transformation method conveniently transfers time series of loading into frequency domain, and shows how the added low frequency and high frequency components affect the power density spectrum. The six load calculation methods are group into three pairs, with 1 and 2 compared to see how the Rainey's method brings in higher order terms at different sea states, 1 and 5 compared to figure out second order effects, 3 and 5 compared to find how Wheeler's streching method works to add the wave zone loads.

Figure 3.14 compares PSD for bending moment at foundation base, when subject to linear irregular wave, and wave force calculated with morison equation and Rainey's new equation for slender structure respectively. On the figure at left, when the sea state is mild, two curves almost overlap, though it shows some deviation from first order solution at high frequency end. The higher order term introduced by Rainey's model is more relevant to a harsher sea state. On the figure to the right side, the red curve, representing a non-linear solution, shows several small local maxima at $f > 0.15Hz$.

Similarly, figure 3.15 shows how non-linear irregular wave model affects power density

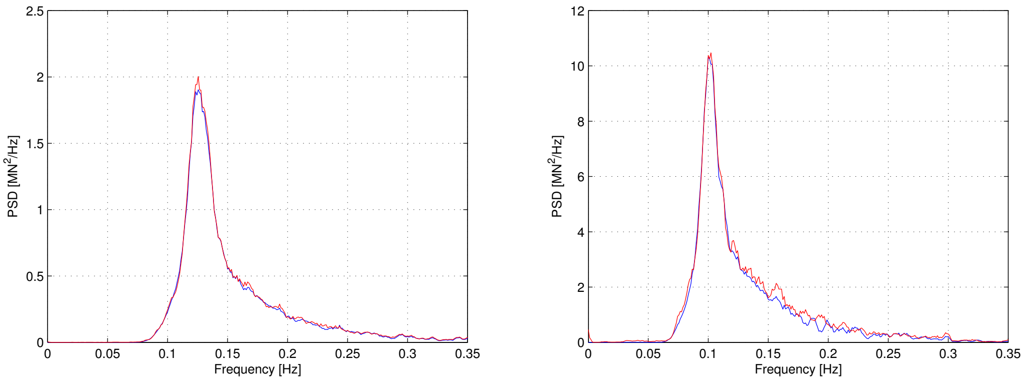

(a) Sea State 1 (b) Sea State 4

Figure 3.16: *Load comparison 3, blue: Linear Rainey, red: Non-linear Rainey*

spectrum for bending moment at foundation base. Different from the previous case, the non-linearity introduced by higher order wave model is present in a mild sea state, by presenting a higher peak at wave peak frequency, and increased PSD at the high frequency range. On the figure to the right, the non-linear wave model increases PSD distributed around $2f_p$. Also, the red curve reach a higher value around $0.05 - 0.1\ Hz$. The enclosed area of PSD, an indicator of energy introduced by the incident wave, is evidently larger when using non-linear model irregular wave model. Similar trend can also be observed in figure 3.16. Second order irregular wave model increases PSD at peak and high frequency end. What's more, low frequency contributions starts to present if Rainey's model is used in combination with second order irregular wave.

To summarize what is observed in the three figures above, all the modified calculation models to some extent alter energy distribution over the frequency range. At a benign sea state, the modified model tends to increase the value at peak frequency, while at a harsher sea state the difference occurs at high frequency end with increased energy distribution at high frequency tail.

Both non-linear wave and loads models include a higher level of energy on the structure, by enclosing a larger area under the power density spectrum curve. But the extent to which non-linear models affects structure design still remains to be determined by considering the dynamic properties of wind turbine and design sea sate selected. Take Siemens 2.3 MW as an example, the rotor speed ranges from 6 to 16 rpm, introducing a rotational frequency that varies from $0.10 - 0.27\ Hz$. Figure 3.17 illustrates how the design wave condition and turbine dynamic properties guide support structure design. The eigenfrequency corresponds to first order bending moment of the offshore wind support structure normally lies between the upper boundary of 1P and the lower boundary of 3P, i.e. the region where the red line is placed in the figure. In case significant higher order components are included in this area, second order irregular wave model shall be consider for design purposes since resonance might occur in this range due to second order contributions.

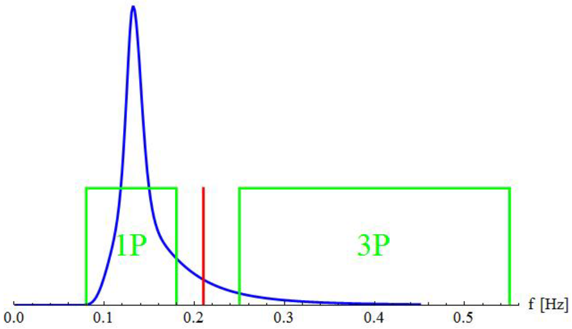

Figure 3.17: *Frequency guided support structure design method*

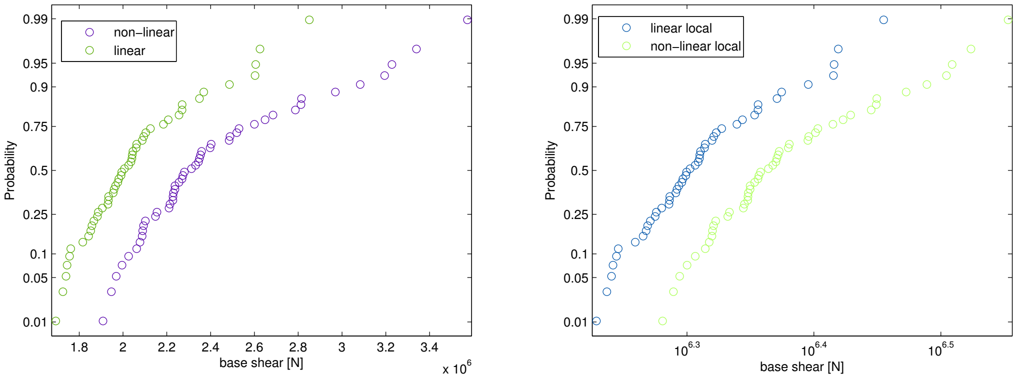

(a) global maxima

(b) local maxima

Figure 3.18: *Extreme value distribution for local and global maxima*

Extreme loads

A long term load extrapolation can help to explain how higher order loads affects ULS design. Forces calculated from model 1 and model 5 will be used for analyzing the distribution of local maximum and global maximum distribution. See from figure 3.18, non-linear model tends to yield higher extreme value than first order solution for both global and local maxima distribution. Figure 3.19 is a Weibull fit for local peaks. Weibull distribution satisfying describes local extremes for the upper part in the figure, while the various outsiders are present in the lower part. However, the trend that non-linear model gives a higher extreme value can still be observed in the fitted curve. For block extremes, i.e. extreme value in each simulation, a Gumbel distribution can be used to fit the distribution. The extreme load extrapolation will be treated in length later in chapter 4.4. As a general conclusion, second order wave models increases long term loads estimations.

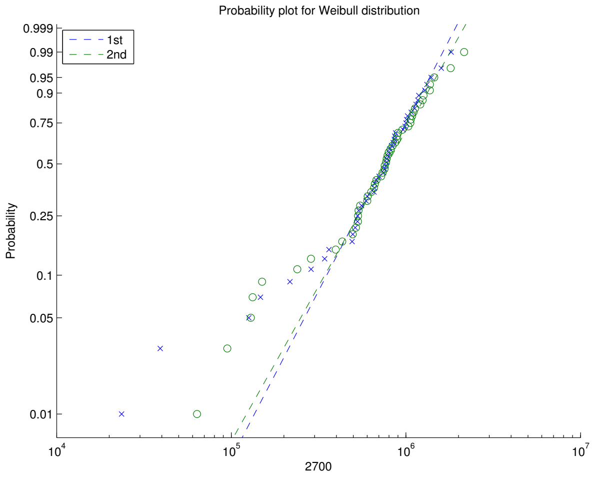

Figure 3.19: *Probability plot for local peaks*

3.6 Conclusion

For a monopile foundation, non-linear wave loads significantly affects loads estimation, with respect to foundation base shear and bending moment. In total, six load calculation methods are compared in analysis. For a severe sea sate, second order irregular wave model increase load at the foundation by 3% to 34%, depending on wave calculation method and environment input. Rainey's load model significantly increases load magnitude, while Wheeler's stretching only mildly modifies wave zone loads. But for a harsh environment condition, the validity of Rainey's model still remains to see, since the 'microseism effect' might occur. When the time series are transferred into frequency domain, higher order frequency terms are present in the wave frequency range. Though dependent on the wave steepness and loads model, higher frequency terms in general affects loads to a greater extend by enclosing higher energy in the spectrum at the high frequency range, while low frequency contributions are secondary. When it comes to fatigue analysis, second order irregular wave model is less critical than the influence on extreme loads, since it only slightly affects force variance.

Chapter 4

Dynamics of Floating Wind Turbine

Second order irregular wave model adds sub-harmonics and super-harmonics in the wave model. For a moored floating turbine, the higher frequency terms might potentially excite the lowest eigen mode of the cylinder hull, resulting in a high bending moment and curvature, while the low frequency components will in most cases affects the dynamic behavior of mooring lines, which are sensitive to low frequency components. Considering that second order irregular waves are most relevant to severe sea sate that normally comes along with a high wind speed, the wind turbines are assumed to be parked for simplification purposes. For the subsequent simulations, aerodynamic forces will be decoupled from the model and the wind turbine is simply treated as a point mass mounted at the top. But the dynamic effects shall still be considered at the end of the project to see if how a coupled model will affect the result significantly. The primary focus of this chapter is on: statistic analysis of loads and response, including displacement, bending moment shear force for both cylinder hull and mooring lines, and some ULS, FLS considerations.

4.1 RIFLEX model

SIMA, short for simulation workbench for marine applications, is a newly developed user interface that enables using SIMO and RIFLEX without experiencing the inconvenience of coding. RIFLEX is a computer program for structural analysis based on finite element method, a tool developed for static and dynamic analysis of slender marine structures, such as mooring lines, and flexible risers, [35]. A very recent development version of RIFLEX includes second order irregular wave model and makes it possible to carry out a non-linear time domain simulation for stochastic analysis with either linear or nonlinear irregular wave model as environment input. The prior interests of the comparison is on the variation of bending moment on the cylinder hull in the wave zone and mooring line attaching points, and axial force on mooring lines. RIFLEX will thus be a desired tool for simulation purposes.

As a tool developed for slender structure analysis, RIFLEX does not included a complicated hydrodynamic model, but Morison equations combined with long wave assumption.

Since the spar hull can be treated as a slender structure due to its relative large longitudinal dimension, the use of Morison equation can be justified, so long as the wave length is relatively large compared with characteristic length of the cylinder. But the surface piercing effects, which are of concern for severe sea states, are not considered in the model.

Based on a Hywind Demo model provided by Marintek, a self-built RIFLEX model was constructed with the same structure properties defined in Neuenkirchen Godø [1]. Appendix B includes a detailed description of Hywind Demo RIFLEX model, which will also be briefly summarized below.

Figures 4.1 and 4.2 respectively shows a layout of mooring system viewing from turbine top and a detailed description of the mooring lines from side. The structural properties of lines will not be elaborated here, but in the Appendix B.

The cylinder hull model is composed of two lines, line 1 running from the keel to the mooring point and line 2 covers the rest of the structure. Table 4.1 shows the segment of which the data will be stored and analyzed during the time domain simulation. Nodes on line 2 will provide information on how the non-linear loads affect the dynamic response in the wave zone, while the nodes on the mooring lines will assist in analyzing the mooring line motion resulting from low frequency components.

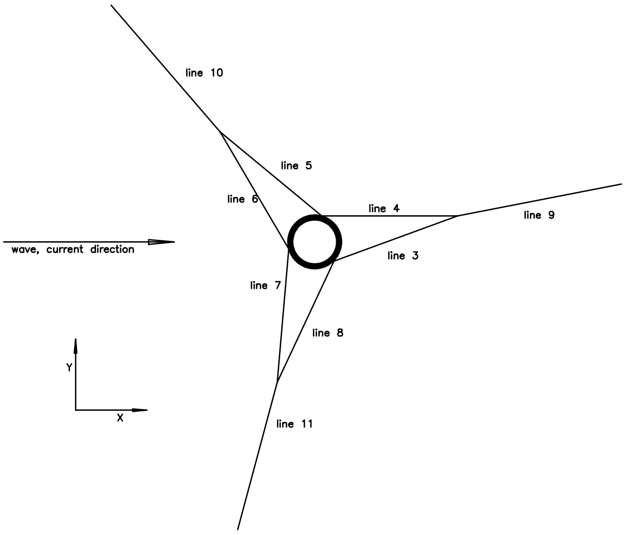

Figure 4.1: *Mooring system layout*

The analysis basically follows the standard RIFLEX simulation procedure. Static analysis achieves structure position in a equilibrium state. Afterwards dynamic forces are exerted on the model to study the dynamic response of the structure. The output files, containing information on nodal displacement and force, will be post processed in Matlab for comparison purposes. The comparison focus primarily on how second order irregular wave affects power spectrum and long term extreme value prediction and fatigue estimation.

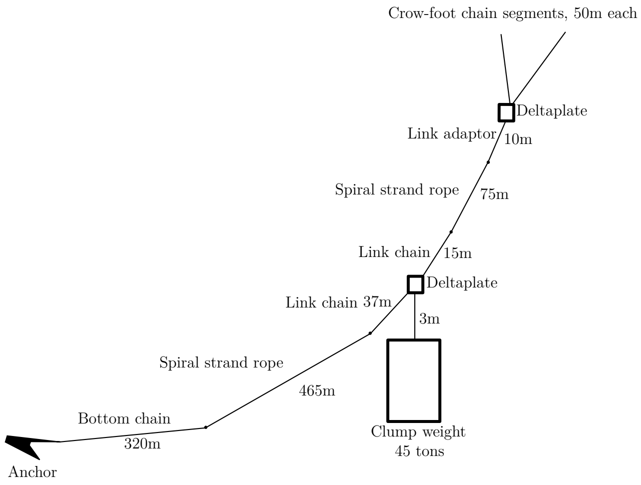
Crow-foot chain segments, 50m each
Deltaplate
Link adaptor
10m
Spiral strand rope
75m
Link chain
15m
Deltaplate
Link chain 37m
3m
Spiral strand rope
465m
Bottom chain
320m
Anchor
Clump weight
45 tons

Figure 4.2: *Mooring line configuration [1]*

Table 4.1: *Hywind wind model brief*

Line	Segment No.	Node No.	Location description
line 1	16	1	mooring point
line 2	17	1	6 m below free water surface
	21	1	free water surface
	25	1	6 m above free water surface
line 3-8	1	1	delta lines
line 9-11	6	5	main mooring lines

4.2 Environmental Input

4.2.1 Wave

The development version of RIFLEX exerts some limitations on using second order wave integration. Second order wave model is available for only severe sea states. Also, there is some incompatibility in using second order non-linear wave to model a regular or bicromatic wave in RIFLEX 4.1.5. Thus only stochastic sea states, represented by JONSWAP, will be used as wave input.

4.2.2 Current

A simplified current model, transporting in wave direction, is used in analysis. Values are based on measurements at the Troll field, and adopted for Hywind Demo site [1], see table 4.2 and figure 4.3. The values varies linearly between two consecutive water levels.

Table 4.2: *Current profile*

Water level	[m]	3	25	50	100	200
Current speed	[m/s]	1.70	1.22	1.14	0.77	0.73

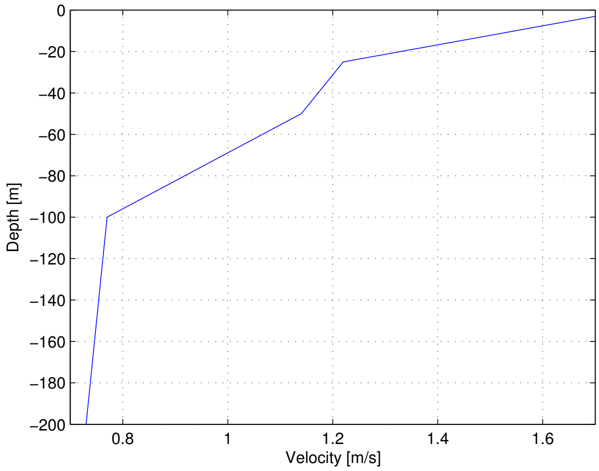

Figure 4.3: *Current profile*

4.2.3 Wind

Aerodynamic forces can be conveniently included in the RIFLEX model by either using the self built-in wind turbine model or a coupled model with AeroDyn. But considering the nonlinear wave model already significantly increase computation time, and wind turbines are normally parked at a severe sea state, aerodynamic effects are ignored.

4.2.4 Second order irregular wave

The previous chapter introduces second order irregular wave model for an infinite water depth site by comparing the wave records, generated wave spectrum and wave kinematics. In deep water, the sum-frequency part is expected to vanish and difference frequency part to be present. Figure 3.7 shows the wave spectrum at a deep water site, with the input defined as $H_s = 5\ m,\ T_p = 12\ s,\ \gamma = 3.3$. Different from spectrum for a shallow water site, both sub-harmonics and super-harmonics are absent in figure (a) 4.4. However, contributions from correction terms start to be present at a severer sea state, displaying sum-frequency contributions and some minor deviation from the first order spectrum at the low frequency end, see figure (b) on 4.4.

To confirm the existence of second order corrections in a deep water site, a bichromatic wave, composed of $T_1 = 8\ s,\ T_2 = 12\ s, A_1 = 2\ m, A_2 = 2\ m$, is used as wave input. Figure 4.5 is the power spectrum based on numerical time records. There are in total six frequency components present in the figure, corresponding to two wave frequency components, three sum-frequency contributions and one difference frequency correction. Among the additional four frequency components resulting from second order potential corrections, the highest two frequency in comparison contains more energy, though all these correction terms are of secondary to the composition of energy spectrum.

Figure 4.6 illustrates how wave kinematics vary over the water depth. Figure (a) and (b) respectively shows the horizontal particle velocity at $z = 0$ and $z = -50$. While sum-frequency components adds to the magnitude of particle velocity, the difference frequency

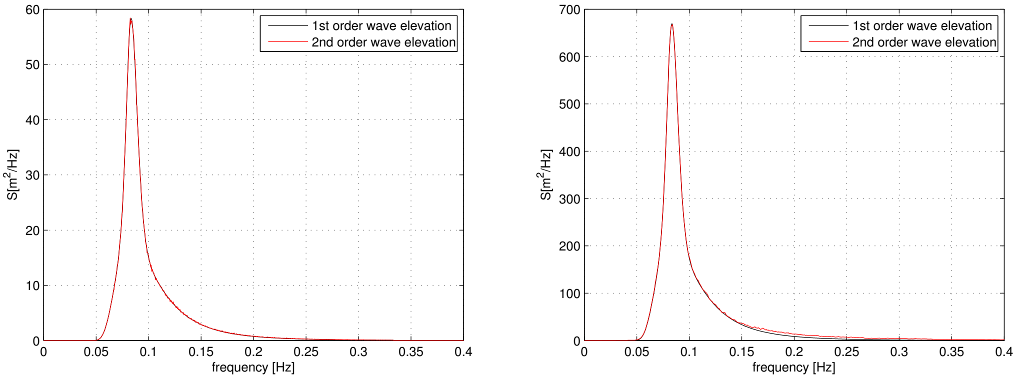

(a) $H_s = 5\ m,\ T_p = 12\ s,\ \gamma = 3.3,\ h = 200\ m$ (b) $H_s = 17\ m,\ T_p = 12\ s,\ \gamma = 3.3,\ h = 200\ m$

Figure 4.4: *Spectrum for wave surface elevation*

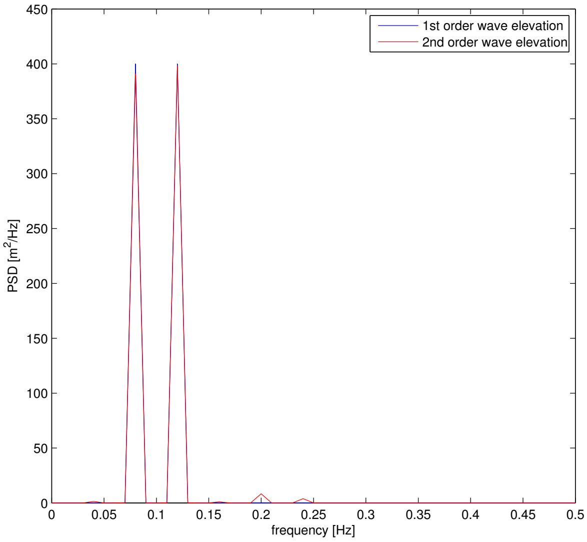

Figure 4.5: *Wave surface elevation spectrum,*
$T_1 = 8\ s,\ T_2 = 12\ s, A_1 = 2\ m, A_2 = 2\ m,\ h = 200\ m$

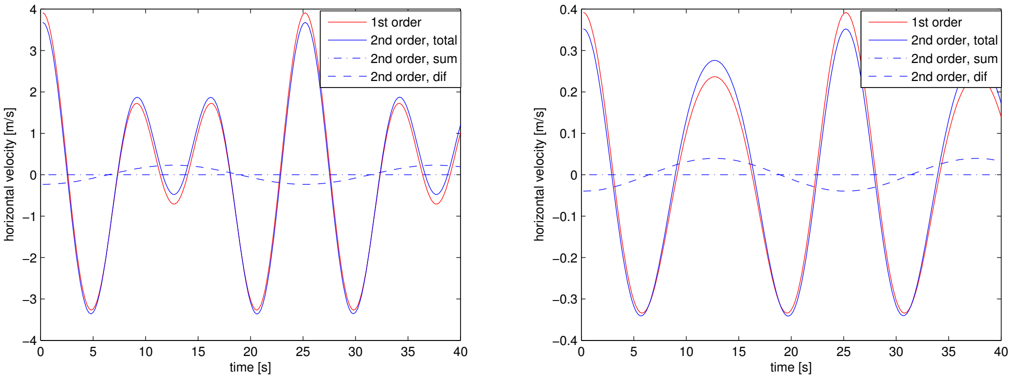

(a) $z = 0\ m$ (b) $z = -50\ m$

Figure 4.6: *Horizontal particle velocity, bichromatic waves,* $h = 200\ m,\ T_1 = 8\ s,\ T_2 = 12\ s, A_1 = 2\ m, A_2 = 2\ m$

counterpart actually reduces the value showing a ‘return current’ effect. The particle velocity reduces with the increase of water depth, but the difference frequency components vanishes in a slower manner.

4.3 Time domain simulation

Step wise integration method works as a numerical tool for solving dynamic vibration problem. Due to the geometric non-linearity introduced by the mooring lines, the dynamic system requires a non-linear solution scheme to determine dynamic response of the system. SIMA utilizes Newmark’s method for solving nonlinear problems. Newark method with $\lambda = 0.5$ and $\beta = 0.25$ is preferred, since it is unconditionally stable for a linear problem with a satisfying period error. To assist with convergence, λ is slightly increased to 0.505 by adding artificial damping to the system. Besides, only the lowest modes are of interests, a relativity large time step, so long as it converge to the real solution, can be chosen in the analysis. However, implicit methods that are unconditionally stable for linear problems, may begin to show instability when used for nonlinear problems, especially for long time simulations[36]. A convergence study is still in need to determine the time increment.

4.3.1 Convergence study

Time domain simulation for a non-linear problem is time consuming. To minimize the computation cost and at the same time ensure the representatives of simulation result, a convergence study is first carried out to determine an optimum time increment used for solving the dynamic equilibrium, and also storage step used for writing into result files. Time step affects total computation time for each simulation, while storage steps decides the time required for importing data into Matlab. The convergence study focuses on how the time step influence the variance of bending moment on the structure part in wave zone

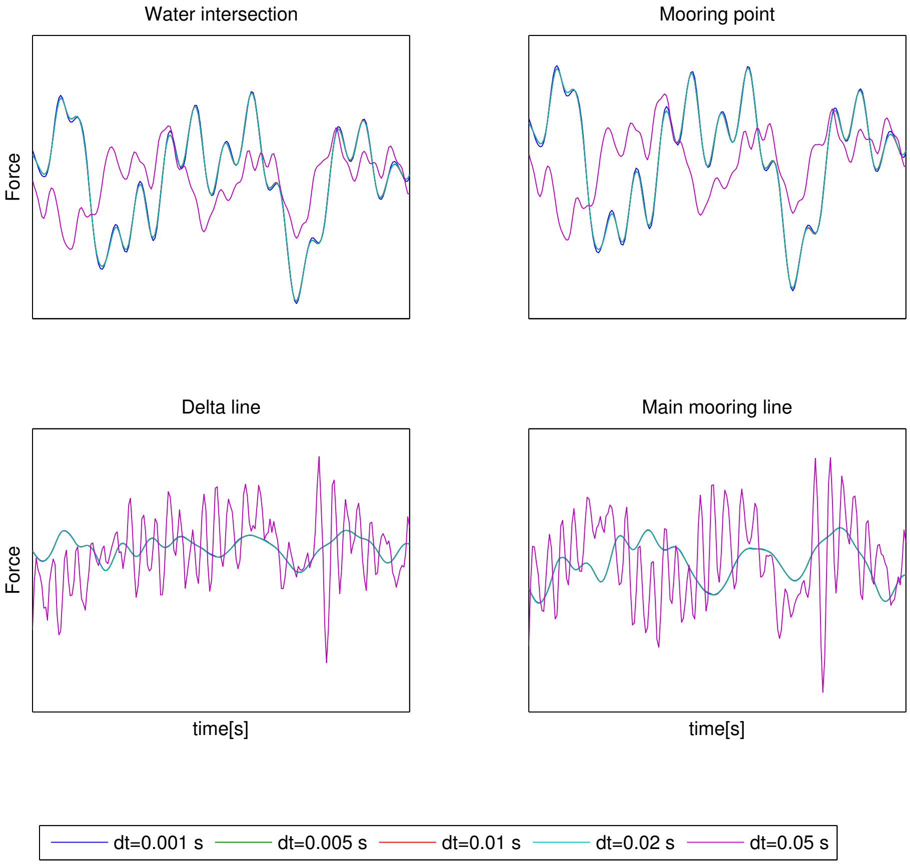

Figure 4.7: *Convergence study, response over various time step*

and the axial force of delta lines and main mooring lines. Four different time increments, dt ranging from 0.001, 0.005, 0.010, and 0.050 are compared, with each simulation lasts 1200s. But error occurs for even smaller time increment. One possible explanation is that the solution lost its stability and results in an unrealistically large value.

Figure 4.7 shows how the time series of bending moment varies with different time increments at surface piercing point in wave zone and axial force in the mooring lines. Results are shown for second order irregular wave model only, considering non-linear wave model should require a smaller time increment to capture the higher order frequency terms introduced. See from the figure, the response tend to diverge when time increment is as large as 0.05, while curves for other increments almost overlap, indicating a convergence trend.

Table 4.3 summarizes total computation time for non-linear time integration for a total simulation length of 1200 s. The computation time grows in proportion to the total time steps taken in each simulation.

Values in table 4.4 comes from the expression $(1 - A/B) \times 100\%$, in which B is the reference value, i.e results for $\Delta t = 0.005$ and A is the value to be compared. See from

Table 4.3: *CPU time for non-linear time integration*

Δ t	[s]	2e-2	1e-2	5e-3	1e-3
time	[s]	743	1359	2629	11723

Table 4.4: *Statistics comparison, different time steps*

		Maximum [%]			Variance [%]		
	Δ t	0.005	0.01	0.02	0.005	0.01	0.02
Location							
Wave intersection		0.72	0.71	0.65	1.10	1.11	1.10
Mooring point		0.67	0.66	0.60	0.99	1.01	0.99
Delta line		0.01	0.01	0.01	-0.31	-0.32	-0.34
Main Mooring line		0.00	0.00	0.00	-0.15	-0.15	-0.16

the table, a more delicate division of time do result in an improved description of maximum value, but in a subtle manner. In comparison, it seldom affects the maximum axial force in the mooring lines, though it to some extend reduces the variance. Considering both computation cost and accuracy requirement, the time increment is determined to be 0.01s.

While time increment affects time required for each simulation , the storage step decides the efficiency of data post-processing in Matlab. A series of time step, ranging from 1 to 20 with an increment of 5, are tested to determine the storage step. It shows that when results are stored every 10 steps, the change of maximum value will be within 0.05% and 0.07% for variance.

To sum up, simulations below use the time increment of 0.01 s and the response results are written into the result files very 10 steps, i.e. the output files contain information for the dynamic responses in every other 0.1 s. The maximum response frequency is thus 10Hz, which still cover the lowest igenmodes that are of interests.

4.3.2 Dynamic analysis

To study how second order irregular wave model affects the dynamics of Hywind, a sea state, characterized by $T_p = 6\ s$, $H_s = 6\ m$ is introduced as environmental excitation. The results presented are based on 20 simulations. Each simulation lasts 6200 s and repeated 20 times with seed number ranging from $1 - 20$. First order and second order wave input share exactly the same seed number. The time series presented below are based on the simulation results of seed 1 while power spectral density function is formulated with averages of 20 simulations. The *smooth* command in the fit curve tool box assists to show the curve in a more elegant manner.

In the RIFLEX model, the cylinder hull are modeled as beams. For beam elements, the dynamic behavior are characterized by the bending moment, shear force and displacement. Figure 4.9 and figure 4.8 respectively show the dynamic response of the structure at mooring point and wave-structure intersection. Figures in the first column shows time

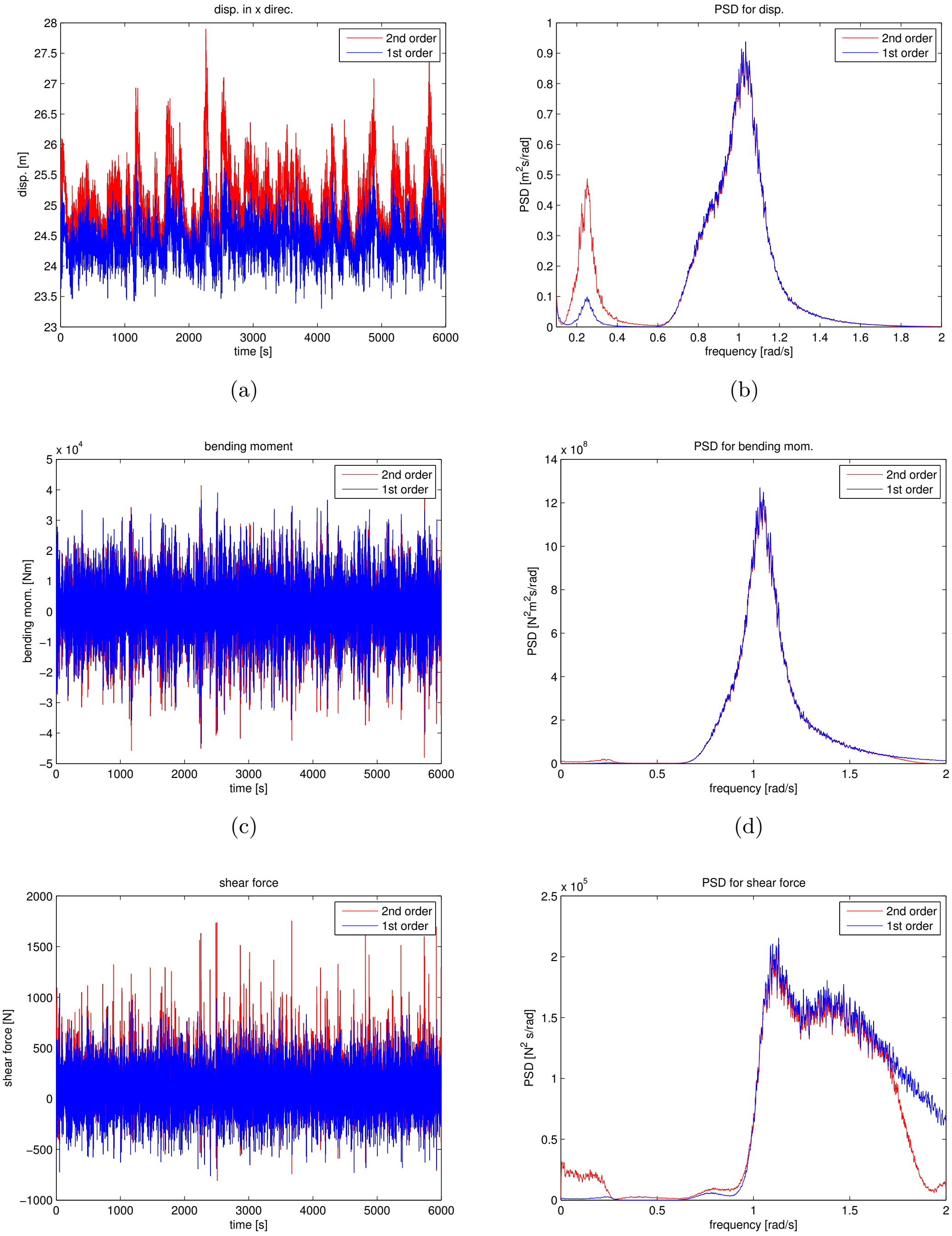

(a) (b)

(c) (d)

(e) (f)

Figure 4.8: *Dynamic response of cylinder hull in wave zone,* $H_s = 6\ m, T_p = 6\ s$

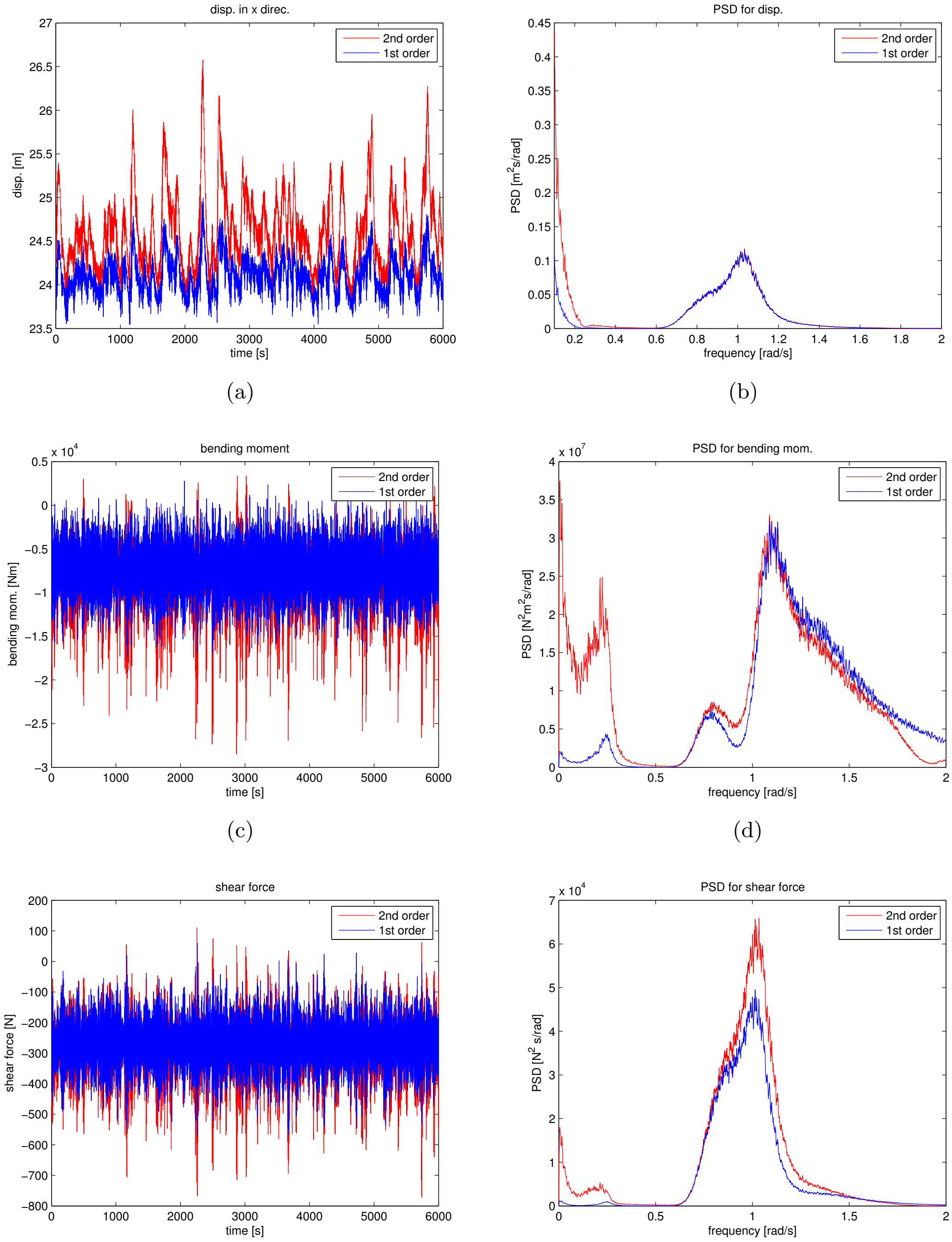

(a) (b) (c) (d) (e) (f)

Figure 4.9: *Dynamics of cylinder hull at mooring point,* $H_s = 6\ m, T_p = 6\ s$

domain variations, while figures on the second column shows FFT transformation of time series into frequency domain. See from the figures, the modified wave model results in a larger displacement from its mean position, and a re-distribute of energy spectrum by increasing PSD in the low frequency range.

Figure 4.8 illustrates the dynamic behavior of a point located 6 m below mean water level in static position. See from the time records, second order wave input causes an additional 0.5 m mean displacement in x direction, and at the same time differentiate it from first order solution by displaying increased maximum displacements and a larger variation. Bending moment variation overlaps with first order solution, but it includes a significantly increased number of negative peaks. At this location, the maximum positive and negative force are the same when using linear wave input, which is not the case for second order solution. Larsen et al. [15] looked into the asymmetry caused by Stokes five order wave, which can also be an explanation for the asymmetry observed. Briefly speaking, when the surface elevation is considered in wave modeling, the maximum negative and positive force do not appear at the same water level. The third row in the figure shows the statics properties of shear force. It is noticed that second order wave model results in significantly higher local and global peaks. With kurtosis reached 6.5 and skewness increased to 1.11, strong non-linearity are present in shear force records. In comparison, first order solution is symmetric and Gaussian distributed. Figures in the second column assists in explaining the difference. See from the frequency domain solutions, second order corrections terms, mainly low frequency components, magnifies the dynamic response at the frequency around 0.23 rad/s. The amplification effects can also be clearly observed in the PSD for displacement and shear force, while there is only a hardly observable local peak in figure (d) around 0.23 rad/s. 0.23 rad/s corresponds to a period of 27.3 s, which is close to the natural period of pitch 25.00 s and heave motion 27.78 s. When second order irregular wave is applied, heave motion is dominated by low frequency motion and turns wave frequency motion to be secondary. RIFLEX output files contain information on transnational displacements only, but rotational displacement. Assuming local deformation on the cylinder is negligible compared to surge motion, the pitch angle can be calculated using the ratio between the difference of $x-$displacement at two water levels and its distance along the hull. Different from heave, pitch motion still exhibits wave frequency motion, in addition to the magnified low frequency motion in low frequency range.

Similar trends can also be observed in figure 4.9, showing asymmetry in loading profile and amplified energy distribution around 0.23 rad/s. While there is a only slight deformation of PSD for bending moment in figure 4.8, second order wave model significantly intensify the vibration in the low frequency range. For the time series of bending moment, the negative maximum is twice as large as first order solution maximum. When it comes to shear force, amplification effects are present at both wave peak frequency region and low frequency range. Second order wave model works to increase the maximum shear force by 45

To sum up, the improved wave model introduced significant low frequency contributions, which might excite resonance. The model also cause asymmetry in load profile and results in higher peaks.

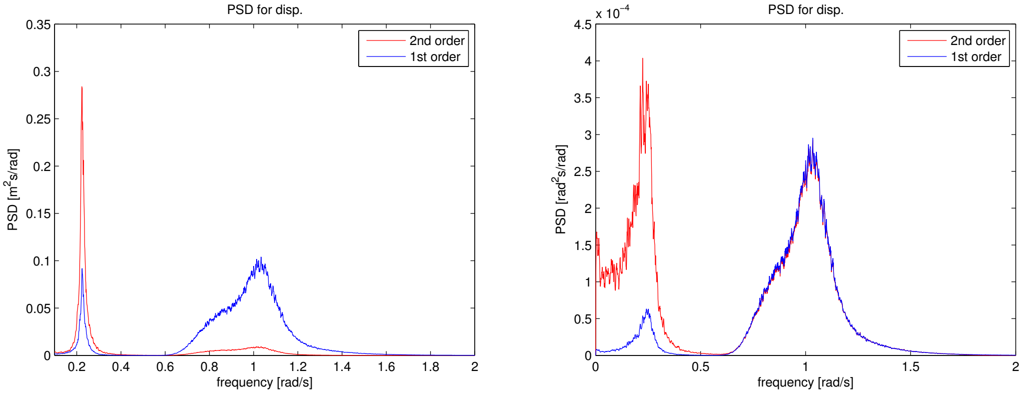

(a) heave (b) pitch

Figure 4.10: *Heave and pitch motion of cylinder hull,* $H_s = 6\ m, T_p = 6\ s$

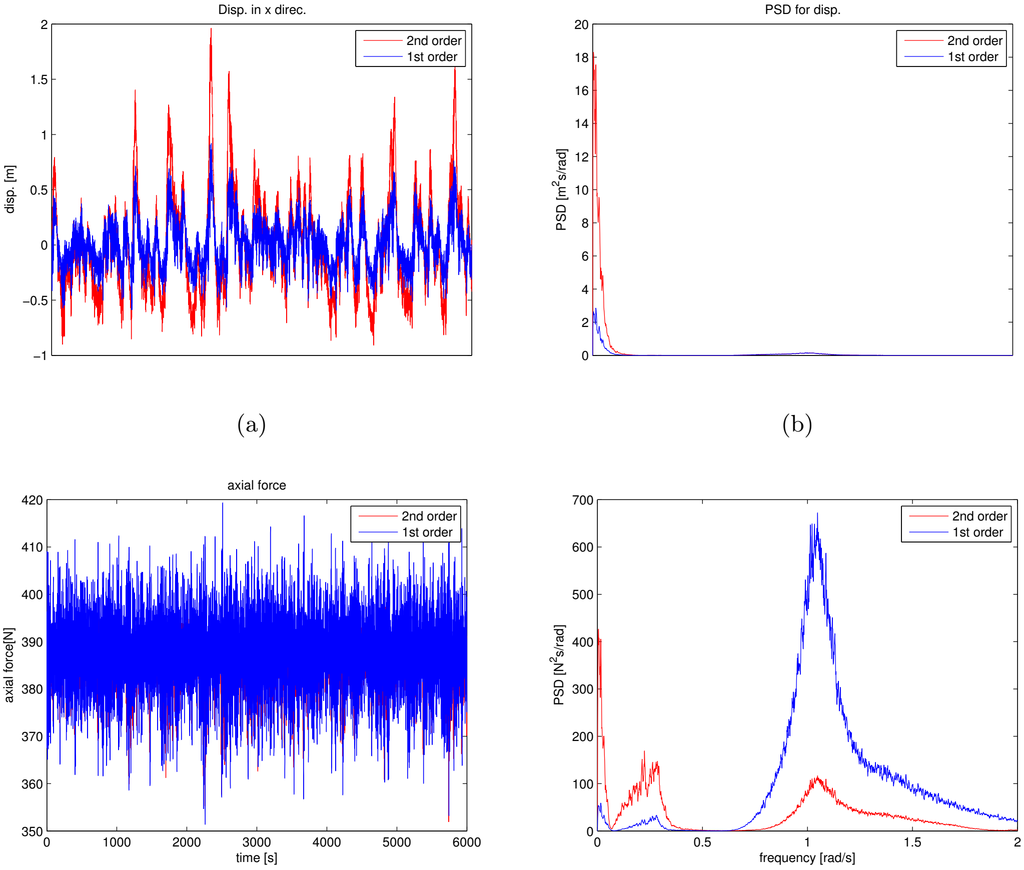

(c) (d)

Figure 4.11: *Dynamics of delta line, line 3,*$H_s = 6\ m, T_p = 6\ s$

In the RIFLEX model, mooring lines are treated as bar elements, which is subject to axial force only. Figure 4.11 shows the dynamics of delta line calculated with two wave models.

An increased maximum displacement from its equilibrium position is also represent, see from figure (a). Different from the dynamics at cylinder hull, mooring displacement is dominated by low frequency vibrations, displaying a high peak close to zero in the power spectrum without showing wave frequency motion. Though second order model only moderately changes the magnitude of axial force, it actually alters energy distribution to a great extent. With more energy enclosed in low frequency range, there is a shift of energy distribution between two peaks at $0.2rad/s$, and $1.1rad/s$ corresponding to incident wave peak frequency. Similar trends can also be observed in figure 4.12. On the main mooring line, the non-linear wave model increases the displacement, and reduces the PSD value at wave peak frequency. The total energy extracted from wave is significantly reduced. Possible explanation can be the inclusion of low frequency terms. Though all the wave kinematic terms vanish with the increment of water depth, low frequency components decrease in a slower manner. In deep water, sum-frequency contributions are absent, which means only low frequency terms are added. When low frequency terms take over, it will reduce the inertia forces acting on the mooring lines. Slower variation means a reduced acceleration and consequently a lower inertia force term exerted as excitation. On the other hand, second order difference components exhibit a 'return current', which reduces wave kinematic and consequence the forces acting on the mooring line.

Conclusions drawn above are also confirmed by the statistics comparison in table 4.5. Table 4.5 shows the statistics of forces acting on the structure from two types of analysis, loading from first order wave, and second order irregular wave, based on averages of twenty simulations. For the environment set $H_s = 6\ m,\ T_p = 6\ s$, the maximum bending moment at mooring point is increased by 95.51%, while at the surface piercing point it is increased by around 20%. The effects of second order wave model on shear force are also vital influence at either water intersection or at the mooring point, displaying around $10 - 30\%$ increase of the maximum value. But for axial force on mooring lines, it actually reduces its maximum value by $2.32 - 2.45\%$depending on its relative position to wave direction.

However, the extent to which second order irregular wave model affects design loads still remains to be investigated. Due to the excited low frequency mode around 0.25 rad/s, second order wave model might not exert similar amplification effect when use other environment inputs. Also, the condition set exerts a high loads using linear model might not be of as critical when using non-linear wave model. It is thus necessary to look into how second order wave model affects mooring line design by varying wave condition, which will be dealt with in detail in the following section.

4.4 Extreme load

Another critical aspect of design calculation is to establish long term extreme loads. For a floating wind turbine, the ultimate limit state normally corresponds to 50 year level response. Based on analysis in previous chapter, the adaption of second order irregular wave significantly changes most probable maximum during 20 simulation at some segment of the structural model. The second order modification also alters the distribution for global maximum. To gain a further understanding of how the wave model affects structure

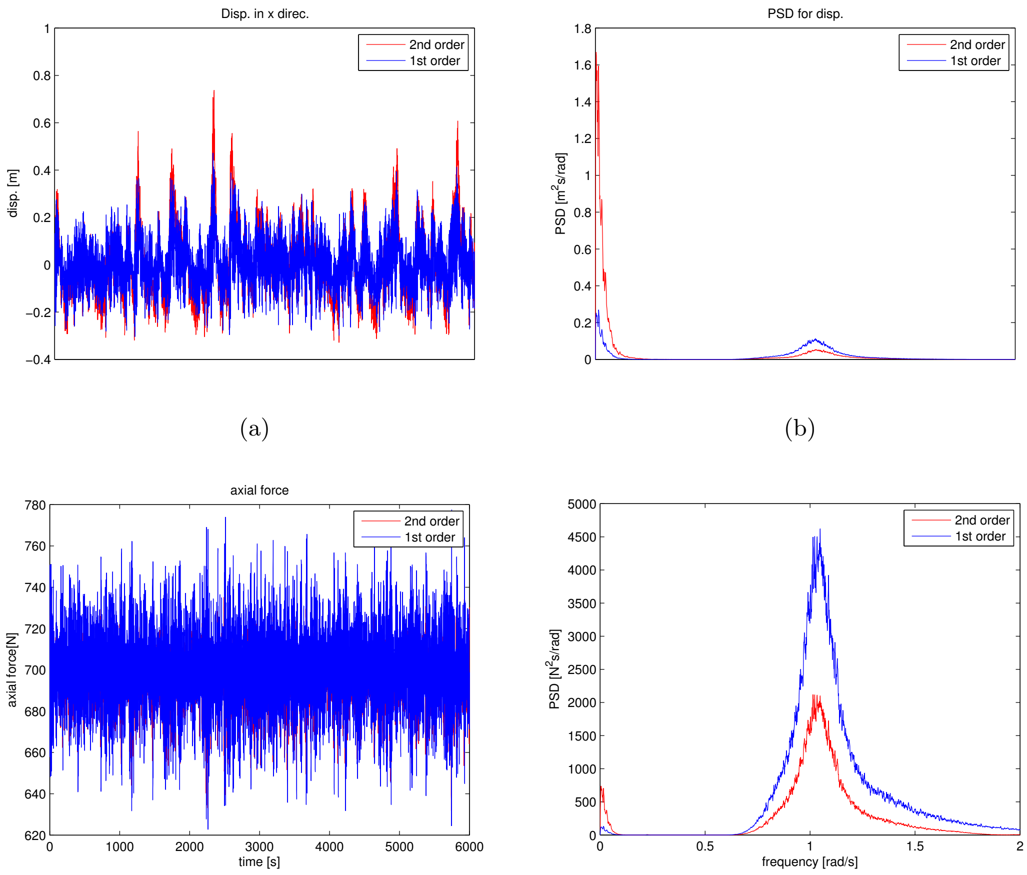

(a) (b)

(c) (d)

Figure 4.12: *Dynamic response of main mooring line, line 9,* $H_s = 6\ m, T_p = 6\ s$

design, it will be of help to determine long term extreme loads based on short term simulations.

Generally, extreme load prediction can be calculated in either a deterministic or a reliability based manner. When using the deterministic approach, a 50-year sea state needs to be predefined and the calculated results correspond the targeted ULS level. The deterministic approach saves considerable computation time, but it generates a relatively conservative result. In comparision, reliability based method returns a more satisfying estimation. Reliability method also provide two approaches, full long term all sea state analysis and contour line method.

4.4.1 Full long term all sea state approach

In the present study, the probability distributions for wind and current are decoupled from wave, which makes it possible to conveniently express the probability for response

Table 4.5: *Dynamic response statistics,* $H_s = 6\ m, T_p = 6\ s$

	Bending Moment[Nm]		
	2nd	1st	Δ
Mooring point	3.83E+04	1.98E+04	95.51%
Water intersection	4.14E+04	3.33E+04	18.85%
	∼ 4.94E+04	∼ 4.61E+04	∼ 24.16%
	Axial Force [N]		
	2nd	1st	Δ
Delta line	4.03E+02	4.19E+02	-3.90%
	∼ 8.56E+03	∼8.77E+02	∼2.81%
Main mooring line	7.42E+02	7.77E+02	-2.32%
	∼1.52E+03	∼1.56E+03	∼-4.51%
	Shear Force [N]		
	2nd	1st	Δ
Mooring point	8.15E+02	5.65E+02	44.01%
Water intersection	1.15E+03	1.01E+03	14.18%
	∼1.59E+03	∼ 1.13E+03	∼40.61%

x to occur as,

$$F_{X_d}(x) = \int_h \int_t F_{X_d|H_sT_p}(x|h,t)\, f_{H_d,T_p}(h,t)\, dtdh \tag{4.1}$$

$f_{H_d,T_p}(h,t)$ is the joint probability density function of the sea sate parameters, which is site specific. For analysis purposes, a North Sea wave climate, for which a Weibull distribution has been fit to Hs [37]will be assumed for Hywind Demo site:

$$P[H_s < h] = F_{H_s}(h) = 1 - exp[-(h/2.822)^{1.547}] \tag{4.2}$$

Conditional on H_s, T_p is assumed log-normally distributed, characterized with:

$$E[lnT_p] = 1.59 + 0.42ln(H_s + 2) \tag{4.3}$$

$$Var[lnT_p|H_s] = 0.005 + 0.085exp(-0.13H_s^{1.34}) \tag{4.4}$$

and

$$f_{H_d,T_p}(h,t) = P[H_s < h] \times P[T_p < t|H_s] \tag{4.5}$$

$F_{X_d|H_sT_p}(x|h,t)$ is the short term distribution of the maximum over simulation time d. When evaluating d-hour extremes, $F_{X_d|H_sT_p}(x|h,t)$ is always modeled with Gumbel distribution (see equation), so long as the initial response process can be treated as Gaussian.

$$F_{X_d|H_sT_p}(x|h,t) = exp\left\{-exp\left[-\left(\frac{x-\gamma_G}{\beta_G}\right)\right]\right\} \tag{4.6}$$

If the global maxima, i.e. peaks between zero-crossings, is Rayleigh distributed, the Gumbel parameter are given as,

$$\gamma_G = \sigma_d(h,t)\sqrt{2ln(N)} \tag{4.7}$$

$$\beta_G = \frac{\sigma_d(h,t)}{\sqrt{2ln(N)}} \tag{4.8}$$

However, within the scope of the project, second order irregular wave model, and geometric non-linearity in the mooring lines make the above assumption invalid. But still, the response maxima for a non-linear problems can be modeled with Weilbull distribution. The Gumbel distribution is well suited if the initial distribution has an exponential tail, but the parameters need to be modified [1] as:

$$\beta_G = \frac{\pi}{6}s \tag{4.9}$$

$$\gamma_G = \bar{x} - 0.577\beta \tag{4.10}$$

$\bar{x}$, s are the mean and standard deviation of d-hour maximum in k simulations.

Another alternative is to apply Generalized Extreme Value Distribution. *Like the extreme value distribution, also called Gumbel distribution, the generalized extreme value distribution is often used to model the smallest or largest value among a large set of independent, identically distributed random values representing measurements or observations*[38]. In case the modified Gumbel parameters fail to describe the distribution of block maxima, the generalized extreme distribution type will be utilized to fit the extreme value distribution.

With above calculated, the response that correspond to a return period of T years, i.e. with the probability of occurring once, is formulated as,

$$1 - F_{X_d|H_sT_p}(x|h,t) = \frac{1}{N_{d,T}} \tag{4.11}$$

in which, $N_{d,T}$ is the number of d hour sea state in T years, $N_{d,T} = \frac{T\cdot 365\cdot 24}{d}$. At a north sea environment, each sea state realization normally cover a three hour period. But when the simulation time is set to to 1120 s, error occurs in RIFLEX due to the failure in generating second order irregular waves. Based on trials, the simulation time is chosen as 6200 s. With transient state response removed from the time series, the data that can be used for analysis covers one hour and a half.

All sea state long term analysis give a desirable prediction for long term loads, but at a high computation cost. The integration requires a knowledge of the response over a considerable number of sea states, with several realizations at each sea sate. For linear problems, the method can still be an efficient approach when the problem is solved in frequency domain. But for a non-linear problem, which normally requires a time domain simulation with small time increment, this method will be rather demanding in computation cost. Contour line method can be an alternative.

4.4.2 Contour line method

Compared with all sea state long term analysis, contour line method excludes short term variations. A good example of short term variation is the difference between two realizations of the same sea state with different seed number. Due to change of randomly generated phase angle, the two wave series are not identical and result in short term variance. As a benefit of ignoring short term variance, it requires only a limited set of environmental condition to be checked to ensure adequate structure capacity.

When short term variation is ignored, the response X_T, corresponds to T-year level, can be estimated by analyzing short-term response along the T-year environmental contour line. After the environmental design point, where the largest response occurs, is located, the T-year response, X_T , can be replaced by the median value, $x_{50\%}$, of design point d-hour maximum distribution.

To account for the omitted short term variation, it is recommended to inflate the contour line, scale the $x_{50\%}$ by a factor of γ or taking a higher level of percentile, instead of the median as the design response value [39]. However, the remedy for short term variation equally alters first order and second order response. In the remaining part of thesis, this correction method will not be discussed in detail.

Environmental contour line

Figure 4.13 shows $H_s - T_p$ contours for a return periods of 1, 20, 50, 100 year. The curves are obtained by relating H_s and T_p to standard normal variables U_1 and U_2. Rosenblatt transformation transforms the joint distribution function to a standard Gaussian space.

$$U_1 = \Phi^{-1}\left[F_{H_s}(h)\right] \tag{4.12}$$

$$U_2 = \Phi^{-1}\left[F_{T_p|H_s}(t|h)\right] \tag{4.13}$$

In the transformed Gaussian space, the environment condition with the same occurrence probability are located within the same distance from the origin. In this case, it forms a circle with a radius of β by varying two variables, U_1 and U_2:

$$\beta = \sqrt{U_1^2 + U_2^2} \tag{4.14}$$

$$= \Phi^{-1}\left(1 - p_f\right) \tag{4.15}$$

$$= \Phi^{-1}\left(1 - \frac{d}{365 \cdot 24 \cdot T}\right) \tag{4.16}$$

where d is the simulation length of each realization in hours and T the targeted return period. Varying T from 1 to 100, it shows an expanding trend of the envelop. But this tendency becomes less obvious with the increase of T. For a 50 year contour, $p_f = 1.14e{-}6$ and corresponds to $\beta = 4.72$. Reformulate U_1 and U_2 into a polar coordinate system and relate it to the probability distribution function, the points on the contour line can be conveniently calculated.

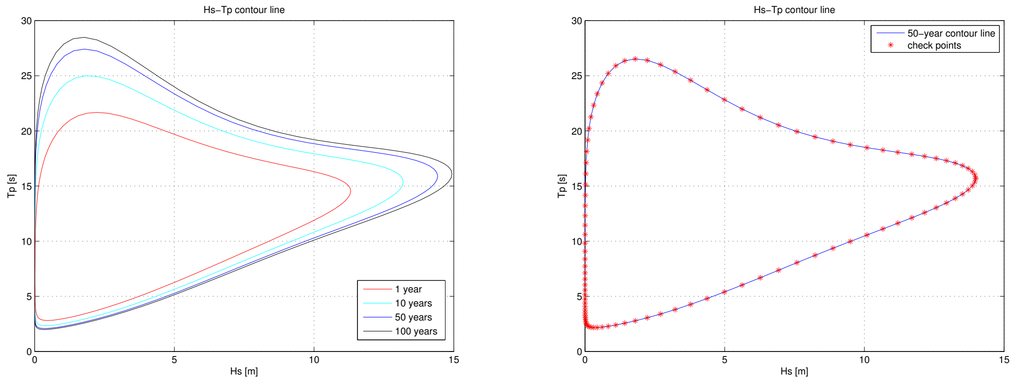

Figure 4.13: *Envrionmental contour lines*

Design point

Figure (b) on 4.13 shows the points to be considered as the potential environment combinations that yield the largest response. Those points to the left side of the figure, with $H_s < 5\ m$, are actually not considered in RIFLEX simulation. On the one hand, the development version of RIFLEX set a lower limit, approximately $H_s = 5\ m$, for generating second order irregular waves series. On the other hand, though those environmental sets that fails in wave initiation has a low probability of occurrence, the corresponding resultant response should not be expected to be critical. Thus only a portion of points on the contour line are used as the environment input in SIMA. The reduced condition sets are assumed to include the targeted environmental design points.

Based on time domain simulations with 56 varying environment condition sets along the 50 year environmental contour line, the design points that results in highest extreme response, are located as follows listed in table 4.6 and 4.7 for linear and non-linear incident wave respectively,

Table 4.6: *Design points, linear wave model*

Location	H_s $[m]$	T_p $[s]$
mooring point	14.3	16.5
intersection	12.6	13.0
delta lines	13.9	17.1
main mooring lines	10.1	10.6

Table 4.7: *Design points, non-linear wave model*

Location	H_s $[m]$	T_p $[s]$
mooring point	13.9	17.1
intersection	13.3	17.5
delta lines	13.3	17.5
main mooring lines	13.3	17.5

Table 4.6 and table 4.7 respectively shows the design points to be considered when using linear wave and non-linear wave as environmental excitation. See from the tables, the environment condition set correspond to the chosen design points vary along the structure, mainly because of the varying of mass and stiffness distribution along the structure. Also, the non-linear wave inputs also alters the location of design point.

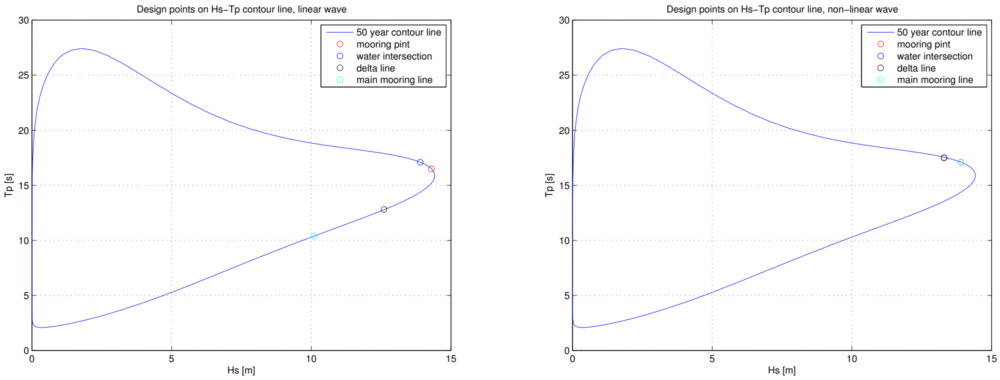

Figure 4.14: Design ponits on the contour line, left first order wave, right, second order

Figure 4.14 shows that for linear wave case, the design points scatter along the contour line, while for non-linear wave case they accumulate at the upper right corner of the contour line. Also, it is noticed a sea state characterized by a relatively large wave height and a small wave period is more likely to result in a large response, since all the design points are located at the lower half of the contour line.

Extreme distribution

To determine the extreme distribution at design points, multiple realizations of each sea state are required to obtain several global maxima that can be used for distribution fit. As the first attempt, 40 simulations are realized for each environment set. The global maximum in each simulation, 40 in total, will be used to approximate a Gumbel distribution , with Gumbel parameters calculated from equation 4.8 and 4.8.

Figure 4.15 shows how block maxima fit in a Gumbel paper. Outsiders are present in the lower part of the figure, but data points in the upper part follows the fitted Gumbel line in a satisfying manner.

With the extreme distribution defined, the median value, $x_{50\%}$, will can be treated as 50 year ULS design load. Concluded in previous sections, higher order wave model mainly affect the bending moment at mooring point and MSL, and axial forces at the mooring lines. Long term load extrapolation thus focus mainly on those force components.

Table 4.8 summarizes the statistic properties of long term loads, correspond to a return period of 50 years. Due to second order correction terms, the 50-year bending moment on the cylinder hull are increased by 2% at mooring point and 7% at water intersection,

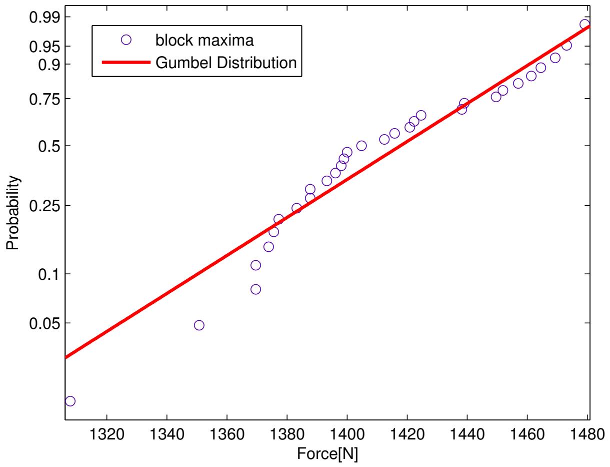

Figure 4.15: *Gumbel Fit*

Table 4.8: *Dynamic response statistics, long term exptrapolation*

	Bending Moment[Nm]		
	1st	2nd	Δ
Mooring point	1.04 e+4	1.07 e+5	2.86%
Water intersection	1.03 e+5	1.13 e+5	7.34%
	Shear Force[N]		
	1st	2nd	Δ
Mooring point	2.22. e+3	2.31 e+3	5.14%
Water intersection	2.14 e+3	2.23 e+3	4.58%
	Axial Force [N]		
	1st	2nd	Δ
Delta line	1.23 e+3	1.02 e+3	-9.08%
Mooring line	1.43 e+3	1.23 e+3	-9.28%

corresponds to a point below mean water level. On the mooring lines, the non-linear wave model reduce the axial force design load by approximately 9%. For the shear forces, it is increased by around 5% at both mooring line attaching point and surface piercing point.

4.5 Fatigue damage

Fatigue design aim to ensure the safe and reliable performance of the offshore wind support structure during its operational life. Fatigue damage is governed by stress range, instead of stress level. Though second order irregular wave alters maximum load level at various part of the structure, it still remains to investigate the extent to which it affects fatigue design.

A FLS analysis normally requires a knowledge of S-N curve and loading conditions for the site. The sea state that attributes the most to fatigue design can be determined based

Table 4.9: Dynamic response statistics, force variance, $H_s = 6\ m$, $T_p = 12\ s$

	Bending Moment$[Nm^2]$		
	1st	2nd	Δ
Mooring point	1.99 e+7	2.09 e+7	4.44%
Water intersection	7.79 e+7	7.75 e+7	+0.49%
	Axial Force$[N^2]$		
Delta line, line 3	3.56 e+2	2.44 e+2	-46.15%
Mooring line, line 9	4.54 e+2	2.00 e+2	-127.05%

on a site specific scatter table, and the resultant fatigue damage can be calculated by Miner-Palmgren's hypothesis,

$$D = \sum_{i=1}^{p} \frac{n_i}{N_i} \tag{4.17}$$

in which D is the accumulated damage, n_i is the number of cycles of stress ranges at level S_i, N_i is the number of cycles that lead to fatigue damage at stress level S_i, p is the total number of stress levels. Rainflow counting is widely employed procedure for determining the load cycle at a certain stress level.

Sea states that affect fatigue level the moment are those with the high occurrence probability and normally corresponds to a significant wave height smaller than 5 m. But due to the limitation of the minimum wave height requirement in RIFLEX, fatigue damage comparison can not be carried out in a deterministic manner. Instead, a comparative caparison by looking into the number of load cycles corresponds to a certain stress level at a selected sea state will be used illustrate how second order irregular wave model affects FLS design.

See from the power spectrum above in figure 4.9, it is evident that the modified wave model affects the energy distribution over its frequency range. But the analyzed sea state, $H_s = 6\ m$ $T_p = 6\ s$ retains a low probability of occurrence. Instead, a $H_s = 6\ m$, $T_p = 12\ s$ sea, which corresponds to a occurrence probability of 1.6 % [40], will be taken as the wave input for fatigue comparison.

Table 4.9 shows the variance of forces acting at various sections of the structure. It is noticed that second order irregular wave model only slightly influence of the variation of forces around the surface piercing, but greatly affects the response variation of mooring lines. Since the force variance can be an indicator for fatigue damage, it is expected that the improved wave model affects mooring line fatigue design to a larger extend than cylinder hull.

Figure 4.16 shows the dynamic behavior of the main mooring line, line 9 at $H_s = 6$, $T_p = 12\ s$. Similar as the environment set $H_s = 6$, $T_p = 6\ s$, the dynamics behavior poses an increased slow frequency motion and reduced wave frequency motion. But the amplification effects around heave and pitch natural frequency are absent.

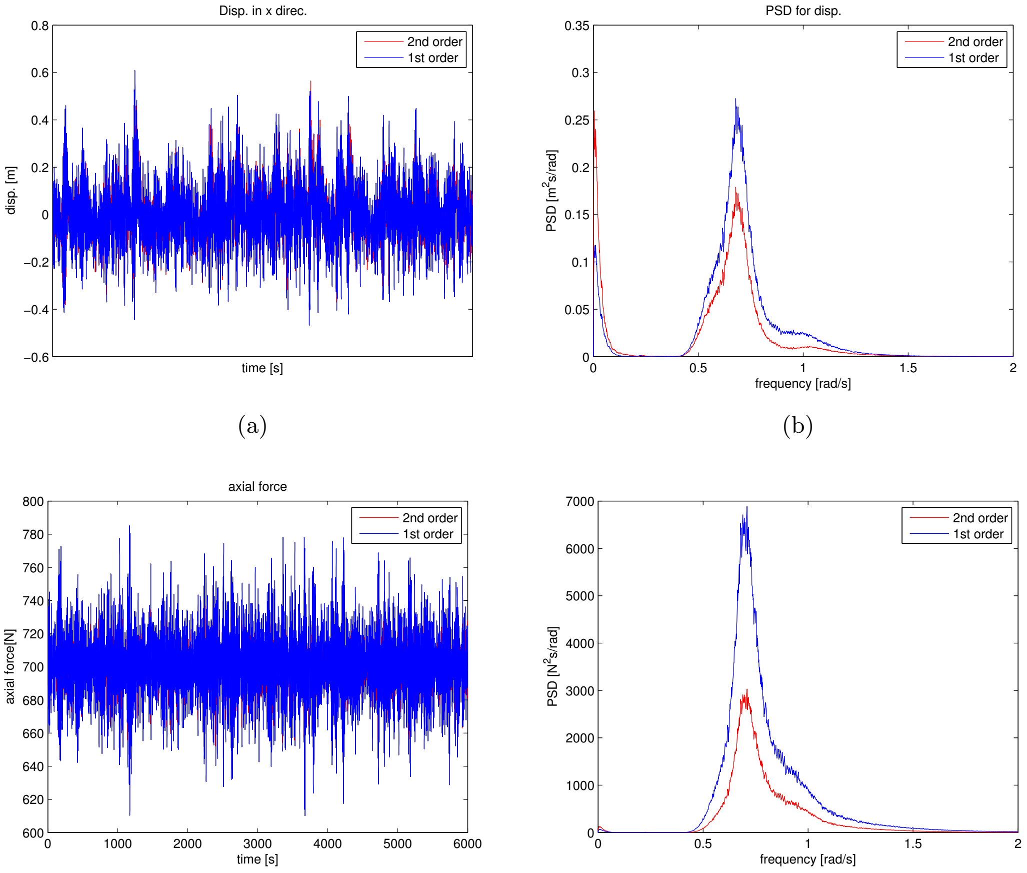

(a) (b)

(c) (d)

Figure 4.16: *Dynamic response on main mooring line 9,* $H_s = 6\ m, T_p = 12\ s$

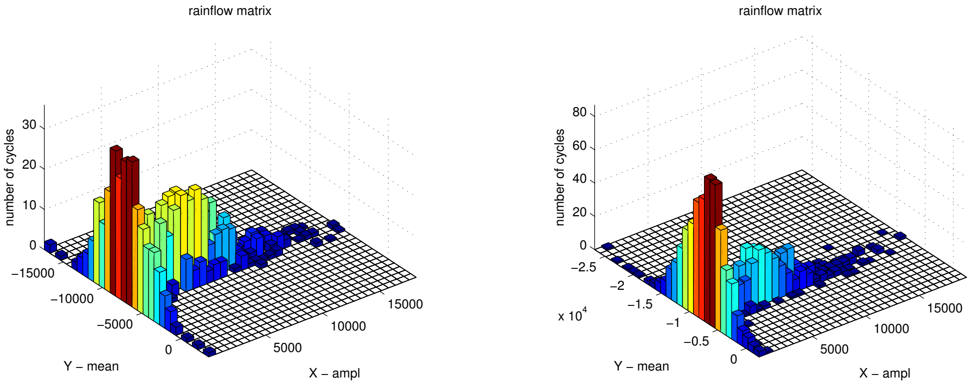

(a) MSL, 1st

(b) MSL, 2nd

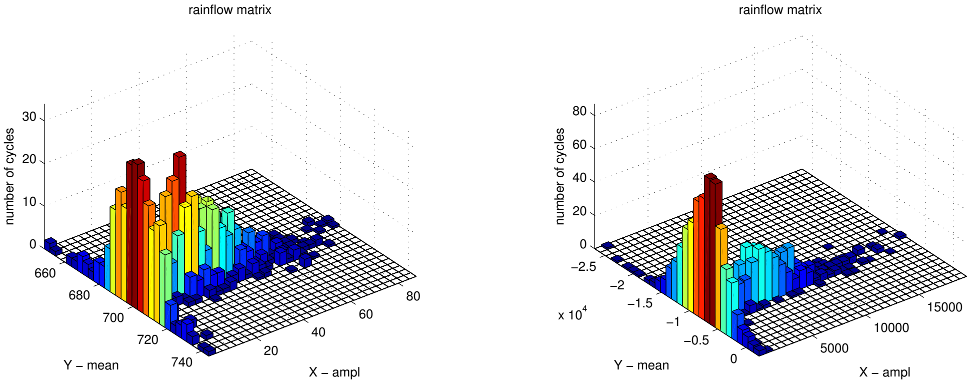

(c) mooring line, 1st

(d) mooring line, 2nd

Figure 4.17: *Rainflow counting matrix,* $H_s = 6\ m,\ T_p = 12\ s,\ t = 6000\ s$

Herein, force variation is assumed to be representive of stress level. Force variations in time, instead of stress, is used as input for Rainflow counting. Figure **??** includes information on rainflow amplitude and mean value versus cycle number, for loading at both MSL and mooring lines. Results from first order wave input are listed in the first column, and the second column corresponds to second order solution. Rainflowing counting analysis utilized Matlab scripts publish online by Nieslony [41]. The general trend is that second order corrections terms increase the cycle number corresponds to small amplitude and medium mean stress level.

When using Miner's law, it is actually the cycle number at each stress level decides fatigue damage. Figure 4.18 projects the rainflow matrix to x-amplitude, showing the cycles numbers corresponds to various stress level at $H_s = 6\ m$, $T_p = 12\ s$ in a 6000 s sea state. At MSL, second order model slightly increase the damage level by increasing the cycle number at the low 'rainflow amplitude' end, and the two curves overlap at high stress tail. Similarly, at the mid-point of the cylinder, minor difference of cycle number occurs at middle range of the 'rainflow amplitude'. Second order terms thus slightly reduce the fatigue damage on cylinder hull. In contrast, second order terms are critical to mooring line fatigue. In consistent with the predictions based on variance values, second order wave model predicts a lower fatigue damage. At the delta line, second order wave model always gives a lower cycle number throughout the complete stress level range, though there some exceptions around $S = 30$. The reduction effect is more strait forward, since second order cycle number approaches zero at high stress level while first order cycle number is still no-zero. In a typical S-N curve, a large stress level normally correspond to a small N.

Based on above analysis, it can be concluded that FLS analysis using first order wave model generates a conservative design for mooring lines, compared to second order condition. However, it seldom affects the fatigue at cylinder hull, though extra wave loads are included in the wave zone. But it should be noticed that above conclusions are based on the assumption the selected sea state $H_s = 6\ m$, $T_p = 12\ s$ is representative for the general wave condition, and cycle for force can be a good indicator for stress variations.

4.6 Conclusion

When it comes to deep water, low frequency contributions will be of primary interests. Though second order irregular wave model introduces both sum frequency and difference frequency components in deep water, contributions from super-harmonics are negligible with regards to both loads and responses. Due the fact that low frequency terms vanishes slower than the rest, sub-harmonics still exerts a comparably more significant influence on structure design, especially mooring line design. The additional sum-frequency terms can potentially reduce the 50-year design load by 9%, calculated with contour line method, and also reduce fatigue damage by displaying fewer cycles at a high stress level. Besides, though it hardly shows noticeable change in the wave spectrum, the low frequency terms introduced can cause significant amplification of vibration by exciting low frequency modes and consequently results in high element force maximum.

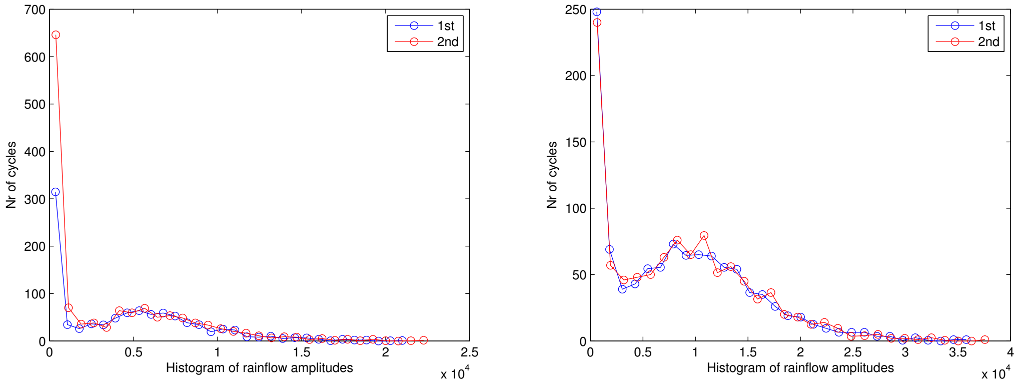

(a) MSL (b) Mooring point

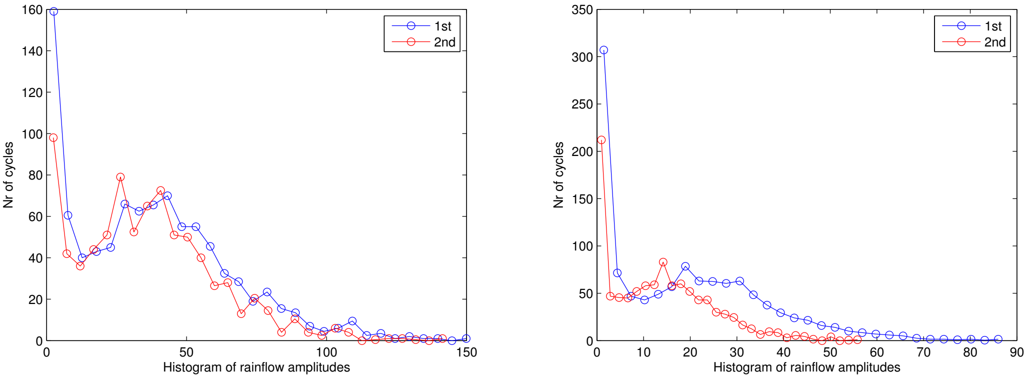

(c) Delta line (d) Main Mooring line

Figure 4.18: *Rainflow counting cycle number comparison, amplitude range versus cycle number,* $H_s = 6\ m$, $T_p = 12\ s$, $t = 6000\ s$

Chapter 5

Conclusions and further work

5.1 Conclusions

A better description of non-linear loads acting on an offshore wind support can be achieved by either implementing a modified hydrodynamic calculation model, or a higher order wave model.

FNV-method and Rainey's new equation for slender structures, both intended to explain third order phenomenon on a offshore structure, include a higher order component at the wave-intersection and modifies inertia term in Morison equation when solving the surface piercing problem. In comparison, Rainey's model is adaptable to a more general loading condition and is preferred in the analysis for offshore wind support structure. Based on modal analysis, it is concluded that the resonance of the lowest eignmode of Hywind will hardly be excited by the higher frequency components introduced by improved hydrodynamic model. However, this improved hydrodynamic model that solves surface piercing included, shall still be considered for extreme sea state wave loads calculation.

An improved description of wave loads also relies on a more sophisticated wave model. Second order irregular wave severs to provide a convenient way to count for both non-linearity in wave and the stochastic nature of sea. The non-linearity introduced is dependent on water depth, wave height and period.

The improved hydrodynamic model and wave model are applied for two types of offshore wind support structure, a bottom founded monopile, and a floating type support structure Hywind Demo.

For a monopile foundation, non-linear wave loads significantly affects extreme loads estimation, with respect to foundation base shear and bending moment. In total, six load calculation methods are compared in analysis. For a severe sea sate, second order irregular wave model increase load at the foundation by 3% to 34%, depending on wave calculation method and environment input. Rainey's load model significantly increases load magnitude, while Wheeler's stretching only mildly modifies wave zone loads. But for a harsh environment condition, the validity of Rainey's model still remains to see, since ' microseism effect' might occur. When the time series are transferred into frequency domain, higher order frequency terms are present in the wave frequency range. Though dependent on the wave steepness and loads model, higher frequency terms in general affects loads to a greater extend and low frequency contributions are secondary by enclosing higher energy in the spectrum at the high frequency tail. When it comes to fatigue analysis, second order irregular wave model is less critical than its influence on extreme loads, since it only slightly affects force variance by 2% to 4%.

When it comes to deep water, low frequency contributions will be of primary interests. Though second order irregular wave model introduces both sum frequency and difference frequency components in deep water, contributions from super-harmonics are negligible with regards to both loads and responses. Due the fact that low frequency terms vanishes slower than the rest, sub-harmonics still exerts a comparably more significant influence on structure design, especially mooring line design. The additional sum-frequency terms can potentially reduce the 50-year design load by 9%, calculated with contour line method, and also reduce fatigue damage by displaying fewer cycles at a high stress level. Besides, though it hardly shows noticeable change in the wave spectrum, the low frequency terms introduced can cause significant amplification of vibration by exciting low frequency modes and consequently results in high element force maximum.

5.2 Further work

Model test is suggested to validate simulation data. Besides, secondary order kinematic corrections shall be tested with measured data. Comparison work done nowadays mainly focuses on wave kinematics in the wave zone, but kinematics under $z < 0$. See from the analysis, second order correction terms below mean water level is critical to mooring line design, but the accuracy of the model is not yet fully explored.

RIFLEX does not include a complicated hydrodynamic calculation model, but Morison equation in combination with long wave assumption. Discussed in previous chapter, the point load at the wave and structure intersection will be critical when wave height is the close to cylinder diameter. Two alternatives, FNV and Rainey can be implemented for including the point loads at the intersection. Importing Rainey's point loads at the intersection into RIFLEX to see the resultant dynamics behavior can be a further extension of the topic.

A coupled simulation that includes the aerodynamic effects would be a more desirable way of analyzing the dynamic response problem.

From economic views, how the improved hydrodynamic model reduces safety margin and consequently reduce offshore wind cost still remain to be investigated.

Reference

[1] Sjur Neuenkirchen Godø. Dynamic response of floating wind turbines, 2013.

[2] Bjørn Skaare, TD Hanson, R Yttervik, and FG Nielsen. Dynamic response and control of the hywind demo floating wind turbine. In *Conference Proceedings of EWEA 2011, Brussels*, 2011.

[3] European Wind Energy Association. Deep water-the next step for offshore wind energy, 2013. URL `http://www.ewea.org/fileadmin/files/library/publications/reports/Deep_Water.pdf`. [Online; accessed 12-November-2013].

[4] A MacAskill. Downwind: Marrying oil and gas expertise with offshore wind. Copenhagen, Denmark, 2005. COPENHAGEN OFFSHORE WIND 2005, Conference and Exhibition.

[5] DNV-OS-J101. Design of offshore wind turbine structure. Standard, October 2010.

[6] SIEMENS. Hywind: Siemens and statoilhydro install first floating wind turbine, 2009. URL `http://www.siemens.com/press/en/pressrelease/?press=/en/pressrelease/2009/renewable_energy/ere200906064.htm`. [Online; accessed 12-November-2013].

[7] Marilena Greco. Tmr 4215: Sea loads, 2012.

[8] RCT Rainey. *A new equation for calculating wave loads on offshore structures*. Cambridge Univ Press, 1984.

[9] Denis Matha, Markus Schlipf, Andrew Cordle, Ricardo Pereira, and Jason Jonkman. *Challenges in Simulation of Aerodynamics, Hydrodynamics, and Mooring-Line Dynamics of Floating Offshore Wind Turbines*. National Renewable Energy Laboratory, US Department of Energy, Office of Energy Efficiency and Renewable Energy, 2011.

[10] OM Faltinsen, JN Newman, and T Vinje. Nonlinear wave loads on a slender vertical cylinder. *Journal of Fluid Mechanics*, 289:179–198, 1995.

[11] J Lucas. Comparison of first and second-order hydrodynamic results for floating offshore wind structures. *GL Garrad Hassan, Report Ref: 11594br02a*, 2011.

[12] Šime Malenica and B Molin. Third-harmonic wave diffraction by a vertical cylinder. *Journal of Fluid Mechanics*, 302(1):203–229, 1995.

[13] C.T. Stansberg and O.T. Gudmestad. Non-linear random wave kinematics models verified against measurements in steep waves. *Proc. Offshore Mechanic and Arctic Engineering Conf*, I(1):15–24, 1996.

[14] RECOMMENDED PRACTICE DNV-RP-C205. Environmental conditions and environmental loads, OCTOBER 2010.

[15] CM Larsen, E Passano, et al. Fatigue life analysis of production risers. In *Offshore Technology Conference.* Offshore Technology Conference, 1987.

[16] RCT Rainey. The hydrodynamics load at the intersection of a cylinder with the water surface. In *Proceedings of 10th International Workshop on Water Waves and Floating Bodies*, pages 207–210, 1995.

[17] Enzo Marino, Claudio Borri, and Udo Peil. A fully nonlinear wave model to account for breaking wave impact loads on offshore wind turbines. *Journal of Wind Engineering and Industrial Aerodynamics*, 99(4):483–490, 2011.

[18] Per A Madsen, Russel Murray, and Ole R Sørensen. A new form of the boussinesq equations with improved linear dispersion characteristics. *Coastal engineering*, 15 (4):371–388, 1991.

[19] Arne Nestegård, Arve Johan Kalleklev, Kjell Hagatun, Yu Lin Wu, Sverre Haver, and Erik Lehn. Resonant vibrations of riser guide tubes due to wave impact. ASME, 2004.

[20] IMC Campbell and PA Weynberg. *Measurement of parameters affecting slamming.* University of Southampton, Department of Aeronautics and Astronautics, 1980.

[21] JR Chaplin, RCT Rainey, and RW Yemm. Ringing of a vertical cylinder in waves. *Journal of Fluid Mechanics*, 350:119–147, 1997.

[22] Even Rosenlund. Nonlinear hydrodynamic effects for bottom-fixed wind turbines. 2013.

[23] Per.A.Madsen. Stokes theory for weakly nolinear water waves, 10-10-2008.

[24] Klaus Hasselmann, TP Barnett, E Bouws, H Carlson, DE Cartwright, K Enke, JA Ewing, H Gienapp, DE Hasselmann, P Kruseman, et al. Measurements of wind-wave growth and swell decay during the joint north sea wave project (jonswap). 1973.

[25] J Sharma and RG Dean. Second-order directional seas and associated wave forces. In *Publication of: Offshore Technology Conference*, volume 4, 1979.

[26] HT Cuong, Armin W Troesch, and Theodore Gerald Birdsall. The generation of digital random time histories. *Ocean Engineering*, 9(6):581–588, 1982.

[27] Celso K Morooka, Irineu H Yokoo, et al. Numerical simulation and spectral analysis of irregular sea waves. In *The Fifth International Offshore and Polar Engineering Conference*. International Society of Offshore and Polar Engineers, 1995.

[28] Carl Trygve Stansberg et al. Non-gaussian extremes in numerically generated second-order random waves on deep water. In *The Eighth International Offshore and Polar Engineering Conference*. International Society of Offshore and Polar Engineers, 1998.

[29] George Z Forristall. Wave crest distributions: Observations and second-order theory. *Journal of Physical Oceanography*, 30(8):1931–1943, 2000.

[30] Carl Trygve Stansberg, Ove T Gudmestad, and Sverre K Haver. Kinematics under extreme waves. *Journal of Offshore Mechanics and Arctic Engineering*, 130(2):21010, 2008.

[31] HF Veldkamp and J Van Der Tempel. Influence of wave modelling on the prediction of fatigue for offshore wind turbines. *Wind Energy*, 8(1):49–65, 2005.

[32] B. Sweetman and S Winterstein. Second-order random ocean waves: Prediction of temporal and spatial variation from fixed and moving references: The wavemaker routine. In *Tech. Rep. RMS-37*. Civil Enigneering Departmetn, Standford University, May,1999.

[33] Michael S Longuet-Higgins and RW Stewart. Radiation stresses in water waves; a physical discussion, with applications. In *Deep Sea Research and Oceanographic Abstracts*, volume 11, pages 529–562. Elsevier, 1964.

[34] Odd Faltinsen. *Sea loads on ships and offshore structures*, volume 1. Cambridge university press, 1993.

[35] IJ Fylling, CM Larsen, N Sødahl, H Ormberg, A Engseth, E Passano, and K Holthe. Riflex–theory manual. *SINTEF report no. STF70 F*, 95219:53, 1995.

[36] Mirza M Irfan Baig and Thomas Grätsch. Recommendations for practical use of numerical methods in linear and nonlinear dynamics.

[37] S Haver and KA Nyhus. A wave climate description for long term response calculations. In *Proc., 5th OMAE Symp., ASME, IV*, volume 27, page 34, 1986.

[38] mathworks, 2014. URL `http://www.mathworks.se/help/stats/generalized-extreme-value-distribution.html`. [Online; accessed 14-May-2014].

[39] SR Winterstein, TC Ude, CA Cornell, P Bjerager, and S Haver. Environmental parameters for extreme response: Inverse form with omission factors. In *Proc. 6th Int. Conf. on Structural Safety and Reliability, Innsbruck, Austria*, 1993.

[40] Hans Homb. Fatigue analysis of mooring lines on the floating wind turbine hywind demo. 2013.

[41] Adam Nieslony. URL `http://www.mathworks.com/matlabcentral/fileexchange/3026-rainflow-counting-algorithm`. [Online; accessed June-2014].

[42] Mari Aarrestad Bekkeheien. Higher order loads from steep waves on floating wind turbines.

Appendix A

Hywind Model

The structural properties used here comes from GodøNeuenkirchen Godø [1], who did a reliability based analysis of long term prediction for dynamic response of hywind. The complete structure are subdivided into two parts, mooring lines and towers.

Mooring lines

Mooring lines are modelled as bar element, and considers axial force only. Structural properties of the mooring lines are presented in table A.1.

Hywind Demo is moored with three lines, and each can be divided into three parts, one main mooring line, and two delta lines. The three mooring lines are identical and are modelled with the same line type. Figure 4.1 and figure 4.2 show the configuration of the mooring system and the components of each mooring line respectively.

Table A.1: *Mooring line structural properties*

	Mass coefficient [kg/m]	External Axial Area [m^2]	Stiffness [N]	Quadratic Drag [-]	Diameter [m]	Added Mass [-]
Bottom chain	126	0.02	5.45E+08	1.273	0.152	1
Rope	32	0.01	6.10E+08	1.000	0.078	1
Link Chain	127	0.02	5.45E+08	1.273	0.152	1
Clump Weight	66640	19.83	5.45E+08	1.000	5.000	1
Link Chain	126	0.02	5.45E+08	1.273	0.152	1
Rope	32	0.01	6.10E+08	1.000	0.078	1
Delta Line	139	0.02	5.44E+08	1.273	0.152	1

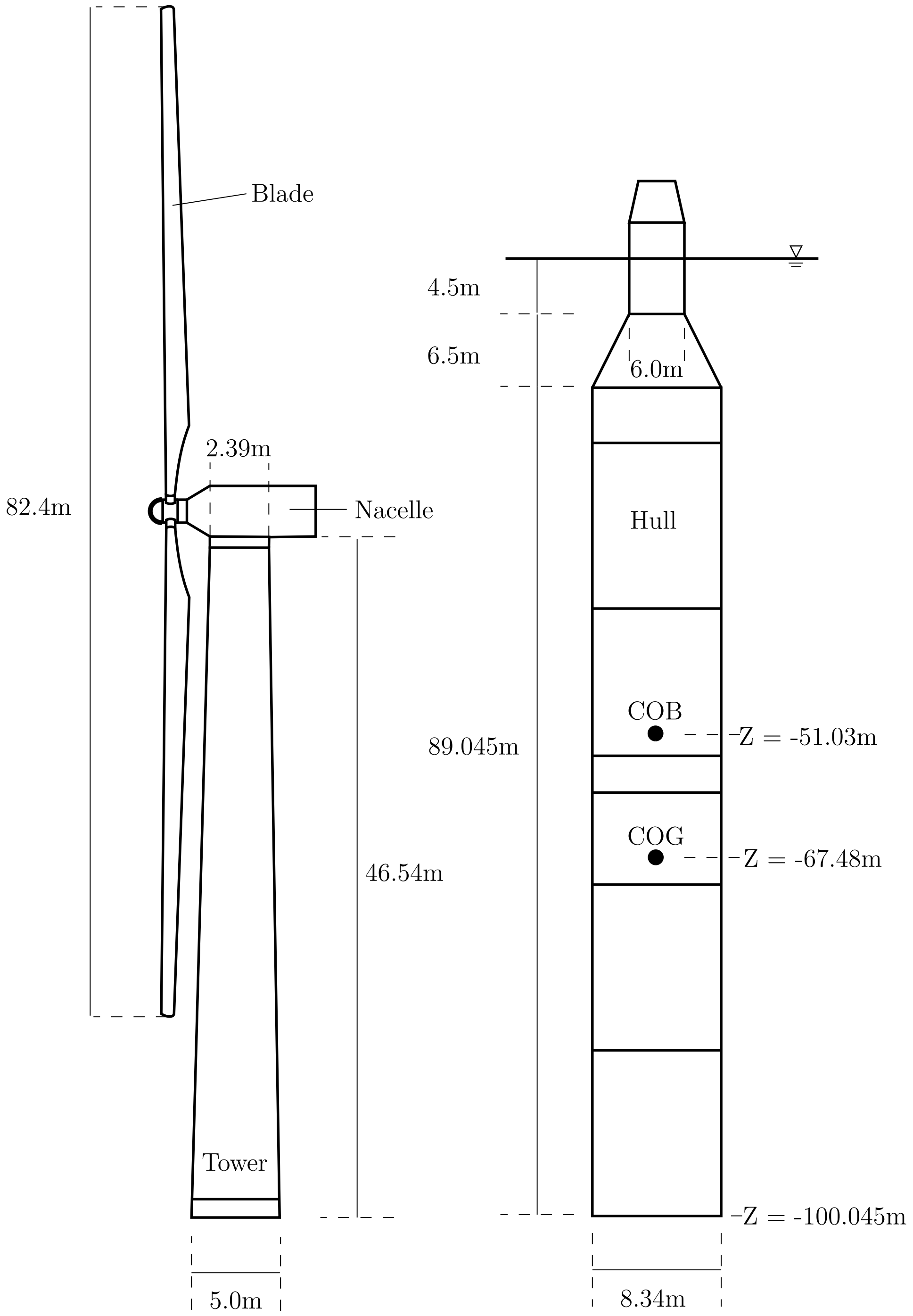
Blade
82.4m
2.39m
Nacelle
46.54m
Tower
5.0m
4.5m
6.5m
6.0m
Hull
COB
Z = -51.03m
89.045m
COG
Z = -67.48m
Z = -100.045m
8.34m

Figure A.1: *Structural drawing of Hywind Demo [1]*

Hull and tower

The hull and the tower are relatively long, which makes it possible to model it in RIFLEX in a similar way as a flexiable riser. The hull and tower is modelled with two lines, with line 1 covering from the keel to the fairlead of the mooring lines, and line 2, models the remaining parts, i.e. from z = -53 to z = 65. Table A.2 shows a summarized structure properties of the cylinder hull. Beam-type cross sections with varying geometries and stiffness defines the cylinder with varying structural properties along the hull.

Table A.2: *Structural properties of cylinder hull and turbine tower*

	segment no [-]	mass coefficient $[ton/m]$	external area $[m^2]$	gyration radius $[m]$
line 1	16	9.75-16.2	54.6	1.62-5.08
line 2	52	0.9-43.3	4.49-54.6	1.20-6.00

	axial stiff $[N]$	bending stiffness $[Nm^2]$	shear stiffness $[N]$	torsional stiffness $[Nm^2/rad]$
line 1	2.08e+11	1.19e+12		8.97e+11
	2.73e+11	2.35e+12		1.17e+12
line 2	2.49e+7	1.98e+7		9.89e+6
	5.86 e+11	2.35e+9		1.17e+9

Appendix B

Matlab Scripts

B.1 Non-linear Load calculation

```
%%%Main

close all
clear all
clc

%load 'ContourLine.mat'
%Tp=15;
%Hs=13.9;

Tp=[8,9,9,10,10];
Hs=[3.25,5,5.5,6.0,7.5];


g=9.81;
h=20;                 %water depth=20m
cf=3*1./Tp;           %cut off frequency/ sample frequency
f_sp=30*1./Tp;        %sampling frequency
Hm0=Hs;
df=1/(100);

gamma=3.3;
sigma_a=0.07;
sigma_b=0.09;


m=length(Hs);         %sea state number
n=1;                  %seeds number
U=cell(m+1,1);
U(1,:)={'F'};

tic
```

```
for k=1:1
    [~,~,~,~,F]=SecondOrderWave(Hm0(k),Tp(k),cf(k),df,gamma,sigma_a,sigma_b,f_sp(k),n,g,h);
    U(k+1,:)={F};
end
toc

%save('Forces_30min_48Seed_4seaState0527.mat','U')
```

```
function ...
    [U1,U2,loc,WaveP,F]=SecondOrderWave(Hm0,Tp,cf,df,gamma,sigma_a,sigma_b,f_sp,p,g,h)

%% wave paramters%%
[Nfreq_1,Nfreq,~,An,Omega,K]=waveparameters(Hm0,Tp,df,gamma,sigma_a,sigma_b,cf,f_sp,g,h);
K(1)=1*10^-15;

%% second order coefficients%%
[k_sum,k_dif,D_sum,D_dif,B_sum,B_dif,Omega_sum,Omega_dif]=second_tranfunction(Omega,Nfreq_1,

b=An*g./Omega;   %array
b(isnan(b))=0;
A=An'*An;
B=b'*b;
t=(0:1:Nfreq-1)*1/f_sp;
t1=(0:2*Nfreq-2)*1/f_sp/2;
t2=(0:Nfreq-2)*1/f_sp;

U1=cell(p+1,6);
U2=cell(p+1,7);
loc=cell(p+1,6);
F=cell(p+1,12);
U1(1,:)={'u1','w1','u1dx','u1dz','w1dz','u1dt'};
U2(1,:)={'u2','w2','u2dt','u2dx','u2dz','w2dz','u2_eta'};
loc(1,:)={'z','Eta','Eta2','Eta2_dx','Phi','z_eta'};
F(1,:)={'F1','M1','F10','M10','F1_streched','M1_streched','FR10','MR10','FR10s','MR10s','FR2

for q=1:p

%% first order elevation
PHI=2*pi*rand(1,Nfreq);
Phi=PHI(1:Nfreq_1);

X=An.*exp(-1i*Phi);
X_dx=-K.*X;

Y=ifft([X,(Nfreq_1+1:Nfreq)*0],Nfreq)*Nfreq; ...
                                  %expand to Nfrq terms by adding 0s
Y_dx=ifft([X_dx,(Nfreq_1+1:Nfreq)*0],Nfreq)*Nfreq; ...
                            %expand to Nfrq terms by adding 0s
Eta=real(Y);
Eta_dx=imag(Y_dx);

%% first order kinematics
dz1=-0.01;
z1=0:dz1:min(Eta);
dz2=-0.1;
z2=min(Eta)+dz1:dz2:-h;
```

```
Z=[z1,z2];
len1=length(Z);

[u1,w1,u1dx,u1dz,w1dz,u1dt,u1_dz,udt_dz,udx_dz,w1_dz]=first_kinematics(Phi,Omega,An,t,Nfreq,

%% second order elevation
phi_sum=zeros(Nfreq_1,Nfreq_1);
phi_dif=zeros(Nfreq_1,Nfreq_1);

for m=1:Nfreq_1
    phi_sum(m,:)=Phi(m)+Phi(:);
    phi_dif(m,:)=Phi(m)-Phi(:);
end

Xmn_sum=A.*B_sum.*exp(-1i*phi_sum);
Xmn_dif=A.*B_dif.*exp(-1i*phi_dif);

Xmn_sum_dx=-k_sum.*Xmn_sum;
Xmn_dif_dx=-k_sum.*Xmn_dif;

Y_eta2_sum=zeros(1,2*Nfreq-1);
Y_eta2_sum_dx=zeros(1,2*Nfreq-1);


Xmn_sum1=fliplr(Xmn_sum);
Xmn_sum1_dx=fliplr(Xmn_sum_dx);

for i=1:2*Nfreq_1-1
    X=diag(Xmn_sum1,-i+Nfreq_1);
    X_dx=diag(Xmn_sum1_dx,-i+Nfreq_1);
    Y_eta2_sum(i)=sum(X);
    Y_eta2_sum_dx(i)=sum(X_dx);
end

Xmn_dif1=Xmn_dif;
Xmn_dif1_dx=Xmn_dif_dx;

Y_eta2_dif=zeros(1,Nfreq);
Y_eta2_dif_dx=zeros(1,Nfreq);


for i=1:Nfreq_1
    X=diag(Xmn_dif1,-i+1);
    X_dx=diag(Xmn_dif1_dx,-i+1);

    Y_eta2_dif(i)=2*sum(X);
    Y_eta2_dif_dx(i)=2*sum(X_dx);
end

Y_sum=ifft(Y_eta2_sum,2*Nfreq-1)*(2*Nfreq-1);
Y_sum_dx=ifft(Y_eta2_sum_dx,2*Nfreq-1)*(2*Nfreq-1);
Elv2_sum=real(Y_sum);
Elv2_sum_dx=imag(Y_sum_dx);


Y_dif=ifft(Y_eta2_dif,Nfreq-1)*(Nfreq-1);
Y_dif_dx=ifft(Y_eta2_dif_dx,Nfreq-1)*(Nfreq-1);

```

```
Elv2_dif=real(Y_dif);
Elv2_dif_dx=real(Y_dif_dx);



Eta2=Eta(1:end-1)+Elv2_sum(1:2:end-1)+Elv2_dif;
Eta2_dx=Eta_dx(1:end-1)+Elv2_sum_dx(1:2:end-1)+Elv2_dif_dx;

[u2_sum1,u2dt_sum1,u2dx_sum1,u2dz_sum1,w2dz_sum1,u2_dif1,u2dt_dif1,u2dx_dif1,u2dz_dif1,w2_su

%% combine all the components
%%cut the time series to the same length%%
len2=length(t2);      %second order time steps in total
u2_sum1(:,len2+1:end)=[];
w2_sum1(:,len2+1:end)=[];
u2dt_sum1(:,len2+1:end)=[];
u2dx_sum1(:,len2+1:end)=[];
u2dz_sum1(:,len2+1:end)=[];
w2dz_sum1(:,len2+1:end)=[];

u1(:,len2+1:end)=[];  %first oder
w1(:,len2+1:end)=[];
u1dt(:,len2+1:end)=[];
u1dx(:,len2+1:end)=[];
u1dz(:,len2+1:end)=[];
w1dz(:,len2+1:end)=[];

u1_dz(:,len2+1:end)=[];
udt_dz(:,len2+1:end)=[];
udx_dz(:,len2+1:end)=[];
w1_dz(:,len2+1:end)=[];

%%sum of first order comp and second order correction

u2_1=u1+u2_sum1+u2_dif1;
w2_1=w1+w2_sum1+w2_dif1;

udt_1=u1dt+u2dt_sum1+u2dt_dif1;
udx_1=u1dx+u2dx_sum1+u2dx_dif1;
udz_1=u1dz+u2dz_sum1+u2dz_dif1;
wdz_1=w1dz+w2dz_sum1+w2dz_dif1;

%%wave kinematics for particles above zero
Eta_max=max(Eta);
z3=Eta_max-dz1:dz1:0.1;
len3=length(z3);
U0=zeros(len3,len2);
W0=zeros(len3,len2);
Udt0=zeros(len3,len2);
Udx0=zeros(len3,len2);
Udz0=zeros(len3,len2);
Wdz0=zeros(len3,len2);

for i=1:len3
    U0(i,:)=u2_1(1,:);
    W0(i,:)=w2_1(1,:);

    Udt0(i,:)=udt_1(1,:);
    Udx0(i,:)=udx_1(1,:);
    Udz0(i,:)=udz_1(1,:);
    Wdz0(i,:)=wdz_1(1,:);
end

u2_2=U0+z3'*u1_dz;
w2_2=W0+z3'*w1_dz;
u2dt_2=Udx0+z3'*udt_dz;
u2dx_2=Udz0+z3'*udx_dz;
u2dz_2=repmat(u1_dz,len3,1);
w2dz_2=repmat(w1_dz,len3,1);

u2=[u2_2;u2_1];
w2=[w2_2;w2_1];
u2dt=[u2dt_2;udt_1];
u2dx=[u2dx_2;udx_1];
u2dz=[u2dz_2;udz_1];
w2dz=[w2dz_2;wdz_1];


z=[z3,Z];

u2_eta=zeros(1,Nfreq-1);
z_eta=zeros(1,Nfreq-1);
%%clear the kinematic terms for z under water surface
for i=1:Nfreq-1
    if Eta(i)>0
        j=floor((-Eta_max+Eta(i))/dz1);         %%NB
    else
        j=length(z3);
    end
    u2_eta(i)=u2(j+1,i);
    z_eta(i)=Eta(i);
    u2(1:j,i)=0;
    w2(1:j,i)=0;
    u2dt(1:j,i)=0;
    u2dx(1:j,i)=0;
    u2dz(1:j,i)=0;
    w2dz(1:j,i)=0;
end


U1(q+1,:)={u1,w1,u1dx,u1dz,w1dz,u1dt};          %6
U2(q+1,:)={u2,w2,u2dt,u2dx,u2dz,w2dz,u2_eta};   %7
loc(q+1,:)={z,Eta,Eta2,Eta2_dx,Phi,z_eta};      %5
[F1,M1,F10,M10,F1_streched,M1_streched,FR10,MR10,FR10s,MR10s,FR2,MR2]=load_calculation_check
F(q+1,:)={F1,M1,F10,M10,F1_streched,M1_streched,FR10,MR10,FR10s,MR10s,FR2,MR2};
end

WaveP={K,Omega,An,Nfreq,Nfreq_1,t,t1,t2};       %7
%save('WaveKinematics.mat','U1','U2')
%%%%%%%%%%%%%%%%%%%%%%%%%%%%%%%%%%%%%%%%%%%%%%%%%%%%%%%%%%%%%%%%%%%%%%%%%%%%%
```

```
function[u1,w1,u1dx,u1dz,w1dz,u1dt,u1_dz,udt_dz,udx_dz,w1_dz]=first_kinematics(Phi,Omega,An,

%%first order values
```

```
len1=size(Z,1);

U11=Omega.*An.*exp(-1i*Phi);
Ud11=Omega.^2.*An.*exp(-1i*Phi);
u1=zeros(len1,length(t));
w1=zeros(len1,length(t));

u1dt=zeros(len1,length(t));  %dt
u1dx=zeros(len1,length(t));  %dx
u1dz=zeros(len1,length(t));  %du/dz
w1dz=zeros(len1,length(t));  %dw/dz

U1=zeros(1,Nfreq_1);
W1=zeros(1,Nfreq_1);

U1dx=zeros(1,Nfreq_1);    %dU/dx
U1dz=zeros(1,Nfreq_1);    %dU/dz
W1dz=zeros(1,Nfreq_1);    %dQ/dz

U1dt=zeros(1,Nfreq_1);

%%first order kinematics
for i=1:len1
    U1(1:Nfreq_1)=U11(1:Nfreq_1).*cosh(K(1:Nfreq_1)*(Z(i)+h))./sinh(K(1:Nfreq_1)*h); ...
             %real part
    W1(1:Nfreq_1)=U11(1:Nfreq_1).*sinh(K(1:Nfreq_1)*(Z(i)+h))./sinh(K(1:Nfreq_1)*h); ...
             %imga part

    U1(isnan(U1))=0;
    W1(isnan(W1))=0;

    U1dx(1:Nfreq_1)=K(1:Nfreq_1).*U11(1:Nfreq_1).*cosh(K(1:Nfreq_1)*(Z(i)+h))./sinh(K(1:Nfr
         %imagine part
    U1dz(1:Nfreq_1)=K(1:Nfreq_1).*U11(1:Nfreq_1).*sinh(K(1:Nfreq_1)*(Z(i)+h))./sinh(K(1:Nfr
         %real part
    W1dz(1:Nfreq_1)=K(1:Nfreq_1).*U11(1:Nfreq_1).*cosh(K(1:Nfreq_1)*(Z(i)+h))./sinh(K(1:Nfr
         %imagine part
    U1dt(1:Nfreq_1)=-Ud11(1:Nfreq_1).*cosh(K(1:Nfreq_1)*(Z(i)+h))./sinh(K(1:Nfreq_1)*h);

    U1dx(isnan(U1dx)) = 0;
    U1dz(isnan(U1dz)) = 0;
    W1dz(isnan(W1dz)) = 0;
    U1dt(isnan(U1dt)) = 0;

    u1(i,:)=real(ifft([U1,(Nfreq_1+1:Nfreq)*0],Nfreq)*Nfreq);
    w1(i,:)=imag(ifft([W1,(Nfreq_1+1:Nfreq)*0],Nfreq)*Nfreq);

    u1dx(i,:)=imag(ifft([U1dx,(Nfreq_1+1:Nfreq)*0],Nfreq)*Nfreq);
    u1dz(i,:)=real(ifft([U1dz,(Nfreq_1+1:Nfreq)*0],Nfreq)*Nfreq);
    w1dz(i,:)=imag(ifft([W1dz,(Nfreq_1+1:Nfreq)*0],Nfreq)*Nfreq);
    u1dt(i,:)=imag(ifft([U1dt,(Nfreq_1+1:Nfreq)*0],Nfreq)*Nfreq);
end


%slope at Z=0
U1_dz=Omega.*An.*K.*exp(-1i*Phi);
U1_dz(isnan(U1_dz))=0;
```

```
u1_dz=real(ifft([U1_dz,(Nfreq_1+1:Nfreq)*0],Nfreq)*Nfreq);  %first ...
    order dirivation to Z at Z=0

Udt_dz=-Omega.^2.*An.*K.*exp(-1i*Phi);
Udt_dz(isnan(Udt_dz))=0;
udt_dz=imag(ifft([Udt_dz,(Nfreq_1+1:Nfreq)*0],Nfreq)*Nfreq);  %first ...
    order dirivation to Z at Z=0

Udx_dz=K.^2.*Omega.*An.*exp(-1i*Phi);   %sin
Udx_dz(isnan(Udx_dz))=0;
udx_dz=imag(ifft([Udx_dz,(Nfreq_1+1:Nfreq)*0],Nfreq)*Nfreq);  %first ...
    order dirivation to Z at Z=0

W1_dz=Omega.*An.*K.*exp(-1i*Phi).*cosh(K*h)./sinh(K*h);
W1_dz(isnan(W1_dz))=0;
w1_dz=imag(ifft([W1_dz,(Nfreq_1+1:Nfreq)*0],Nfreq)*Nfreq);  %first ...
    order dirivation to Z at Z=0
```

```
function[u2_sum1,u2dt_sum1,u2dx_sum1,u2dz_sum1,w2dz_sum1,u2_dif1,u2dt_dif1,u2dx_dif1,u2dz_di

Z_sum=zeros(Nfreq_1,Nfreq_1);
Z_dif=zeros(Nfreq_1,Nfreq_1);

ZW_sum=zeros(Nfreq_1,Nfreq_1);
ZW_dif=zeros(Nfreq_1,Nfreq_1);

SGN1=ones(Nfreq_1,Nfreq_1);
SGN2=-ones(Nfreq_1,Nfreq_1);
SGN=triu(SGN2,0)+tril(SGN1,0);

u2_sum=zeros(len1,length(t1));
u2_dif=zeros(len1,length(t2));

w2_sum=zeros(len1,length(t1));
w2_dif=zeros(len1,length(t2));

u2dt_sum=zeros(len1,length(t1));
u2dt_dif=zeros(len1,length(t2));

u2dx_sum=zeros(len1,length(t1));
u2dx_dif=zeros(len1,length(t2));

u2dz_sum=zeros(len1,length(t1));
u2dz_dif=zeros(len1,length(t2));

w2dz_sum=zeros(len1,length(t1));
w2dz_dif=zeros(len1,length(t2));

%v and a at varisous vertical level
for i=1:len1
    Z_sum(1:Nfreq_1,1:Nfreq_1)=1/4.*B(1:Nfreq_1,1:Nfreq_1).*cosh(k_sum(1:Nfreq_1,1:Nfreq_1)
    Z_dif(1:Nfreq_1,1:Nfreq_1)=1/4.*B(1:Nfreq_1,1:Nfreq_1).*cosh(k_dif(1:Nfreq_1,1:Nfreq_1)

    ZW_sum(1:Nfreq_1,1:Nfreq_1)=1/4.*B(1:Nfreq_1,1:Nfreq_1).*sinh(k_sum(1:Nfreq_1,1:Nfreq_1)
    ZW_dif(1:Nfreq_1,1:Nfreq_1)=1/4.*B(1:Nfreq_1,1:Nfreq_1).*sinh(k_dif(1:Nfreq_1,1:Nfreq_1)

    Z_dif(1,:)=0;
    Z_dif(:,1)=0;
    Z_dif(isnan(Z_dif))=0;

    Z_sum(1,:)=0;
    Z_sum(:,1)=0;
    Z_sum(isnan(Z_sum))=0;


    ZW_dif(1,:)=0;
    ZW_dif(:,1)=0;
    ZW_dif(isnan(ZW_dif))=0;

    ZW_sum(1,:)=0;
    ZW_sum(:,1)=0;
    ZW_sum(isnan(ZW_sum))=0;

    U_sum=Z_sum.*exp(-1i*phi_sum);    %velocity u
    U_dif=Z_dif.*exp(-1i*phi_dif);

    W_sum=ZW_sum.*exp(-1i*phi_sum);    %velocity u
    W_dif=ZW_dif.*exp(-1i*phi_dif);
    W_dif(isnan(W_dif))=0;


    U_sum2=Z_sum.*exp(-1i*phi_sum);    %velocity u
    U_dif2=Z_dif.*exp(-1i*phi_dif);

    Udt_sum=-(Omega_sum).*U_sum;       %acceleration du/dt
    Udt_dif=-(Omega_dif).*U_dif;

    Udx_sum=k_sum.*U_sum;       %du/dx
    Udx_dif=k_dif.*U_dif;

    Udz_sum=k_sum.*U_sum2;      %du/dz
    Udz_dif=k_dif.*U_dif2;

    %remains to check the solutuion...
    Wdz_sum=k_sum.*W_sum;      %dw/dz
    Wdz_dif=k_dif.*W_dif;

    U_dif=U_dif.*SGN;
    W_dif=W_dif.*SGN;
    Udt_dif=Udt_dif.*SGN;
    Udx_dif=Udx_dif.*SGN;
    Udz_dif=Udz_dif.*SGN;
    Wdz_dif=Wdz_dif.*SGN;


    U_dif(logical(eye(size(U_dif))))=0;
    W_dif(logical(eye(size(W_dif))))=0;
    Udt_dif(logical(eye(size(Udt_dif))))=0;
    Udx_dif(logical(eye(size(Udx_dif))))=0;
    Udz_dif(logical(eye(size(Udz_dif))))=0;
    Wdz_dif(logical(eye(size(Wdz_dif))))=0;


    %%ifft
    UU_sum=zeros(1,2*Nfreq-1);
    WW_sum=zeros(1,2*Nfreq-1);
    UUdt_sum=zeros(1,2*Nfreq-1);
    UUdx_sum=zeros(1,2*Nfreq-1);
    UUdz_sum=zeros(1,2*Nfreq-1);
    WWdz_sum=zeros(1,2*Nfreq-1);


    U_sum1=fliplr(U_sum);
    W_sum1=fliplr(W_sum);
    Udt_sum1=fliplr(Udt_sum);
    Udx_sum1=fliplr(Udx_sum);
    Udz_sum1=fliplr(Udz_sum);
    Wdz_sum1=fliplr(Wdz_sum);


    for j=1:2*Nfreq_1-1
        X1=diag(U_sum1,-j+Nfreq_1);
        X2=diag(Udt_sum1,-j+Nfreq_1);
        X3=diag(Udx_sum1,-j+Nfreq_1);
        X4=diag(Udz_sum1,-j+Nfreq_1);
        X5=diag(Wdz_sum1,-j+Nfreq_1);
        X6=diag(W_sum1,-j+Nfreq_1);

        UU_sum(j)=sum(X1);
        UUdt_sum(j)=sum(X2);
        UUdx_sum(j)=sum(X3);
        UUdz_sum(j)=sum(X4);
        WWdz_sum(j)=sum(X5);
        WW_sum(j)=sum(X6);
    end


    UU_dif=zeros(1,Nfreq-1);
    WW_dif=zeros(1,Nfreq-1);
    UUdt_dif=zeros(1,Nfreq-1);
    UUdx_dif=zeros(1,Nfreq-1);
    UUdz_dif=zeros(1,Nfreq-1);
    WWdz_dif=zeros(1,Nfreq-1);

    for j=1:Nfreq_1
        X1=diag(U_dif,-j+1);
        X2=diag(Udt_dif,-j+1);
        X3=diag(Udx_dif,-j+1);
        X4=diag(Udz_dif,-j+1);
        X5=diag(Wdz_dif,-j+1);
        X6=diag(W_dif,-j+1);

        UU_dif(j)=2*sum(X1);
        UUdt_dif(j)=2*sum(X2);
        UUdx_dif(j)=2*sum(X3);
        UUdz_dif(j)=2*sum(X4);
        WWdz_dif(j)=2*sum(X5);
        WW_dif(j)=2*sum(X6);
    end

    u2_sum(i,:)=ifft(UU_sum,2*Nfreq-1)*(2*Nfreq-1);
    u2_dif(i,:)=ifft(UU_dif, Nfreq-1)*(Nfreq-1);

    w2_sum(i,:)=ifft(UU_sum,2*Nfreq-1)*(2*Nfreq-1);
    w2_dif(i,:)=ifft(UU_dif, Nfreq-1)*(Nfreq-1);

    u2dt_sum(i,:)=ifft(UUdt_sum,2*Nfreq-1)*(2*Nfreq-1);
    u2dt_dif(i,:)=ifft(UUdt_dif, Nfreq-1)*(Nfreq-1);

    u2dx_sum(i,:)=ifft(UUdx_sum,2*Nfreq-1)*(2*Nfreq-1);
    u2dx_dif(i,:)=ifft(UUdx_dif, Nfreq-1)*(Nfreq-1);

    u2dz_sum(i,:)=ifft(UUdz_sum,2*Nfreq-1)*(2*Nfreq-1);
    u2dz_dif(i,:)=ifft(UUdz_dif, Nfreq-1)*(Nfreq-1);

    w2dz_sum(i,:)=ifft(WWdz_sum,2*Nfreq-1)*(2*Nfreq-1);
    w2dz_dif(i,:)=ifft(WWdz_dif, Nfreq-1)*(Nfreq-1);
end


u2_sum1=real(u2_sum(:,1:2:end));
u2_dif1=real(u2_dif);

w2_sum1=imag(u2_sum(:,1:2:end));
w2_dif1=imag(u2_dif);

u2dt_sum1=imag(u2dt_sum(:,1:2:end));
u2dt_dif1=imag(u2dt_dif);

u2dx_sum1=imag(u2dx_sum(:,1:2:end));
u2dx_dif1=imag(u2dx_dif);

u2dz_sum1=real(u2dz_sum(:,1:2:end));
u2dz_dif1=real(u2dz_dif);

w2dz_sum1=imag(w2dz_sum(:,1:2:end));
w2dz_dif1=imag(w2dz_dif);
```

```
function ...
    [F1,M1,F10,M10,F1_streched,M1_streched,FR10,MR10,FR10s,MR10s,FR2,MR2]=load_calculation(u
%% LOAD CALCULATION
D=5.0;
Cm=2.0;
Cd=1.0;
rho=1.0*10^3;

%morision +second order wave kinematics
dF1=rho*pi*D.^2/4*Cm*u2dt+rho/2*Cd*D*abs(u2).*u2;
dz_1=[z(2:end),z(end)];
dz_2=[z(1),z(1:end-1)];
dz=(dz_1-dz_2)';
F1=1/2*sum(dF1.*repmat(dz,1,size(dF1,2)));

dM1=dF1.*(repmat(z',1,size(dF1,2))+h);
M1=1/2*sum(dM1.*repmat(dz,1,size(dF1,2)));

% morison +first order without streching
dF10=rho*pi*D.^2/4*Cm*u1dt+rho/2*Cd*D*abs(u1).*u1;
```

```
dZ1=[Z(2:end),Z(end)];
dZ2=[Z(1),Z(1:end-1)];
dZ=(dZ1-dZ2)';
F10=1/2*sum(dF10.*repmat(dZ,1,size(dF1,2)));
dM10=dF10.*(repmat(Z',1,size(dF1,2))+h);
M10=1/2*sum(dM10.*repmat(dZ,1,size(dF1,2)));

% morision +first order+streching
z_streched=(repmat(z',1,len2)-repmat(Eta(1:end-1),size(z',1),1))./(1+1/h*repmat(Eta(1:end-1

%EtaExp=repmat(Eta(1:end-1),size(z_streched,1),1);
%z_streched(z_streched > 0)=0;         %determine the free surface in ...
    the streched coordinate

%loc=find(z_streched>0);

dz_1streched=[z_streched(2:end,:);z_streched(end,:)];
dz_2streched=[z_streched(1,:);z_streched(1:end-1,:)];
dz_streched=(dz_1streched-dz_2streched);

[u1_streched,w1_streched,u1dx_streched,u1dz_streched,w1dz_streched,u1dt_streched,~,~,~,~]=f
dF1_streched=rho*pi*D.^2/4*Cm*u1dt_streched(:,1:end-1)+rho/2*Cd*D*abs(u1_streched(:,1:end-1
F1_streched=1/2*sum(dF1_streched.*repmat(dz,1,size(dF1,2)));
F1_streched(z_streched>0)=0;

dM1_streched=dF1_streched.*(z_streched+h);
M1_streched=1/2*sum(dM1_streched.*repmat(dz,1,size(dF1,2)));

% Rainey+first order
%[u1,w1,u1dx,u1dz,w1dz,u1dt,~,~,~,~]=first_kinematics(Phi,Omega,An,t,Nfreq,Nfreq_1,Z,K);
dFR10=(rho*pi*D^2/4)*Cm*(u1dt+u1.*u1dx+w1.*u1dz)+(Cm-1)*(rho*pi*D^2/4).*w1dz.*u1;
dFdR10=rho/2*Cd*D*abs(u1).*u1;
Fs10=-1/2*Eta2_dx.*(Cm-1)*(rho*pi*D^2/4).*u1(1,:).^2;
FR10=1/2*sum((dFR10+dFdR10).*repmat(dZ,1,size(dF1,2)))+Fs10;

Ms10=Fs10.*(h);
dM_R10=dFR10.*(repmat(Z',1,size(dF1,2))+h);
MR10=1/2*sum(dM_R10.*repmat(dZ,1,size(dF1,2)))+Ms10;

% Rainey+first order+streching
dFR10s=(rho*pi*D^2/4)*Cm*(u1dt_streched+u1_streched.*u1dx_streched+w1_streched.*u1dz_streche
dFdR10s=rho/2*Cd*D*abs(u1_streched).*u1_streched;
Fs10s=-1/2*Eta2_dx.*(Cm-1)*(rho*pi*D^2/4).*u1(1,:).^2;
FR10s=1/2*sum((dFR10s(:,1:end-1)+dFdR10s(:,1:end-1)).*repmat(dz,1,size(dF1,2)))+Fs10;

Ms1s=Fs10s.*(h);
dMR1s=dFR10s(:,1:end-1).*(repmat(dz,1,size(dF1,2))+h);
MR10s=1/2*sum(dMR1s.*dz_streched)+Ms1s;

% Rainey+second order
dFR2=(rho*pi*D^2/4)*Cm*(u2dt+u2.*u2dx+w2.*u2dz)+(Cm-1)*(rho*pi*D^2/4).*w2dz.*u2;
dFdR2=rho/2*Cd*D*abs(u2).*u2;
Fs2=-1/2*Eta2_dx.*(Cm-1)*(rho*pi*D^2/4).*u2_eta.^2;
FR2=1/2*sum((dFR2+dFdR2).*repmat(dz,1,size(dF1,2)))+Fs2;

Ms2=Fs2.*(z_eta+h);
dMR2=dFR2.*(repmat(z',1,size(dF1,2))+h);
MR2=1/2*sum(dMR2.*repmat(dz,1,size(dF1,2)))+Ms2;
```

B.2 Rossenblatt Transformation

```
clear all
clc

year=[1,20,50,100];
n=100;
m=length(year);
linetype={'r','c','b','k'};
legendInfo={'1 year','10 years','50 years','100 years'};

for i=1:m

a=1/(year(i)*365*24*2);
b=-sqrt(2) * erfinv(2*a-1); ...
                                                   %inverse normal ...
    distribution accumulated
beta=2*pi/n*(0:1:n); ...
                                                          %reliablity
u1=b*cos(beta);
u2=b*sin(beta);

phi1=normcdf(u1);
h=2.822*nthroot(-log(1-phi1),1.547);
mu=1.59+0.42*log(h+2);
sigmma=sqrt(0.005+0.085*exp(-0.14*h.^(1.34)));
phi2=normcdf(u2);
tp=exp(u2.*sigmma+mu);
grid on
plot(h,tp,linetype{i})

hold on

end

lgh=legend(legendInfo);
set(lgh,'Location','Best')
hold off
title('Hs-Tp contour line')
xlabel('Hs [m]')
ylabel('Tp [s]')

for i=3
    a=1/(year(i)*365*8);
    b=-sqrt(2) * erfinv(2*a-1); ...
                                                   %inverse normal ...
        distribution accumulated
    beta=2*pi/n*(0:1:n); ...
                                                          %reliablity
    u1=b*cos(beta);
    u2=b*sin(beta);

    phi1=normcdf(u1);
    h=2.822*nthroot(-log(1-phi1),1.547);
    mu=1.59+0.42*log(h+2);
    sigmma=sqrt(0.005+0.085*exp(-0.14*h.^(1.34)));
    phi2=normcdf(u2);
    tp=exp(u2.*sigmma+mu);
end
Hs=h(1:5:end);
Tp=tp(1:5:end);

save('ContourLine.mat','Hs','Tp')
```

Appendix C

Modal Analysis

C.1 Modal analysis

When the structure is subject to higher order loads, its elastic response, instead of the global motion is of greater interests. The higher loads, though with a lower magnitude than first order wave forces, have the potential to excite significant elastic deformation due its higher frequency.

Due to the complex geometry of Hywind Demo, it is not practical to establish a set of governing equations and solve analytically to get the exact value. Instead, numerical methods are applied to obtain a approximate value that is expected to have a satisfying accuracy. Generally, there are two numerical methods applicable, i.e. finite element methods by discretionary the structure, and modal superposition by assuming the deformation as a combination of known mode shapes. As the mode shapes are relatively convenient to calculate and requires fewer computational efforts, herein, modal superposition is utilized to analyze the dynamic characteristics of this floating wind turbine. At a later phase of the project, FEM method will be implemented as well in RIFLEX and compare with modal superposition results.

In this section, C.1.1 aims to formulate the mode shapes of the simplified model and C.1.2 works to explain the principles of modal superposition.

C.1.1 Beam model

To obtain the lowest vibration modes of this structure, a free-free beam model is applied, considering the support structure is free to move at both ends with out any forces or moments applied. Based on these concerns, the support structure of Hywind Demo is simplified as a free-free beam.

For a free-free beam, the governing equation is formulated as below in equation C.1, in which A, I, E, ρ, and γ represents the cross sectional area, the moment of inertia, the elastic modulus, material density of the structure and structural damping coefficient of the structure.

$$\rho A\ddot{w} + \gamma\dot{w} + EIw^{''''} = 0 \tag{C.1}$$

where the dots correspond to a time partial differentiation, and the primes indicates a spatial partial differentiation(i.e., $\dot{w} = \frac{\partial w}{\partial t}$ and $w^{'} = \frac{\partial w}{\partial x}$).

To solve the partial differential equation that describes the vertical deflection $w(x,t)$, a 'separation of variables' approach is employed in the analysis. The vertical displacement is assumed to be composed of the product of two functions, one which is a function of space only and the other is a function of time only, i.e.

$$w(x,t) = X(x)T(t) \tag{C.2}$$

Substituting equation C.2 into equation C.1, the governing equation can be formulated as two separate equations after some manipulations.

$$X^{''''} - \beta^4 X = 0, \beta^4 = \frac{\omega^2}{c^2}, c = \sqrt[2]{\frac{EI}{\rho A}} \tag{C.3}$$

$$\ddot{T} + \frac{\gamma L}{m}\dot{T} + \omega^2 T = 0 \tag{C.4}$$

The spatial variation of the vibration shape is of greater interest here. The general solution of the equation C.3 has the form,

$$X(x) = a_1\sin(\beta x) + a_2\cos(\beta x) + a_3\sinh(\beta x) + a_4\cosh(\beta x) \tag{C.5}$$

The four unknowns, $a_1, a_2, a_3, anda_4$, are determined by applying the four boundary conditions at the two ends, i,e, zero moments at both ends of the beam

$$EIw^{''}(0,t) = EIw^{''}(L,t) = 0 \tag{C.6}$$

and zero shear force at both ends of the beam,

$$EIw^{''''}(0,t) = EIw^{''''}(L,t) = 0 \tag{C.7}$$

With the above boundary conditions applied, the spatial variation part is obtained as,

$$X_n(x) = -a_2\left[\cosh[(\beta_n L)\frac{x}{L}] + \cos[(\beta_n L)\frac{x}{L}] - \sigma_n(\sinh[(\beta_n L)\frac{x}{L}] + \sin[(\beta_n L)\frac{x}{L}]\right] \tag{C.8}$$

where $n = 1, 2, 3, \cdots$, and $\sigma_n = \frac{\cosh(\beta_n L) - \cos(\beta_n)L}{\sinh(\beta_n L) - \sin(\beta_n L)}$.

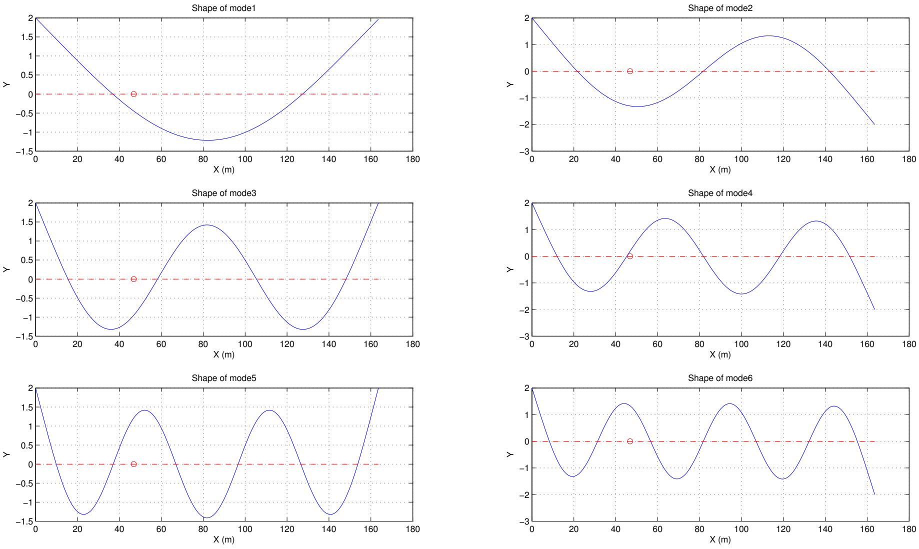

Figure C.1: Modes shape for the lowest six modes

while the value of β_n is constrained by the following characteristic equation, with the roots given in table

$$\cos(\beta L)\cosh(\beta L) = 1 \tag{C.9}$$

Table C.1: Roots of the characteristic equation for a free-free beam

Root	Value
$\beta_0 L$	0
$\beta_1 L$	4.73
$\beta_2 L$	7.85
$\beta_3 L$	10.99
$\beta_4 L$	14.13
$\beta_n L$	$(2n+1)\pi/2$

Equation C.8 describes the n*th* order elastic mode shape for this free-free beam, with the first few mode shapes shown in figure C.1. In the figure, the lowest mode, rigid body mode is not included. The x-axis in the figure represents the location from the bottom of the spar and the red dot is the anchoring point where the mooring lines are attached.

C.1.2 Modal superposition

When using modal superposition, the dynamic response is assumed as a linear combination of the natural modes of vibration, as shown in equation C.5. The basis for this method is equation C.10.

$$w(x,t) = \sum_{i=1}^{N} \psi_i(x) q_i(t) \tag{C.10}$$

where $w(x,t)$ is the combined weighted response, $\psi_i(x)$ is the shape function for the i^{th} mode and $q_i(t)$ is a time-dependent weight function for i^{th} mode. By applying the principle of virtual displacement, it is possible to rephrase the continuous system with arbitrary distributional of masses, damping and stiffness, into a simplified system with one degree of freedom by using a generalized coordinate, $q_i(t)$.

By equating the external and internal virtual work, the dynamic equations can be rephrased as:

$$\overline{m_i}\ddot{q_i} + \overline{c_i}\dot{q_i} + \overline{k_i}q_i = \overline{p_i} \tag{C.11}$$

in which,

$$\overline{m_i} = \int_0^L m(x) \left[\psi_i(x)\right]^2 dx + \sum_{j=1}^{N} M_j \left[\psi_i(x_j)\right]^2 \tag{C.12}$$

$$\overline{k_i} = \int_0^L EI(x) \left[\psi_{i,xx}(x)\right]^2 dx + \sum_{j=1}^{N} K_j \left[\psi_i(x_j)\right]^2 \tag{C.13}$$

$$\overline{c_i} = \int_0^L c(x) \left[\psi_i(x)\right]^2 dx + \sum_{j=1}^{N} C_j \left[\psi_i(x_j)\right]^2 \tag{C.14}$$

$$\overline{p_i}t = \int_0^L q(x,t)\psi_i(x)\, dx + \sum_{j=1}^{N} P_j \psi_i(x_j) \tag{C.15}$$

$\overline{m_i}$, $\overline{k_i}$, $\overline{c_i}$ and $\overline{p_i}$ are generalized mass, generalized stiffness, generalized damping and generalized load respectively. In the expressions for the generalized quantities, the integral part represent the contributions from the distributed quantities, $m(x), c(x), k(x)$, while the summation parts are the contributions from the concentrated quantities, $M_j(x_j), C_j(x_j), K_j(x_j)$ acting on the position x_j. Also, the stiffness contribution from the bending stiffness of the beam EI is also included in the expression.

While modal mass and modal stiffness are explicitly defined in chapter 1.2, the damping level is relatively more challenging to measure. For simplicity concerns, a modal damping ratio is introduced directly into the prolbem, as defined in equation C.1.2.

$$\xi_i = \frac{c_i}{c_{i,critical}} = \frac{\bar{c_i}}{2\sqrt{\bar{m_i}\bar{k_i}}} \tag{C.16}$$

When the damping level is explicitly defined, the modal damping can be calculate as,

$$\bar{c_i} = 2\xi_i\sqrt{\bar{m_i}\bar{k_i}} \tag{C.17}$$

C.2 Hywind Model

Detailed design parameters of the structure are provided in chapter 1. The complete support structure has 11 segments in total, including 2 for the wind turbine tower and the rest for the spar type hull. For numerical analysis purposes, the support structure is divided into smaller sections within each segment assigned with a node number in the modal analysis coordinates $w - o - x$, which is marked as coordinate 1 in the *Matlab* script. When dividing the segment, the general rule is applying smaller section for segments with significant geometrical variation and larger sections for segments with constant geometrical properties, such as segments at the hull bottom, see table 1.2. Due to limited knowledge on design details within each segment, all the parameters are assumed to be linearly varied, if the design parameters for segment top and bottom are not identical.

$$D_{i,k} = D_{i,bottom} + \frac{z_{i,k} - z_{i,bottom}}{z_{i,top} - z_{i,bottom}} \times D_{i,top} - D_{i,bottom} \tag{C.18}$$

where, D can be any of the design parameter, mass per unit length, wall thickness, and cylinder diameter, the suffix i denotes the segment number, k is the node number within that segment, and *top*, *bottom* represent the value at the segment top and bottom.

Coordinate system

To model the Hywind Demo, three coordinate systems are defined. Two of them are body fixed coordinate system and earth fixed coordinate system as defined in figure **??**. A third coordinate system is introduced here for elastic deformation analysis purposes, the origin is fixed at the bottom of the hull, with the centerline of the structure taken as the x axis and w pointing outwards.

Modal mass

The Hywind Demo tower and substructure consist of 11 segments in total. The mass distribution is illustrated in table 1.3 containing information on mass distribution. For the immersed part, added mass due to radiation is counted as a distributed mass along the length, which means $m(x) = m_{dis}(x) + m_{11}^{(2D)}$.

$$\overline{m_i} \;=\; \int_0^L m(x)\left[\psi_i\left(x\right)\right]^2 dx \sum_{j=1}^{N} M_j\left[\psi_i\left(x_j\right)\right]^2 \tag{C.19}$$

Since the mass distribution is not continuous, the integration is instead carried out in a numerical way. The mass distribution is defined in table chapter 2 and the modal shapes are analyzed in section C.1, with the following derived for mode shapes,

$$\psi_i(x) = -a_2\left[\cosh[(\beta_i L)\frac{x}{L}] + \cos[(\beta_i L)\frac{x}{L}] - \sigma_i(\sinh[(\beta_i L)\frac{x}{L}] + \sin[(\beta_i L)\frac{x}{L}]\right] \tag{C.20}$$

where $i = 1, 2, 3, \cdots$, and $\sigma_i = \frac{\cosh(\beta_i L) - \cos(\beta_i) L}{\sinh(\beta_i L) - \sin(\beta_i L)}$. β_i is constrained

$$\cos(\beta L) \cosh(\beta L) = 1 \tag{C.21}$$

The turbine mass and nacelle mass are treated as a lumped mass, without considering the coupling, which is added as the second part of equation C.19.

Within each segment, each section is defined with the same length for simplicity concerns. The numerical integration can be carried out in a efficient way by applying trapezoidal rule, i.e.

$$\begin{aligned} f(x) &= m(x)[\psi_i(x)]^2, && \text{(C.22)} \\ \overline{m_i} &= \int_0^L f(x) dx && \text{(C.23)} \\ &= \sum_{j=1}^{11} h_j [\frac{1}{2} f(x_1) + f(x_2) + f(x_3) + \cdots + f(x_{n-1}) + \frac{1}{2} f(x_n)] && \text{(C.24)} \end{aligned}$$

where j is the segment number, ranges from 1 to 11, and x_k denotes the coordinate of node k within the segment. h_j is the node length in segment j.

Modal stiffness

Modal stiffness can be calculated by using equation C.25.

$$\overline{k_i} = \int_0^L EI(x) \left[\psi_{i,xx}(x)\right]^2 dx + \sum_{j=1}^{N} K_j \left[\psi_i(x_j)\right]^2 \tag{C.25}$$

where the $EI(x)$ can be expressed for each node, $\psi_{i,xx}$ is the second derivative of the mode shapes.

When performing numerical integration, the trapezoidal rule is again utilized to account for the structural stiffness distributed along the cylinder. Two Young's modules are introduced for steel and concrete, $E_{steel} = 210\ GPa$ and $E_{concrete} = 30\ GPa$. The moment of inertia, I, is calculated using the equation for a circular cross section:

$$I = \frac{\pi}{4} \left[\left(\frac{D}{2} \right)^4 - \left(\frac{D}{2} - t \right)^4 \right] \tag{C.26}$$

where D is the outer diameter, and t is the wall thickness. For the moment of inertia due to blasting, the value for outer diameter and wall thickness can be equated and regarded as $\frac{D}{2} - t$. In that way, equation C.26 is applicable to calculate the contributions from blasting as well.

Mooring lines, attached at $z = -53.2\ m$ contributes to second part of equation C.25. Due to the lack of information on mooring line stiffness, it is approximated by using the surge period, since mooring line stiffness acts as the only contribution to the storing force in surge.

$$k_{mr} = (m11 + m)(\frac{2\pi}{T_{11}})^2 \tag{C.27}$$

Eigenfrequency

One of the most important part of the modal analysis is to achieve the correct value of of the lowest egiengfrequencies. With modal and modal stiffness calculated for each mode, the eigenfrequencies for the lowest six modes are shown in table C.2,

$$\omega_i = \sqrt{\frac{k_i}{m_i}} \tag{C.28}$$

Table C.2: *Eigenfrequencies for the lowest six modes*

Mode	**Value [rad/s]**
0	0
1	4.26
2	17.38
3	32.19
4	55.06
5	77.67
6	129.91

According to Bekkeheien[42], the eigenfrequency for mode 55 can be regarded as the lowest eigenfrequency of the structure, which is $\omega_n = 4.5429\ rad/s$. The calculated value is 6.17% lower than the provided value. The error might be introduced in two aspects, the modeling and the mode shape. For the modeling part, the diameter and wall thickness distribution is based on the assumption of linearly distribution among each segment, which affects the structural stiffness distribution and the resultant modal mass of each mode. Second, the mass distribution is also assumed to be constant unit value over the segment, which might lead to a error. Thirdly, the 2D added mass, which is taken as $m_{11}^{2D} = \rho\pi D^2/4$, might be different from the analysis by Statoil. Besides, the accuracy of the modal analysis largely depends on the modal shapes assumed and the boundary conditions applied in analysis. In the analysis, a free-free beam is assumed, which is of doubt due the mooring line connection and the heavy mass at the top of the structure. Compared with the value $\omega = 58.7\ rad/s$ calculate by Bekkeheinen, the value obtained here is more compatibly closer to the real value. The much too large k/m ratio in Bekkeheinen might be caused by ignoring modal mass contributions from hydrodynamic added mass(resulted in a small m), or mistakenly used the same Young's modulus for the blasting as steel(led to a large k).

Appendix D

Mooring line dynamics

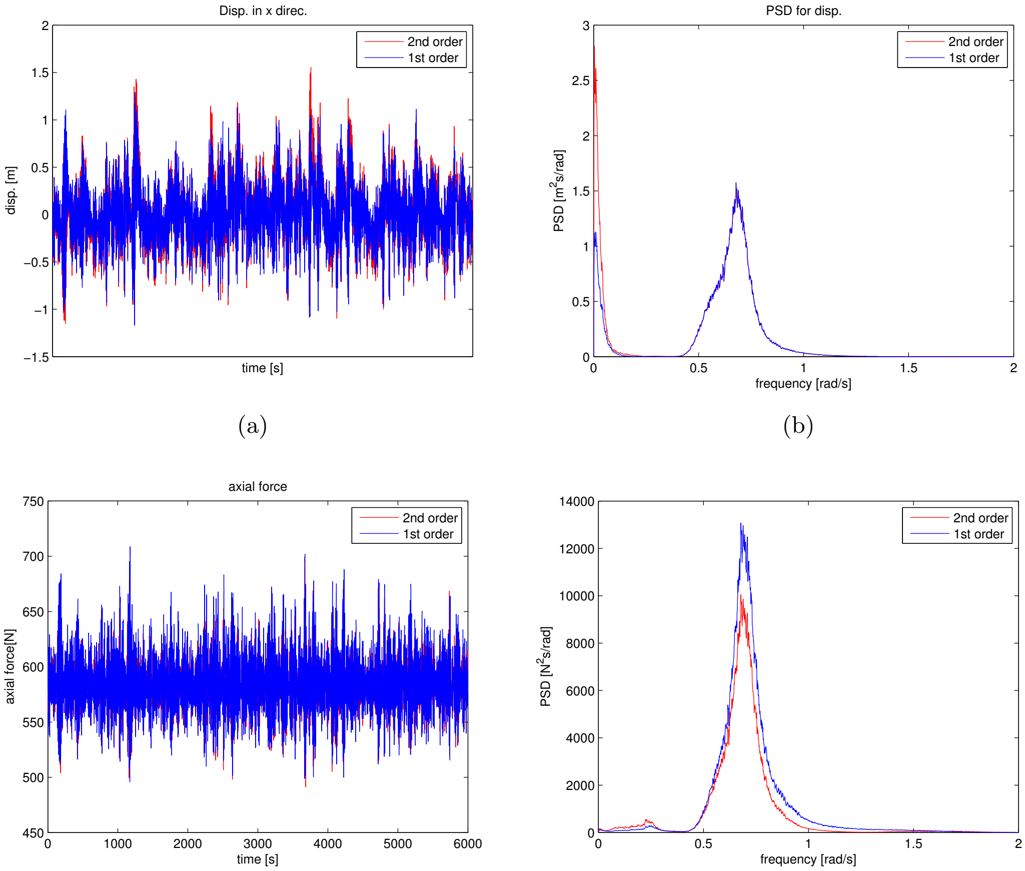

(a) (b)

(c) (d)

Figure D.1: *Maixmum value of dynamic response on main mooring line 9,* $H_s = 6\ m, T_p = 12\ s$

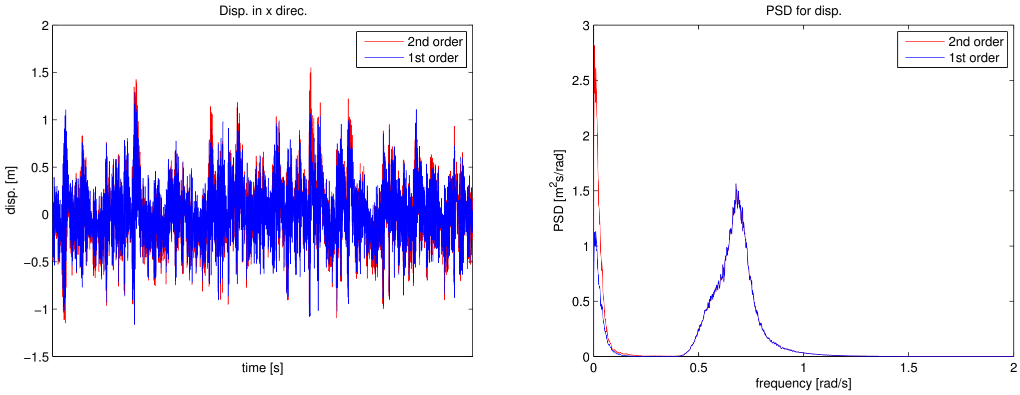

(a)

(b) $z = -50\ m$

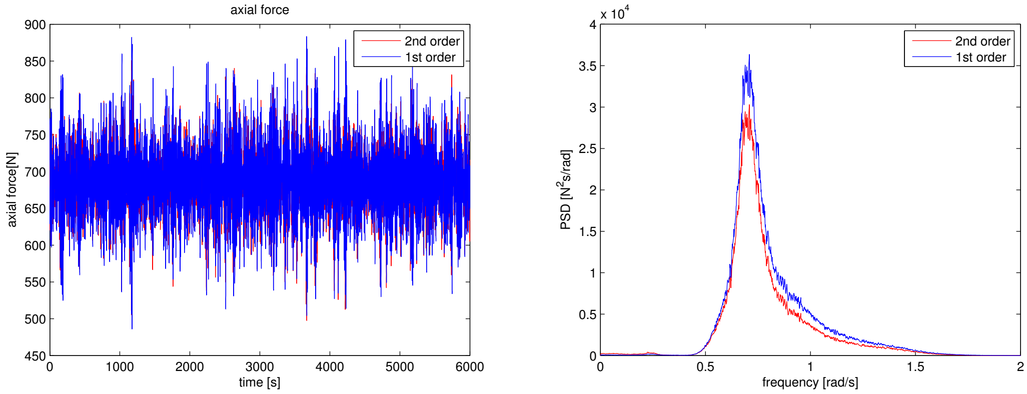

(c)

(d) $z = -50\ m$

Figure D.2: *Maixmum value of dynamic response on main mooring line 9,* $H_s = 6\ m, T_p = 12\ s$

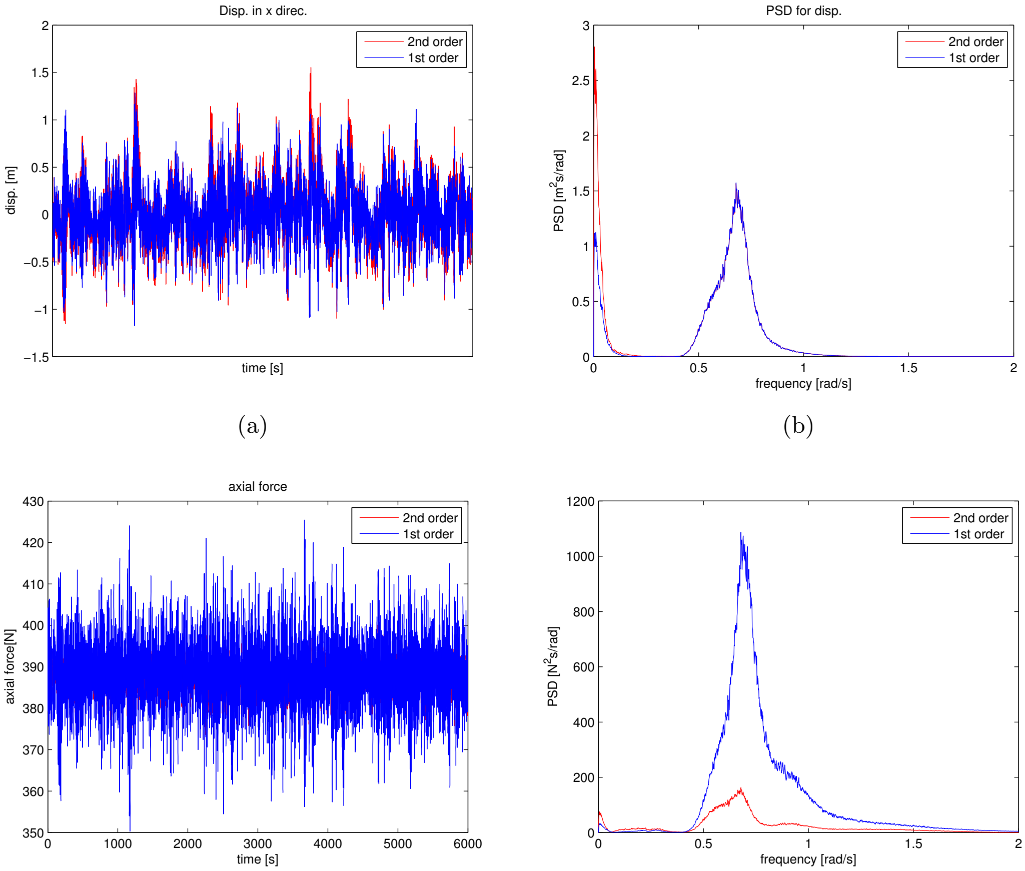

(a) (b)

(c) (d)

Figure D.3: *Maixmum value of dynamic response on main mooring line 9,* $H_s = 6\ m, T_p = 12\ s$

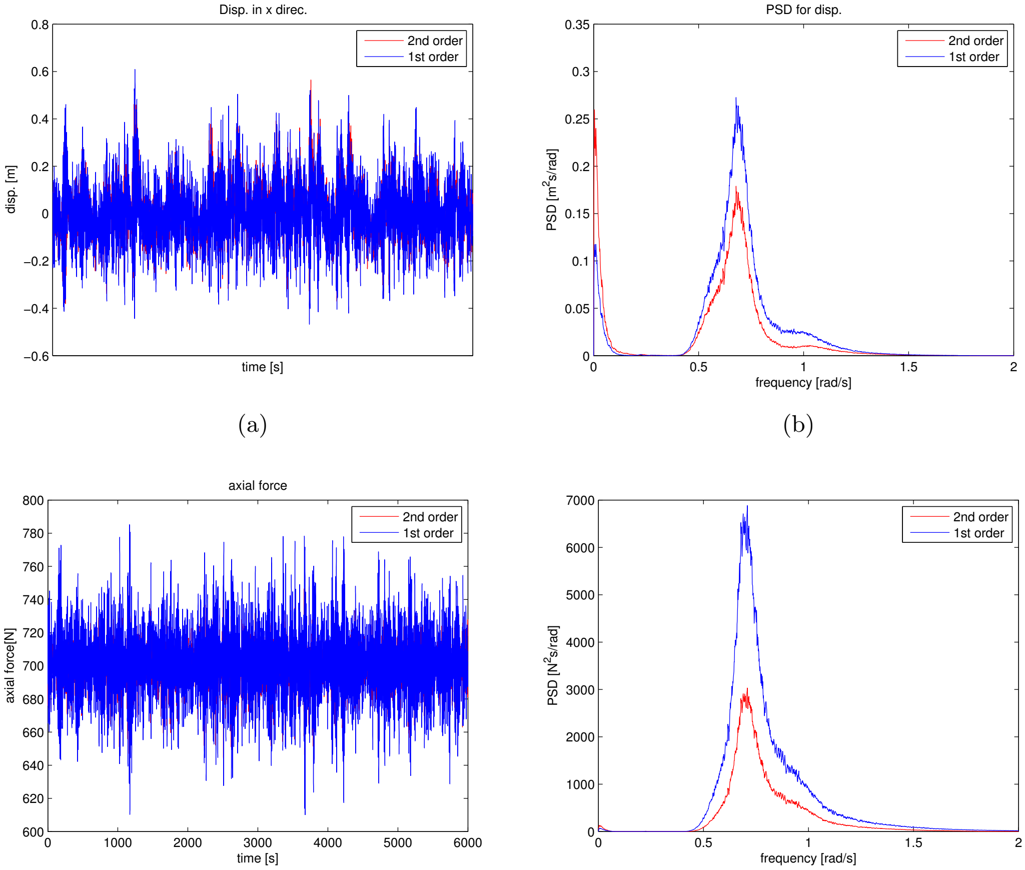

(a) (b)

(c) (d)

Figure D.4: *Maixmum value of dynamic response on main mooring line 9,* $H_s = 6\ m, T_p = 12\ s$

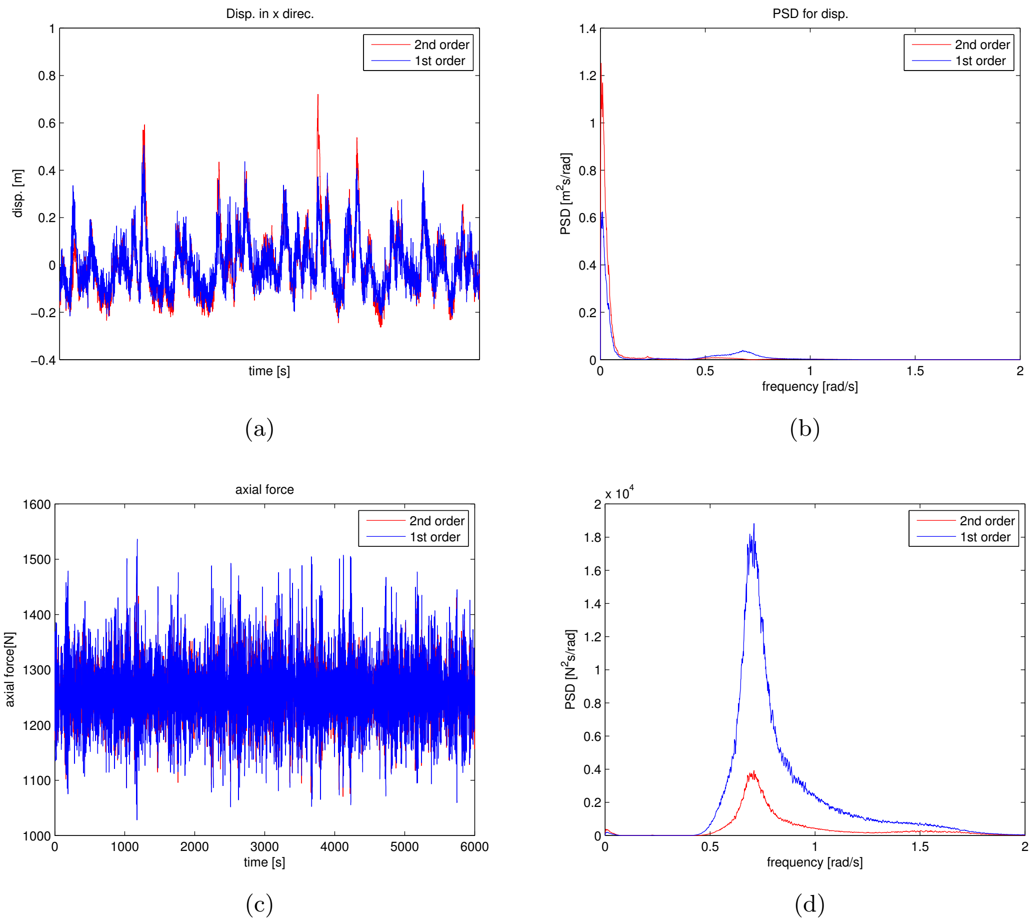

(a) (b)

(c) (d)

Figure D.5: *Maixmum value of dynamic response on main mooring line 9,* $H_s = 6\ m, T_p = 12\ s$

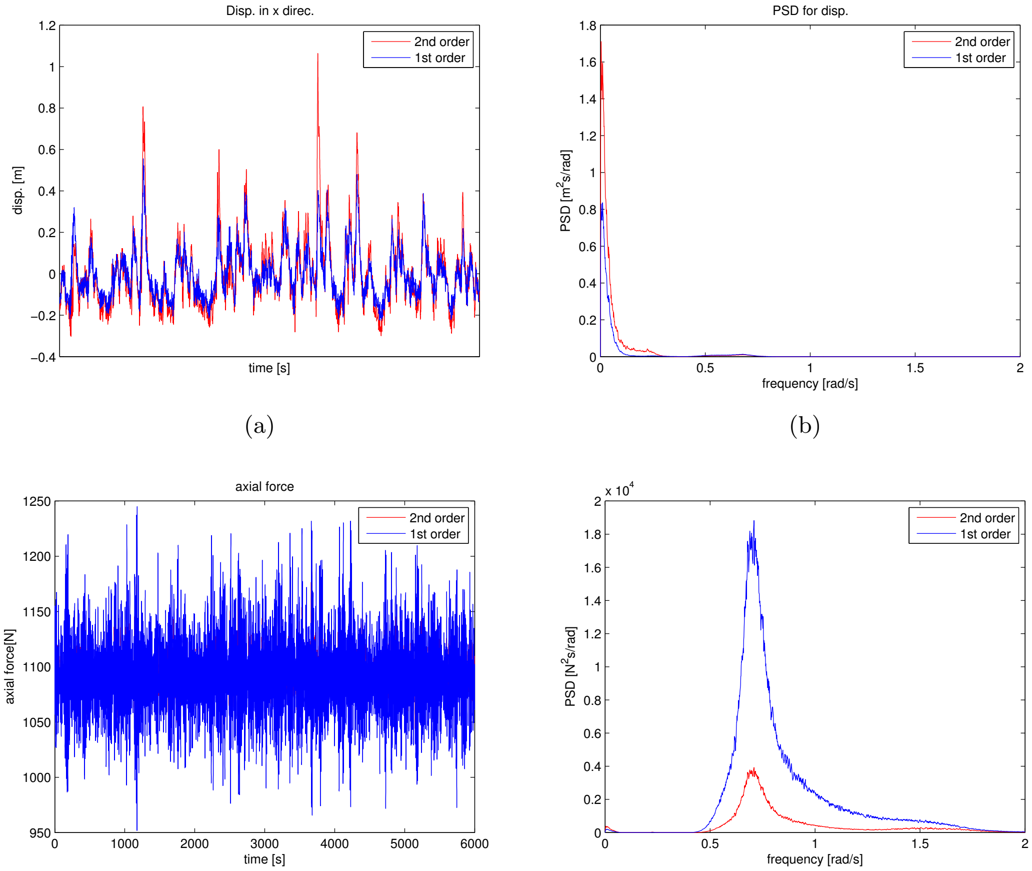

(a) (b)

(c) (d)

Figure D.6: *Maixmum value of dynamic response on main mooring line 9,* $H_s = 6\ m, T_p = 12\ s$

Appendix E

Wave Force

Table E.1: *Comparison of load statistics of monopile base shear, quasi-static assumed, averages over 50 simulations, absolute value*

	Model	1	2	3	4	5	6
1	Max	9.83E+05	1.06E+06	9.90E+05	1.02E+06	1.01E+06	1.13E+06
	Sta.Dev	2.86E+05	2.89E+05	2.87E+05	2.87E+05	2.89E+05	2.93E+05
2	Max	1.43E+06	1.61E+06	1.46E+06	1.50E+06	1.52E+06	1.82E+06
	Sta.Dev	4.22E+05	4.28E+05	4.23E+05	4.21E+05	4.28E+05	4.37E+05
3	Max	1.55E+06	1.78E+06	1.59E+06	1.63E+06	1.65E+06	2.05E+06
	Sta.Dev	4.64E+05	4.72E+05	4.65E+05	4.63E+05	4.72E+05	4.85E+05
4	Max	1.62E+06	1.84E+06	1.71E+06	1.68E+06	1.82E+06	2.17E+06
	Sta.Dev	4.82E+05	4.91E+05	4.84E+05	4.81E+05	4.95E+05	5.07E+05

Table E.2: *Comparison of load statistics of monopile base bending moment, quasi-static assumed, average over 50 simulations, absolute value*

	Model	1	2	3	4	5	6
1	Max	1.24E+07	1.38E+07	1.25E+07	1.27E+07	1.27E+07	1.51E+07
	Sta.Dev	3.57E+06	3.61E+06	3.57E+06	3.55E+06	3.62E+06	3.67E+06
2	Max	1.74E+07	2.03E+07	1.77E+07	1.78E+07	1.87E+07	2.38E+07
	Sta.Dev	5.06E+06	5.14E+06	5.07E+06	4.98E+06	5.18E+06	5.27E+06
3	Max	1.88E+07	2.22E+07	1.94E+07	1.93E+07	2.07E+07	2.65E+07
	Sta.Dev	5.57E+06	5.69E+06	5.59E+06	5.47E+06	5.74E+06	5.85E+06
4	Max	1.91E+07	2.25E+07	2.01E+07	1.94E+07	2.23E+07	2.77E+07
	Sta.Dev	5.63E+06	5.71E+06	5.64E+06	5.49E+06	5.85E+06	5.88E+06